NEUTRONIC AND CFD-THERMAL HYDRAULIC ANALYSES OF VERY-SMALL, LONG-LIFE, MODULAR (VSLLIM) REACTOR

Luis M. Palomino and Mohamed S. El-Genk

Institute for Space and Nuclear Power Studies

Technical Report_TR_UNM_ISNPS-1-2019

The University of New Mexico, Albuquerque, New Mexico, USA

May 2019

ACKNOWLEDGEMENTS

The University of New Mexico's Institute for Space and Nuclear Power Studies (UNM-ISNPS) funded this research. The authors are grateful to the University of New Mexico's Center for Advance Research Computing (CARC) for having access to the supercomputers clusters, which was critical to completing the CFD calculations involved in this research.

EXECUTIVE SUMMARY

Neutronic and CFD-thermal hydraulic analyses are performed of the **V**ery-**S**mall, **L**ong-**LI**fe, and **M**odular (VSLLIM) nuclear reactor. This reactor was developed at the University of New Mexico's Institute for Space and Nuclear Power Studies (UNM-ISNPS) to generate 1.0 – 10 MW_{th} for extended periods without refueling. It offers passive operation and safety features and redundant control and would be fabricated, assembled and sealed in the factory. During nominal operation and after shutdown, the VSLLIM is cooled by natural circulation of in-vessel liquid sodium, with the aid of an in-vessel chimney and annular helically-coiled tubes Na-Na heat exchanger (HEX) in the downcomer. In case of a malfunction of the Na-Na HEX, the reactor shuts down, and the decay heat generated in the core is removed by natural circulation of the in-vessel liquid sodium with the aid of redundant passive means. These include variable-conductance liquid-metal heat pipes that are embedded in the upper part of the reactor primary vessel wall, and natural circulation of ambient air along the outer surface of the reactor guard vessel wall.

The VSLLIM reactor core is loaded with hexagonal assemblies of 19 UN fuel rods clad in HT-9 steel and with scalloped BeO walls, clad also in HT-9 steel. In addition to helping achieve an almost uniform flow distribution in the fuel assemblies, the scalloped BeO walls, together with the BeO axial and radial reflectors, increase the hot-clean reactivity for achieving long full-power operation life, at a relatively low UN fuel enrichment. During nominal operation, the inlet and exit coolant temperatures in the reactor core are maintained at 610 K, and $\leq$ 820 K to minimize embrittlement and corrosion of the HT-9 steel cladding, core structure, and reactor vessel by liquid sodium.

This research conducted neutronic and thermal-hydraulics analyses to investigate and quantify the passive operation and safety features of the **V**ery-**S**mall, **L**ong-**LI**fe, and **M**odular (VSLLIM). The research tasks carried out include:

(a) Performing neutronic analyses of the VSLLIM to investigate the effects of several design and material choices on the cold and hot-clean reactivity, for achieving long operation life without refueling. Also calculate the cold-clean reactivity shutdown margins of the emergency shutdown system (ESS) and reactor control (RC), and the beginning of life (BOL) hot-clean reactivity. Investigated are the effect of UN fuel

enrichment, and the material of the axial and radial reflectors. These analyses calculated the neutron energy spectrums and the radial and axial fission power distributions. These are in addition to determining the temperature reactivity feedback effects due to the UN fuel, sodium coolant, HT-9 steel cladding and core structure, BeO in the driver core and axial radial reflectors, and the Doppler broadening of neutron cross-sections. To estimate the full-power operation lives of the VSLLIM reactor at different thermal powers, fuel depletion calculations are carried out at hot-clean operation condition.

(b) Performing thermal-hydraulic and computational fluid dynamics (CFD) analyses during nominal reactor operation and after shutdown. These analyses estimated the friction number for the liquid sodium flow in the core hexagonal UN fuel assemblies, with scalloped wall as a function of the flow Reynolds number. The flow and temperature distributions in the UN fuel assemblies are calculated, at different reactor thermal powers and inlet and exit core temperatures of 610 K and < 820 K, respectively.

(c) Performing CFD analyses to quantify the passive decay heat removal by natural circulation of ambient air along the outer surface of the reactor guard vessel, after reactor shutdown and in the case of a malfunction of the in-vessel Na-Na HEX.

The performed neutronics and fissile depletion analyses of the VSLLIM confirmed that a UN fuel enrichment of 13.76% is sufficient for achieving high enough hot-clean excess reactivity for operating VSLLIM reactor without refueling for ~92 and 5.8 full power years (FPY) at 1.0 and 10 $MW_{th,}$ respectively. Results confirmed sufficient cold-clean reactivity shutdown margins using either the reactor control (RC) or the emergency shutdown system (ESS), independently. In addition to having two independent reactor shutdown systems, results show that the negative temperature reactivity feedback is capable of shutting down the reactor with a modest increase in the temperatures of the UN fuel and the in-vessel liquid sodium. Results also show that the neutron energy spectrum in the VSLLIM reactor core is hard, which reduces the inventory of minor actinides in UN fuel during reactor operation. Because of its low operating temperatures, $\leq$ 812 K at 10 MW_{th} and UN fuel low average power density ($\leq$ 23.47 MW_{th}/m^3), the fuel

in the VSLLIM core experiences practically no swelling and retains practically all fission gas release.

The performed CFD-thermal-hydraulics analyses investigated the effects of using metal fins along the outer surface of the guard vessel wall and changing the width of the cold air intake duct on the decay heat removal rate and the time after shutdown for cooling the in-vessel liquid sodium to 400 K. Results show that without metal fins, the heat removal rate of the decay heat is 244 kW_{th} immediately after shutdown. However, within 8 minutes after shutdown, natural circulation of ambient air along the outer surface of the guard vessel removes more heat than is being generated by radioactive decay in the core. Consequently, the average in-vessel sodium temperature drops from 682 K to 400 K, within 120 hrs after shutdown.

Using metal fins along the outer surface of the guard vessel increases the total area for heat transfer and the decay heat removal rate by 13.5%, reducing the time for the average temperature of the in-vessel liquid sodium to decrease to 400K in ~100 hrs. Without metal fins, reducing the width of the cold air intake duct by 50% decreases the decay heat removal rate by 35%, increasing to ~ 346 hrs the cooling time of the in-vessel sodium to 400 K. These results demonstrate that the decay heat removal by natural circulation of ambient air from the outer surface of the reactor guard vessel wall, with and without metal fins, is quite effective. Additionally, the results show that the temperature of the in-vessel sodium after shutdown remain safely, ~470 K below its boiling point (~1156 K at 0.1 MPa).

The performed CFD analyses investigated the friction factor for laminar, transition, and turbulent flows in hexagonal bundles of bare tube and also investigated with flat and scalloped walls. The results for the bundles with flat walls are in good agreement with previously reported experimental data by others. The CFD results and the reported experimental data for bundles with flat walls and various numbers of tubes, (7, 19, 37, and 61), in a triangular lattice with $1.07 \leq P/D \leq 2.416$, are used to develop a continuous correlation of the friction factor as a function of P/D and Re_{in}. The developed correlation, for P/D up to 3.0, and a wide range of tubes in the bundles (N = 7 – 331), spans all three flow regions ($10^2 < Re_{in} < 10^6$) and is in excellent agreement with the compiled numerical

and experimental database. The results also validated the applicability of the developed friction factor correlation to the VSLLIM reactor hexagonal bundles with scalloped walls.

The developed continuous friction factor correlation is within 5% - 8% of the CFD data generated for the scalloped walls bundles with 19 and 37 rods or tubes. Results also showed that scalloped walls reduce the bypass flow next to the wall, while increasing the flow in the interior subchannels in the bundles, thus improving heat transfer. Higher flow in interior subchannels enhances the thermal-hydraulics in the VSLLIM reactor core and reduces the maximum temperature at a given Re_{in}.

TABLE OF CONTENTS

LIST OF FIGURES

LIST OF TABLES

NOMECLATURE

A	Cross section flow area (m^2), friction factor parameter for laminar flow, Eq. (6.2), (6.5a)
B	Friction factor parameter for turbulent flow, Eq. (6.5b)
B_4C	Boron Carbide
BeO	Beryllium Oxide
BOL	Beginning of Life
CC	Cold clean at BOL
CFD	Computational fluid dynamics
CO_2	Carbon dioxide
D	Diameter (m)
DC	Direct current
D_e	Equivalent hydraulic diameter, 4 *A*/*Wp*, Eq. (6.1a)
$D_{e,sub}$	Subchannel equivalent hydraulic diameter, Eq. (6.1b)
DUN	Depleted Uranium Nitride
EOL	End of Life
ESS	Emergency Safety Shutdown
f	Friction factor, Eq. (6.9)
FP	Fission Products
FPY	Full Power Year
G	Fluid mass flux, $\dot{m}/A$ ($kg/m^2.s$)
H	Height (m)
HC	Hot-Clean at BOL
HEX	Concentric helically coiled tubes, Na-Na heat exchanger
HP	Heat Pipes
HT-9	High Chrome and strength, Ferritic-Martensitic steel
HTR	High Temperature gas cooled Reactor
k_{eff}	Effective multiplication factor
kgHM	kilograms of heavy metal in fresh fuel
L	Length (m)
LMHPs	Liquid Metal Heat Pipes

MA	Minor Actinides
MTHM	Metric Tons of Heavy Metal in fresh fuel
N	Number of tubes or rods in hexagonal bundle
Na	Sodium
NCRP	National Council on Radiation Protection
P	Thermal power (MW_{th}, kW_{th}), Pitch of tubes or rods in hexagonal bundles (Fig. 6.1a)
P/D	Pitch to diameter ratio
Pb	Lead
Pu	Plutonium
PWR	Pressurized Water Reactor
r	Radial coordinate
R	Radius (m)
Re	Reynolds Number, GD_e/μ, $(-)$
SFR	Sodium fast Reactor
SLIMM	**S**calable **LI**quid **M**etal cooled **M**odular reactor
SMR	Small Modular Reactor
T	Temperature (K)
TE	Thermoelectric
U	Uranium
UN	Uranium Nitride
VSLLIM	**V**ery-**S**mall, **L**ong-**LI**fe, **M**odular reactor
vSMR	very Small Modular Reactor
W	Separation distance of nearest rod / tube to the bundle flat wall (Fig. 6.1a)
Wp	Wetted perimeter (m)
Y	Hexagonal bundle flat-to-flat distance (m)
z	Axial coordinate
Subscripts	
b	Bundle
BeO	Beryllium oxide
C	Reactor core

Ch	In-vessel chimney
Doppler	Doppler broadening of neutron cross-section
e	Equivalent
ex	Reactor core exit
Fuel	UN fuel in reactor core
HEX	In-vessel Na-Na Heat Exchanger
in	Reactor core inlet
n	Exponent, Eq. (6.5b)
ref	Reference
Riser	Distance from HEX exit to top of Rx core
Rx	Reactor
sub	Subchannel (Eq. 6.1d)
t	turbulent
V	Vessel
l	Laminar

Greeks

β	Parameter, Eq. (6.1b)
γ	Parameter, Eq. (6.1c)
μ	Dynamic viscosity (Pa.s)
ρ	Reactivity ($), Density (kg/m^3)
τ	Operation life time in FPY, Eq. (4.1)

1. INTRODUCTION

There is recent global interest in developing and deploying small modular nuclear reactors (SMRs). SMRs are those that provide electric power between 15 - 300 MW_e (IAEA, 2012; El-Genk and Palomino 2014, 2015; El-Genk et al., 2017), whereas reactors that produce less than 15 MW_e are considered very small modular reactors (vSMRs) (Moore, 2016; World Nuclear Association, 2016). SMRs and vSMRs can be used to generate electricity and/or supply process heat for industrial applications (e.g., seawater desalination, hydrogen production by thermochemical and electrolysis, biofuels processing, oil refinery, district heating).

There is a wide range of SMR designs in development around the world to potentially address some of the challenges that large nuclear power plants face, such as lengthy construction time and delays, passive operational safety, and proliferation concerns. A large light water reactor that produces 700 - 1,500 MW_e can cost \$5B - \$10B and world require approximately 5 - 6 years for construction before it comes on line (IAEA, 2012; Hidayatullah et al., 2015; Singh, 2013). In contrast, a 300 MW_e SMR unit may cost less than \$2B and require only ~24 months for construction (Ingresoll, 2009). A 10 MW_e vSMRs plant would likely require even less time, and cost only ~\$80M (Carelli, 2010; El-Genk and Palomino, 2014, 2015; El-Genk et al., 2017).

SMRs and vSMRs are designed with fast, epi-thermal, or thermal neutron energy spectra, and are cooled with pressurized water, pressurized helium gas, near atmospheric liquid sodium, molten fluoride salt, molten lead or molten lead-bismuth alloy (IAEA, 2007, 2012, 2014; Ingersoll, 2009; Brown et al., 2017; Lommers et al., 2014; Wang et al., 2015). The integral design of these compact reactors makes them safer by having the heat exchanger or steam generator inside the reactor vessel, and reducing the number of vessel penetrations. Placing the heat exchanger or steam generator above the reactor core creates a relatively tall reactor vessel, which facilitates natural circulation for cooling the reactor core during nominal operation, and after shutdown (Locatelli, 2014). SMRs and vSMRs also take advantage of a high volume-to-surface area ratio to incorporate passive decay heat removal via natural circulation of ambient air (Ingersoll, 2009; Liu, 2014; El-Genk and Palomino, 2014, 2015; El-Genk et al., 2017).

The small physical sizes of SMRs and vSMRs makes it possible to be fabricated, assembled, and sealed at the factory, and transported by barge, rail, or truck to the site (Ingersoll, 2009, El-Genk and Palomino, 2014, 2015, El-Genk et al., 2017). This ease of manufacturing and transportation opens up many opportunities for nuclear power energy, including use in niche markets. For Example, SMRs and vSMRs could be made available to remote communities, islands, and outposts, as a stable source of energy (IAEA, 2007; The U.S Department of Energy's Office of Nuclear Energy, 2011; John, 2018)). In addition, the physical footprint of these power plants is considerably smaller than of a large plant, increasing the options for site placement and facilitating emergency planning. SMRs and vSMRs offer many advantages regarding plant safety, including a smaller inventory of actinides, eliminating accidents through improved design, and passive response to unexpected transients (Kemeny, 1979; IAEA, 2008, 2012; Vujic 2012). Owing to their small sizes, these reactors can be housed in small buildings, or installed below ground to be protected from impact by airplanes or missiles. Furthermore, they can be mounted on seismic isolating bearings to withstand earthquakes.

Many conceptual designs are currently being developed around the world to satisfy a wide range of needs and applications. There are approximately 60 SMR designs being developed or under licensing in many countries including the Russian Federation, Japan, Argentina, China, India, Republic of Korea, and the US, several of which are at the prototype stage (IAEA, 2007, 2012, 2014, 2018; Smith and Wright, 2012; Salemo et al., 1988; Kuznetsov, 2008; Kyoko et al., 2011; Ingersoll et al., 2014; Horie et al., 2008; Chun et al., 2013; B&W Nuclear Energy Inc., 2011; Carelli et al., 2010; GA, 2010; El-Genk and Palomino 2014, 2015; El-Genk et al., 2017). Although there are many SMR designs being developed around the world, there are relatively few vSMRs under development (IAEA, 2008, 2012, 2014; Ingresoll 2009, Vujic 2012; Liu 2014). The small and portable vSMRs could provide electricity or process heat for many industrial applications, for remote mining or drilling operations, for remote outpost, military bases and for remote communities with low energy needs ranging from 1.0 – 10 MW_{th}.

The objectives of this research are to perform detailed neutronics and CFD-thermal hydraulic analyses of the **V**ery-**S**mall, **L**ong-**LI**fe, and **M**odular (VSLLIM) nuclear reactor, developed at the University of New Mexico's Institute for Space and Nuclear

Power Studies (UNM-ISNPS) for generating 1.0 – 10 MW_{th}. The VSLLIM reactor could provide energy to remote communities, islands nations for extended periods of time. Furthermore, it has low upfront financial risk and short construction time, and could be installed at a permanent site or on a portable platform. The VSLLIM reactor has a fast neutron energy spectrum and with the same core design can generate 1.0 – 10 MW_{th} for long operation of time without refueling. This reactor uses 'off-the-shelf' materials for fuel, cladding, core structure, and the primary and guard vessel.

Reactor shutdown is accomplished by redundant means and / or by the negative reactivity feedback, with a sufficient temperature margin from the boiling point of the in-vessel liquid sodium. VSLLIM operates passively except for the reactor control (RC) and the emergency shutdown system (ESS). During nominal operation, and after shutdown, the reactor core is cooled by natural circulation of in-vessel liquid sodium. Natural circulation is achieved with the aid of a tall chimney and annular, helically coiled tubes Na-Na heat exchanger (HEX) located at the top of the reactor vessel to enhance in-vessel natural circulation. In case of malfunction of the Na-Na HEX, this reactor design comes with a backup passive decay heat removal system and liquid metal (LM) heat pipes along the reactor primary vessel wall. Those include natural circulation of ambient air at the outer surface of the reactor guard vessel. The VSLLIM may be factory-fabricated in modules, assembled and sealed at the factory. It can be deployed on a portable/mobile platform together with the rest of the power system or transported to a site by rail, barge or heavy truck and be permanently installed below ground to avoid direct impact by aircraft or missiles and mounted on seismic isolating bearings to resist earthquakes.

Neutronics and fuel depletion analyses are needed to demonstrate that the VSLLIM is capable of operating for a prolonged period without refueling, and with relatively low fuel enrichment. Also, neutronic analyses are needed to assess potential power and temperature peaking in the core, while meeting a shutdown requirement of -$1 cold-clean. The VSLLIM core is loaded with hexagonal bundle of 19 UN fuel rods with scalloped BeO walls. Thermal-hydraulic analyses of the core assemblies are needed to determine the pressure losses and examine the flow and temperature distribution within the assemblies. However, a friction number correlation for sodium flow in hexagonal assemblies with scalloped walls does not exist and therefore needs to develop.

Additionally, further analyses are needed to ensure that the decay heat is passively removed by the natural circulation of ambient air along the outer surface of the compact reactor guard vessel, in case of an unlikely malfunction of the in-vessel Na-Na heat exchanger (HEX).

Therefore, the objective of this research is to investigate the neutronic, thermal-hydraulics and passive operation and safety features of the VSLLIM. This includes the following tasks:

(a) Perform neutronic analyses to investigate the effects of several design and material choices on the cold and hot-clean reactivity, for achieving long operation life without refueling. Also calculate the cold-clean reactivity shutdown margins of the emergency shutdown system (ESS) and reactor control (RC), and the beginning of life (BOL) hot-clean reactivity, and investigate the effects of the UN fuel enrichment, and the BeO axial and radial reflectors. These need to analyses calculate the neutron energy spectrums and the radial and axial fission power distributions. These are in addition to determining the temperature reactivity feedback effects due to the UN fuel, sodium coolant, HT-9 steel cladding and core structure, BeO in the driver core and in the axial radial reflectors, and the Doppler broadening of the neutron cross-sections. To estimate the full-power operation lives of the VSLLIM reactor at different thermal powers, fuel depletion calculations need to be carried out at hot-clean operation condition.

(b) Perform thermal-hydraulic and computational fluid dynamics (CFD) analyses during nominal reactor operation and after shutdown. These analyses estimate the friction number for the liquid sodium flow in the UN fuel assemblies with scalloped wall as a function of the Reynolds number. They also calculate the flow and temperature distributions in the UN fuel assemblies, at different reactor thermal powers.

(c) Perform CFD analyses of the passive decay heat removal by natural circulation of ambient air along the outer surface of the reactor guard vessel after reactor shutdown and in the case of a malfunction of the in-vessel Na-Na HEX.

Chapter 2 provides a background on SMRs and vSMRs development and design worldwide. Chapter 3 describes the VSLLIM design core design, the reactor control and emergency shutdown, natural circulation of in-vessel liquid sodium, and passive decay

heat removal and auxiliary power generation. Chapter 4 presents the neutronics and fissile depletion analyses, results of the temperature reactivity feedback effects and the reactor operation lifetime estimates. Chapter 5 presents the CFD-thermal hydraulic analyses and results for passively removing the decay heat generated in the reactor core after shutdown and in case of a malfunction of the in-vessel Na-Na HEX, by natural circulation of ambient air along the outer surface of the guard vessel wall. Chapter 6 presents the CFD analyses and results for developing of a friction factor correlation in hexagonal rod bundles with flat and scalloped walls.

2. BACKGROUND

Small modular reactors (SMRs) and very small modular reactors (vSMRs) have been under development for many years, however due to economy of scale, these types of reactors were put aside until recent years. SMRs are those that provide electric power between 15 - 300 MW_e (IAEA, 2018; El-Genk and Palomino, 2014, 2015, El-Genk et al., 2017), whereas reactors that produce less than 15 MW_e are considered vSMRs (Moore, 2016; World Nuclear Association, 2016; Filippone, 2017; DoD, 2016; Westinghouse, 2017; Sterbentz et al., 2017). This section will discuss the history of all nuclear reactors and the current and potential use of SMRs and vSMRs.

After World War II, the U.S. Navy started developing small nuclear reactors with the intention of using them as power sources for submarines and aircraft carriers. By the 1950s, the Navy had developed and deployed a Small Light-Water Reactors (SLWR) that was capable of providing power to submarines (Vujic 2012, Ingersoll 2009, U.S. Department of Energy May 2011). Currently, the U.S. Navy nuclear program has successfully operated more than 100 nuclear reactors that provided from 10s-100s of MW_e each, for submarines and aircraft carriers (Ingersoll 2009).

Following the Navy's lead, the U.S. Air Force started the Aircraft Nuclear program. From 1946 to 1961, the Air Force developed a small high-temperature nuclear reactor to provide power to long-range bombers (Suid, 1990). Developing an aircraft that was powered by a nuclear reactor proved too complex, and by 1961 this program became politically undesirable and was terminated. Similarly between 1954 and 1976 the Air Force and the Navy, the Army started their own Nuclear Program, building eight small nuclear reactors capable of providing for 1.0 to 10 MW_e. However, funding for the program was discontinued because of the high cost of nuclear power plants compared to cheaper alternatives, such as fossil fuel power plants (U.S. Department of Energy, 2011).

During this time, the U.S. economy and population was rapidly growing. As a result, the demand for electric power grew rapidly and ushered in the commercialization of nuclear power plants. The increased demand for energy and the confidence in the safety of nuclear power plants motivated the development of large commercial reactors. The first commercial nuclear power plants were scaled-up versions of the Navy's LWR power

plants, and produced 60 to 1300 MWe. The economic drivers behind these commercial reactors were the low price of electricity (IAEA 2018).

Large LWRs brought up concerns about the safety and thus, new safety regulations were imposed. The addition of new regulations increased safety measures for the primary and auxiliary systems, increasing the complexity of the LWRs, compared to the scaled-up Navy version (Ingersoll, 2009). The nuclear industry faced many setbacks and complications due to the increased safety regulations and complexity of the large nuclear reactors. These were realized through increased cost, licensing, construction, and operation delays, and consequently reduced the confidence of investing in nuclear power plants. Finally, after the Three Mile Island accident in 1979 interest and new investments in the nuclear industry were suspended (Kemeny, 1979; Ingersoll, 2009). As a result, there was no new construction of LWRs in the 1980s, and plant owners were motivated to maximize the power output and the load factor of their original plants, extending the power plant lifetime from 30 to 40 years. In 1982 the Electric Power Research Institute (EPRI) surveyed 11 nuclear power plants operating LWRs, concluding that nuclear power plants of 1200-1300 MW_e were too large (Martel et al., 1985). The survey found that large nuclear plants need to be less sensitive to events in the secondary system.

The EPRI survey not only showed the design challenges of LWRs, but also encouraged the development of Advance Light Water Reactors (ALWRs). At the beginning of this new program, the nuclear reactor design, development, and requirements were done jointly by the utility companies and the reactor vendors. As the program progressed, the government helped to fund the development and certification of a new generation of LWRs, which were designated as Generation III. The Nuclear Regulatory Commission (NRC) eventually certified three nuclear reactor designs: the Advance Passive AP-600 (subsequently upsized to over 1000MW_e) by Westinghouse; the System 80+ by ABB-Combustion Engineering; and the Advanced Boiling Water Reactor by General Electric (U.S. Department of Energy 2011). These new nuclear power plants focused on the use of passive safety features and the reduction of materials, like concrete and steel. They also reduced the probability of system failure by reducing the amounts of required components like valves, pumps, wires, etc.

During the 1960s and 1970s the nuclear industry grew so quickly that it was thought the uranium supply would be exhausted. To address this concern, a parallel program to the LWRs program was started in order to develop another type of reactor (Ingersol, 2009). This new program was the fast spectrum reactor. The main objective of the fast spectrum reactor program was to design a nuclear reactor that could produce or breed more fuel than it consumed. Through this new program, the liquid-metal-cooled fast breeder reactor (LMFBR) was developed. By 1980s the LMFBR program managed to build a 400 MW_{th} test facility. Later, development of the 375 MW_e Clinch River Breeder Reactor (CRBR) was terminated in 1984 when it was 80% completed because it faced strong opposition from the public due to an anti-nuclear sentiment following the Three Mile Island accident. This forced the U.S. Congress to pass a bill which canceled funding for the project. Before cancellation of the CRBR, it was thought that large LMFBR (over 1000MW_e) would replace the existing LWRs operating at the time (Ingersoll, 2009).

After the LMFBR program was canceled, the nuclear industry was challenged to build Fast Reactors. Following the Three Mile Island accident, safety concerns had increased and it was thought that LWRs were too complex to build and operate safely. To address this problem, the government (with the help of the nuclear industry and national laboratories) initiated the Advance Liquid-Metal Reactor (ALMR) program. The objective of this program was to develop a new Fast Breeder Reactor design that reduced the need for active safety systems and would use a more "passive" or "inherent" safety system. The ALMR program in the General Electric Power Reactor Inherently Safe Modular (PRISM) (IAEA, 2014) has the unique feature of grouping nine units of 160 MW_e power to form a power plant of 1440 MW_e, which is equivalent to a large LWR power plant (IAEA, 2011).

In spite of all the problems and challenges that large nuclear power plants have, the nuclear power industry made tremendous progress in seven decades. The nuclear industry is now on its way to a new period of technology development with the understanding of LWR design, the push for more power due to an increasing population, the reduction of carbon-emissions to curb climate change, and the desire to increase national security through energy independence. These factors are opening doors for the nuclear industry to commission and construct new nuclear power plants. In this new nuclear era, SMRs and

vSMRs have the benefit of: factory fabrication; a simple and compact design; transportable by rail, barge or truck; and low capital investment. SMRs and vSMRs will complement the larger power plants that will be built for the base load demand by being scaled up or down to meet power needs. The nuclear industry has moved on from its stormy past and will continue to improve on the safety, efficiency, and security of its technology as it powers the next generation.

2.1. SMRs and vSMRs

There has been increased interest in the development of SMRs and vSMRs due to an increase in energy demand and the threat of climate change. Nuclear power provides large amounts of electricity with virtually zero greenhouse gas emissions during operation, providing a solution to these two problems (Odmaa, 2012). To provide flexible power generation and a non-polluting energy source that is transportable and safe, SMRs and vSMRs are being developed around the world. Countries such as the Russian Federation, Japan, Argentina, China, India, Republic of Korea, and the U.S. are leading the way in developing different SMR and vSMRs designs and are building prototypes. In the near future, construction and deployment will be possible. The proposed SMR and vSMRs designs by these countries have multiple purposes such as electricity production and process heat utilization for industrial processes, hydrogen production, water desalination, and district heating (Fig. 2.1). SMRs and vSMRs accommodate many needs for potential clients due to their multiple advantages. These advantages include: providing power generation in remote locations with limited infrastructure for continuous transportation of fuel year-round; modular concept and factory fabrication making construction faster; long operation time of about 1.5-30 years (IAEA 2018) which reduces the need for refueling; design simplicity that reduces the risk of accidents or failures; passive safety systems that allow for quick response in case of an accident without the need of an operator; a smaller footprint which allows for more potential sites; lower operation and maintenance costs; lower financial risk; and proliferation resistance.

The smaller size of a SMR allows for factory fabrication. All components can be fabricated in local forging factories using conventional fabrications capabilities in contrast with large rectors that require large metal forging factories, which are only available in one or two countries. Additionally, transporting large components like the

reactor vessel would restrict the location of new plants to coastal areas or along rivers (Maitra, 2018). SMRs and vSMR use smaller reactor vessels that can be transported by barge, rail, or truck (Locatelli, 2014). This opens many new markets for nuclear power that were untapped by the previous large LWR technology. Many remote communities, islands, and landlocked cities could have a reliable source of energy. Construction in such locations would be considerably faster as the reactor would be transported to the site, reducing the cost of construction, schedule uncertainty, and also increasing the safety and reliability of the plant. Due to the smaller footprint of SMRs, the amount of space necessary to provide power to these untapped communities would also be much less than previous LWR technology.

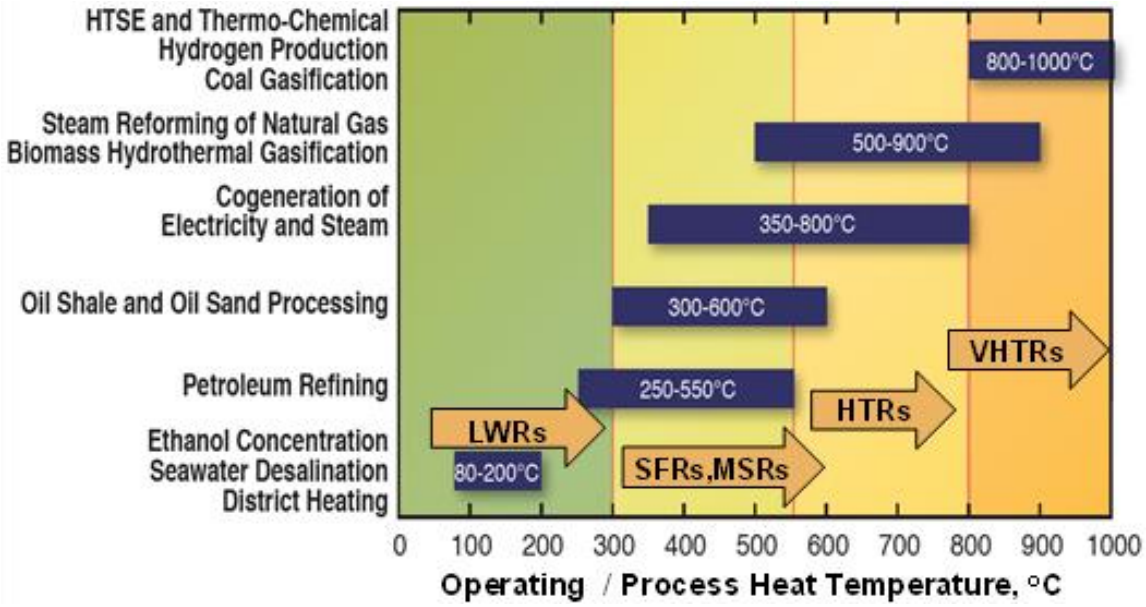

Fig. 2.1. Potential applications of process heat from SMRs of different types (Schriener and El-Genk, 2018; IAEA, 2016).

Plant safety is of the utmost importance for nuclear power because of the three major nuclear accidents at Chernobyl, Three Mile Island, and Fukushima. SMRs offer many advantages regarding plant safety, such as smaller inventory of actinides, elimination of accidents by design, and passively responding to unexpected reactor transients.

The primary concern of nuclear power plants is the retention of radioactive nuclides inside the reactor pressure vessel. The number of radionuclides in the reactor core is directly proportional to the power level of the reactor. Thus, for the AP-1000 which

produces 1000$MW_{e,}$ it will produce about four times more radionuclides than a SMR or vSMRs that produces <300 MW_e. The benefits of operating at lower power levels also include decreased shielding and smaller plant footprint and emergency planning zone, allowing the installation of the power plant to be closer to communities and reduces the infrastructure required to provide power in isolated communities.

SMRs and vSMRs eliminate accidents by design due to an integral system reactor. This means that the reactor core, steam generator or heat exchanger, and pressurizer are all inside the primary reactor vessel (Ingersoll et al., 2014, Locatelli et al., 2014, IAEA, 2018). The integral design eliminates all large coolant pipes that penetrate the reactor vessel and having the heat exchanger or steam generator inside of the reactor vessel allows the use of a small feed that penetrates the vessel carrying steam or coolant to a secondary heat exchanger (El-Genk et al., 2017). With the heat exchanger inside the reactor vessel, the total inventory of coolant in the primary system is much larger and this extra coolant inventory increases the heat capacity and thermal inertia of the system and prevents core heat-up transient. Traditionally in SMRs and vSMRs designs the heat exchanger is placed above the reactor core creating a relatively tall system that facilitates the use of natural circulation to cool the reactor core during nominal operation and after shutdown (El-Genk et al., 2017).

After shutdown, the decay heat is removed passively from the reactor core by conduction of the heat through the reactor core structural material and by natural circulation of the primary coolant (Palomino and El-Genk, 2016). The passive decay heat removal system by natural circulation of ambient air in SMRs and vSMRs design can accommodate the decay heat better than large power reactors for several reasons. The low operation power means decreased decay heat generated, a small core volume allows the heat to move more rapidly to the reactor vessel, and the high surface to volume ratio of SMRs and vSMRs increase the effectiveness of external heat removal compared to large reactors (Ingersoll, 2009).

As mentioned above, the low power and small physical size of SMRs and vSMRs allows for the installation of plants to be closer to populated areas. The small size of the SMRs and vSMRs would also require a small building. This smaller building would improve plant safety by using seismic isolators similar to what is used for conventional

buildings in high seismic activity areas like Japan, and the seismic isolators will prevent seismic-induced damage. The low power output of a SMRs and vSMRs can better match the requirements and needs for some consumers. For instance, a 100 MW_{th} reactor could provide electricity to a small community and provide process heat for the production of liquid fuels from biomass or seawater desalination (Greene, 2008) (Fig. 2.1). For such a community, SMRs and vSMRs provide grid stability and allow the community to build new capacity at the rate that more closely matches the growth demand without spending a lot of money up front.

SMRs and vSMRs are much cheaper than large nuclear power plants. For example, a large LWR that produces 700-1,500 MW_e could cost between five and 10 billion dollars and construction can last five to six years. On the other hand, a 300 MW_e SMR could cost less than two billion dollars and construction would take approximately two years. A 10 MW_e SMR plant could take even less time for a price of 80 million dollars (Carelli 2010). However, these are only estimates for SMRs and vSMRs and more research needs to be done to prove the feasibility of SMRs and vSMRs compared to those of large LWRs, when economies of scale are applied to SMRs and vSMRs.

Currently, there are many conceptual designs being developed around the world that meet a wide range of needs and applications. SMRs and vSMRs come in several types and depending on the energy spectrum of the core, the reactor could have a thermal, epi-thermal, or fast neutron spectrum. Typically these reactors are cooled with pressurized water, pressurized helium gas, near atmospheric liquid sodium, molten salts, molten lead, molten lead-bismuth alloy or by the use of heat pipes. Depending on the type of energy spectrum and reactor coolant, SMRs and vSMRs are placed into five groups: Thermal or Light Water Reactors (LWRs), Hight Temperature Gas-Cooled Reactors (HTGRs), liquid metal cooled reactors, molten salt reactors, and heat pipe cooled reactors (IAEA, 2007, 2012; Smith and Wright, 2012; Salemo et al., 1988; Kuznetsov, 2008; Kyoko et al., 2011; Ingersoll et al., 2014; Horie et al., 2008; Chun et al., 2013; B&W Nuclear Energy Inc., 2011; IAEA, 2007; Carelli et al., 2010; GA, 2010; Brown et al., 2017).

Light water SMRs and vSMRs have a thermal neutron energy spectrum and are based on proven technology from the large LWRs that have over 60 years of successful operation experience worldwide. There are two versions of LWRs Boiling Water Reactor

(BWRs) and Pressurized Water Reactor (PWRs). These reactors are light water moderated and cooled, have fuel enrichments of less than 10%, and operation lifetimes of 1.5-7 years (IAEA, 2007, 2012; B&W Nuclear Energy Inc.; 2011, Carelli et al., 2010). Reactors with thermal neutron energy spectrums are relatively larger compared to other types of reactors.

High-Temperature Gas Cooled Reactor (HTGR) SMRs and vSMRs have epi-thermal and fast neutrons spectrum, are graphite moderated, and cooled by helium. HTGR-SMRs have attracted worldwide interest because of their high outlet temperature of 1000-1200 K, at a system pressure of 5-7 MPa (GA, 2010). At this high exit temperature, the electricity production efficiency increases and the total plant thermal efficiency is in excess of 45% (El-Genk and Tournier, 2009). High thermal efficiency is attained because of the use of excess heat in many industrial processes like the thermochemical co-production of hydrogen, bio mass fuel production, water desalination, district heating, and other energy intensive industrial uses (IAEA, 2007, 2012, 2014; Rodriguez et al. 2007, 2009; El-Genk et al., 2017, El-Genk and Tournier, 2003). HTGR-SMRs have the potential to reduce the nuclear waste stockpile by reusing and burning nuclear fuel that comes from LWRs (GA, 2010). The technology used for this HTGR-SMRs is based on many years of research, development, and experience from multiple countries like the U.S., Russia Federation, China, and the United Kingdom (IAEA, 2012; Smith and Wright, 2012; Salemo et al., 1988; Kuznetsov, 2008; Kyoko et al., 2011; Ingersoll et al., 2014; Horie et al., 2008; Chun et al., 2013; B&W Nuclear Energy Inc., 2011; IAEA, 2007; Carelli et al., 2010; GA, 2010

Liquid metal cooled reactors use liquid sodium or lead alloy as the primary coolant because metal coolants have much higher heat capacity than water and can remove heat more quickly from the fuel. For these reasons, liquid metal cooled reactors have an increased power density compared to other reactors. Liquid metal cooled reactors are attractive because their size and weight are much less than LWR and HTGR and can lead to decreased transportation costs and concerns. This type of reactor operates at atmospheric pressure because of the low vapor pressure of liquid metals, allowing the use of slimmer reactor vessel walls compared to the ones used for PWRs or HTGRs. The reduced pressure makes liquid metal cooled reactors easier to maintain. Additionally, the

high operation temperature of the liquid metal reactor is used to produce super-heated steam, which increases the thermal efficiency of the plant. Also, because liquid metals conduct electricity, it makes the use of electromagnetic pumps feasible, which can again lead to increased plant efficiency when compared to mechanical pumps.

Of the liquid metal cooled SMRs and vSMRs designs, the most promising is the sodium cooled SMRs (SC-SMRs). This is because SC-SMRs can operate at relatively high core exit temperatures (up to 900 K during nominal operation) and a plant thermal efficiency of 40% (Ueda et al., 2005; Arie, 2009; El-Genk and Palomino, 2014, 2015; El-Genk et al, 2017; El-Genk and Tournier, 2003). Liquid metal cooled SMRs and vSMRs capitalize on more than 30 years of experience from the liquid sodium-potassium-cooled fast reactor Experimental Breeder Reactor I (EBR-I) and the sodium-cooled fast reactor Experimental Breeder Reactor II (EBR II) (INL, 2006). Sodium Fast Reactors (SFR) has many advantages that make them the best option over other reactors due to their fast neutron energy spectrum. This spectrum is more effective than a thermal neutron energy spectrum in reducing the inventory of the minor actinides in the spent fuel due to the high fission-to-capture ratio, making the spent fuel easy to store or reprocess. The fast neutron energy spectrum SC-SMR can achieve long operation life due to the production of fissile Pu by neutron capture in the fertile U^{238}. Additionally, sodium has high thermal conductivity and heat capacity which provides thermal inertia against heat-up transients. Also, sodium has a low vapor pressure making it possible to operate below atmospheric pressure compared to LW- and HT-SMRs that operate at pressures of 5-15 MPa, eliminating the need of thick wall pressure vessels. This is possible because of the low melting point and high boiling point of sodium, 371 K and 1156 K respectively. (Thermal Fluids Central, 2016; Bomellburg et al. 1972; Foust, 1972). This allows for a high exit temperature up to 900 K during nominal operation. At this exit temperature, the stainless-steel corrosion is minimal/negligible and the plant thermal efficiency can be as high as 40%. The excess heat could be used in many industrial applications such as space heating, district heating, and water desalination in coastal nations and arid regions.

Molten lead or lead-bismuth alloys are used as primary coolants in nuclear reactors because of their low neutron absorption cross-sections, neutron reflection, potent gamma shield, and relatively low melting points, and high boiling points. The low neutron

absorption allows for a fast energy spectrum that helps burn minor actinides and produces breeding of more fuel. The coolant also acts as a neutron reflector by returning some of the escaping neutrons back to the reactor core. The high boiling point of lead and lead-bismuth provide safety advantages such as the elimination of the risk of core voiding and allows for higher operation temperature. However, because of the high melting points of lead and lead-bismuth, there is a concern of freezing the coolant while operating at lower power or when refueling or performing maintenance checks. Using lead-bismuth alloy lowers the melting point of the coolant, however the coolant then becomes highly corrosive to the structural materials, but it is still manageable.

Molten Salt Reactors (MSRs) are a class of nuclear reactors that utilize molten salt mixtures as the primary nuclear reactor coolant or as the fuel itself. The nuclear fuel is either solid (e.g. ceramic fuel dispersed in a graphite matrix) or dissolved in the coolant (e.g. uranium tetrafluoride). However, fuel dissolved in the salt is further from commercialization than solid fuel designs. MSRs have a higher thermodynamic efficiency due to high operating temperatures and decreased vapor pressures. The primary coolant salts, mostly lithium-beryllium fluoride and lithium fluoride, remain liquid without pressurization from 773 k to 1673 K (in contrast, at 150 atm a PWR operates at about 588 K). Molten salts are efficient at removing heat from a nuclear reactor, which has the potential to reduce the reactor core size and decrease the required pumping power. The safety profile of MSRs is high due to their passive cooling ability regardless of size. Several designs have incorporated freeze plus, draining the primary salt away from the moderator into dump tanks using gravity if excessive temperatures are reached. MSRs are at a disadvantage in their requirement of an onsite chemical plant to remove fission products and manage the core mixture. Solid fuel MSR technologies are being spearheaded by American researchers and the China Academy of Sciences/SINAP. Molten salt coolant research is underway at the Oak Ridge National Laboratory in the U.S. with the Advanced High Temperature Reactor.

Heat Pipe Cooled Reactors are semi-autonomous vSMRs that use heat pipe technology developed for space nuclear technologies. There are a few vSMRs that implement this technology, such as the eVinci, MegaPower, and Holos nuclear reactor (Westinghouse, 2017, DoD 2016; Filippone, 2017). Heat pipes are used to remove the

heat from a solid reactor core making it a very compact and transportable energy generator that provides power of 200 kW_e-15MW_e (IAEA, 2018). These types of vSMRs are factory fabricated and installed on mobile or floating platforms.

Table 2.1. A partial List of vSMR designs being developed world wide.

vSMR	Type	Plant (MW_e)	Developer, Country	Status	Reference
I. Water Cooled Reactors					
ABV-6M	PWR	6X2	OKBM, Russian Federation	Detailed design	IAEA (2012, 2014, 2016)
UNITHERM	PWR	6.6	RDIPE, Russian Federation	Conceptual design	
Elena	PWR	0.068	RRCKI, Russian Federation	Conceptual design	
SHELF	PWR	6	RDIPE, Russian Federation	Conceptual design	
II. High Temperature Gas-Cooled Reactors					
HTR-10	HTR-He	4.5	Tsinghuan UniV. China, Pebble Bed	Under development	Sun, 2013
U-Battery	HTR-He	4.5	Manchester University, UK	Conceptual design	Ding et al. (2011)
III. Liquid–Metal Cooled Fast Reactors					
CEFR	SFR	19	CNNC, China	In operation	IAEA (2012)
PFBR-500	SFR	20	IGCAR	Under construction	
4S	SFR	10	Toshiba, Japan	Under development	IAEA (2012, 2016)
LFR-TL-X	LMFR	5	HNE, Luxembourg	Preliminary design	IAEA (2018)
SEALER	LMFR	3	LeadCold, Sweden	Conceptual design	IAEA (2018)
SLIMM	SFR	4.5	UNM, USA	Conceptual design	El-Genk et al. (2017)
IV. **Molten Salt Reactors**					
CA Waste Burner	LFR	20	Copenhagen Atomics, Denmark	Conceptual design	IAEA (2018)
V. Heat Pipe Cooled Reactors					
eVinci	HP	0.2	Westinghouse, USA	Conceptual design	Westinghouse (2017)
MegaPower	HP	2	LANL, USA	Under development	DoD (2016)
Holos	HP	3	Holos Generators, USA	Under development	Filippone (2017)

The deployment of vSMRs on mobile or floating platforms offers the flexibility of providing heat and electricity to remote mining and mineral explorations, deep water explorations for fossil fuel, rural small communities, and Native American reservations. However, there are fewer vSMRs designs being developed compared to SMRs. Table 2.1 provides a partial list of vSMRs currently being developed around the world (IAEA, 2012, 2014, 2016, 2018; Westinghouse, 2017; DoD 2016; Filippone 2017; Kyoko et al., 2011; World Nuclear Association, 2016). A vSMR power module, including the energy conversion subsystem, could be fully assembled in the factory and deployed on a truck or on a floating platform.

The research presented in chapter 3-7 includes detailed analyses of The **V**ery-**S**mall, **L**ong-**LI**fe, and **M**odular (VSLLIM) nuclear reactor design concept. Chapter 3 presents the VSLLIM design requirements and describes the VSLLIM design and operation including: reactor core design; reactor control and emergency shutdown; natural circulation of in-vessel liquid sodium; and passive decay heat removal and auxiliary power generation. Chapter 4 details the neutronics and fissile depletion analyses and calculates temperature reactivity feedback effects and reactor operation lifetime estimates. Chapter 5 covers the CFD-thermal hydraulic analyses of passively removing the decay heat generated in the reactor core after shutdown in the case of a malfunction of the in-vessel Na-Na HEX by natural circulation of ambient air along the outer surface of the guard vessel wall. Chapter 6 presents the CFD analyses and development of a friction factor correlation in hexagonal rod bundles with flat walls and scalloped wall. Chapter 7 provides the conclusions of the results from the previous chapter.

3. REACTOR CONCEPTUAL DESIGN

The VSLLIM reactor design is a smaller version of the SLIMM reactor (El-Genk and Palomino 2014, 2015; El-Genk, Palomino and Schriener 2017). This VSLLIM reactor provides 1.0-10 MW_{th} while cooled by natural circulation of in-vessel liquid sodium during nominal operation and after shutdown. The sodium natural circulation is maintained using in-vessel 2-m tall chimney and helically coiled tubes Na-Na heat exchanger, located at the top of the downcomer. This reactor will be fabricated, assembled, and sealed at the factory and deployed on a portable platform together with the rest of the power system. It can also be transported ship by rail, barge, or heavy-duty truck to a permanent site, where it could install below ground and mounted on seismic isolator bearings. The installed VSLLIM incorporates redundant passive decay heat removal systems. These include liquid metal heat pipes along the primary vessel wall and natural circulation of ambient air along the reactor vessel wall. The design requirements for the VSLLIM reactor are as follow:

1. Provide 1.0 - 10 MW_{th} for the same reactor core design.
2. Full-Power operation life >5 FPY without refueling.
3. UN Fuel enrichment <14%.
4. Reactor core is cooled by natural circulation of in-vessel liquid sodium during nominal operation and after shutdown.
5. The reactor core inlet and exit temperature are 610 K and <820 K.
6. Low power and temperature peaking's during nominal operation.
7. Independent reactor control (RC) and reactor emergency shutdown system (ESS).
8. Cold-clean reactivity shutdown margin $\geq$-\$1.0.
9. Independent passive decay heat removal by natural circulation of ambient air and by variable conductance heat pipes along the primary vessel wall.
10. Reactor unit and power system should be deployed on a portable platform.
11. Passive auxiliary power generation for basic plant functions, in the event of a station blackout.

3.1. VSLLIM Reactor Design and Operation Features

The VSLLIM nominal power between 1.0 -10 MW_{th} depends on the height of the in-vessel chimney, H_{ch} = 1-2 m, and the height and design of the in-vessel Na-Na heat exchanger, placed at the top of the downcomer (Fig. 3.1). The passive reactor operation and redundant control, and the redundant and passive means of removing the decay heated after reactor shutdown, would preclude a reactor core overheating or melting, by design. A higher power concept (SLIMM), with similar passive and redundant operation and safety features, that could provide 10 - 100 MW_{th} for 68 and 5.8 FPY, respectively, without refueling, has been developed by El-Genk et al., (2017). It employs taller in-vessel chimney (up to 8 m), larger in vessel Na-Na HEX, and slightly higher UN fuel enrichment (El-Genk and Palomino, 2015; Haskins and El-Genk, 2016; El-Genk et al., 2017).

Owing to the low vapor pressure of sodium, the SLIMM and VSLLIM reactors operate slightly below atmospheric pressure with a safety margin of > 450 K below the sodium boiling point (~1,156 K at 0.1 MPa). The small gap between the reactor primary and guard vessels is filled with argon gas to minimize side heat losses during nominal reactor operations (Fig. 3.4b). This gap also houses a number of sodium-leak detectors and temperature sensors, as needed.

The VSLLIM reactor will be fully fabricated, assembled and sealed in the factory, and either deployed, with the energy conversion subsystem, onto a portable (Fig. 3.2) or a floating platform or transported by rail, truck or a barge to a permanent site (Figs. 3.2, 3.1). The VSLLIM module for portable deployment uses open air Brayton cycle for electricity generation, which eliminates the needs for water cooling. At a permanent site, the VSLLIM reactor would be installed below ground, but well above the underground water table, to protect against missile or airplane impact. It will be mounted on seismic insulation bearings, to resist earthquakes (Fig. 3.1). In such a deployment, (Fig. 4.3), VSLLIM module would use a superheated steam Rankine cycle, or a supercritical CO_2 Brayton cycle (Peakman, 2018; Yu et al. 2015, Wright et al. 2011; Guo et al. 2018), for electricity generation at relatively high thermal efficiency (35-40%).

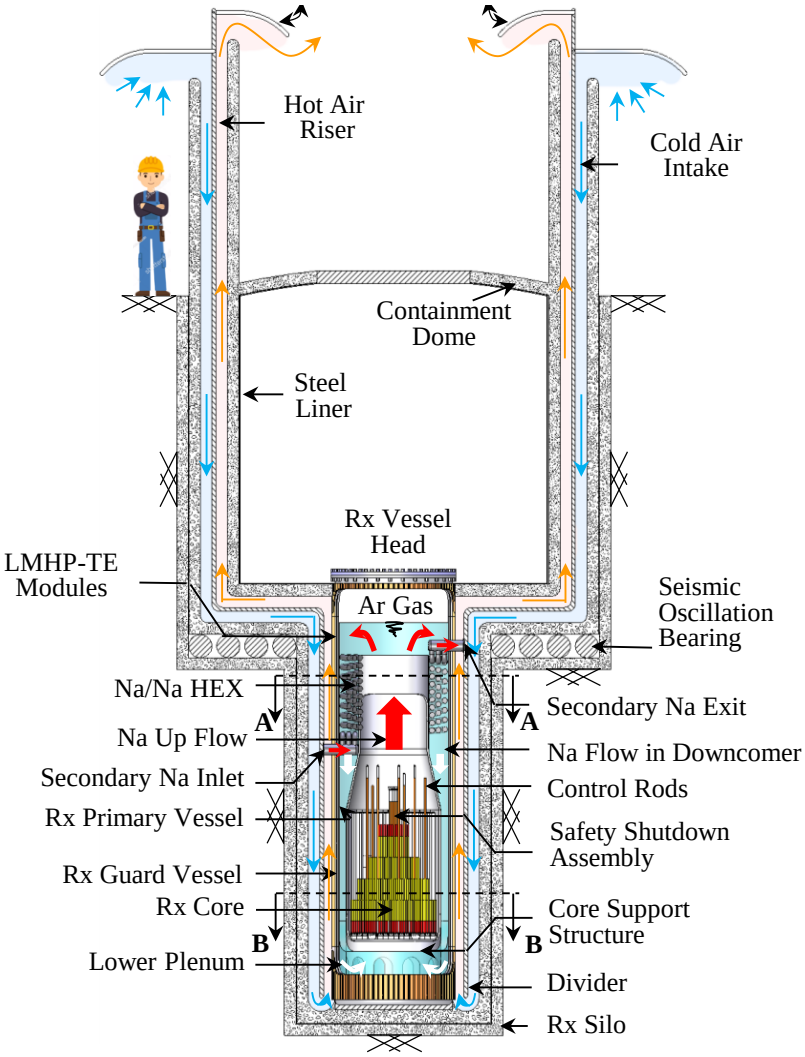

Fig. 3.1. Deployment of VSLLIM reactor at a permanent site

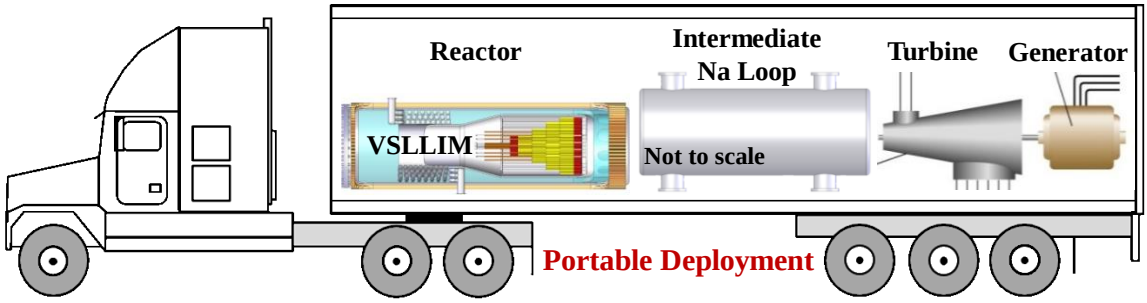

Fig. 3.2. Deployment of VSLLIM reactor and other plant components on a portable platform.

Natural circulation of in-vessel liquid sodium, passively and safely cools the VSLLIM reactor core during nominal operation and after shutdown; with the aid of in-vessel chimney (1-2 m tall) and a helically coiled tubes annular, Na-Na heat exchanger (HEX). The heat exchange is installed at the top of the downcomer to maximize the static driving pressure for natural circulation of the in-vessel liquid sodium (Figs. 3.1 and 3.3). During nominal operation, the core inlet temperature is kept at 610 K, while the exit temperature could be as high as 753 K, depending on the chimney height and the nominal power of the VSLLIM reactor (1.0-10 MW_{th}). At these temperatures the HT-9 Ferritic martensitic steel, for fuel rod cladding, core support structure, Na-Na HEX, and the reactor primary and guard vessels, is compatible with liquid sodium. The high-strength HT-9 steel (Fe-12Cr-1Mo-0.5W-0.5Ni-0.25V-0.2C) has an extensive database available on irradiation performance, making it the best choice for cladding and ducts in future fast reactors (Klueh and Nelson, 2007; Maloy et al, 2011; Caro, 2012).

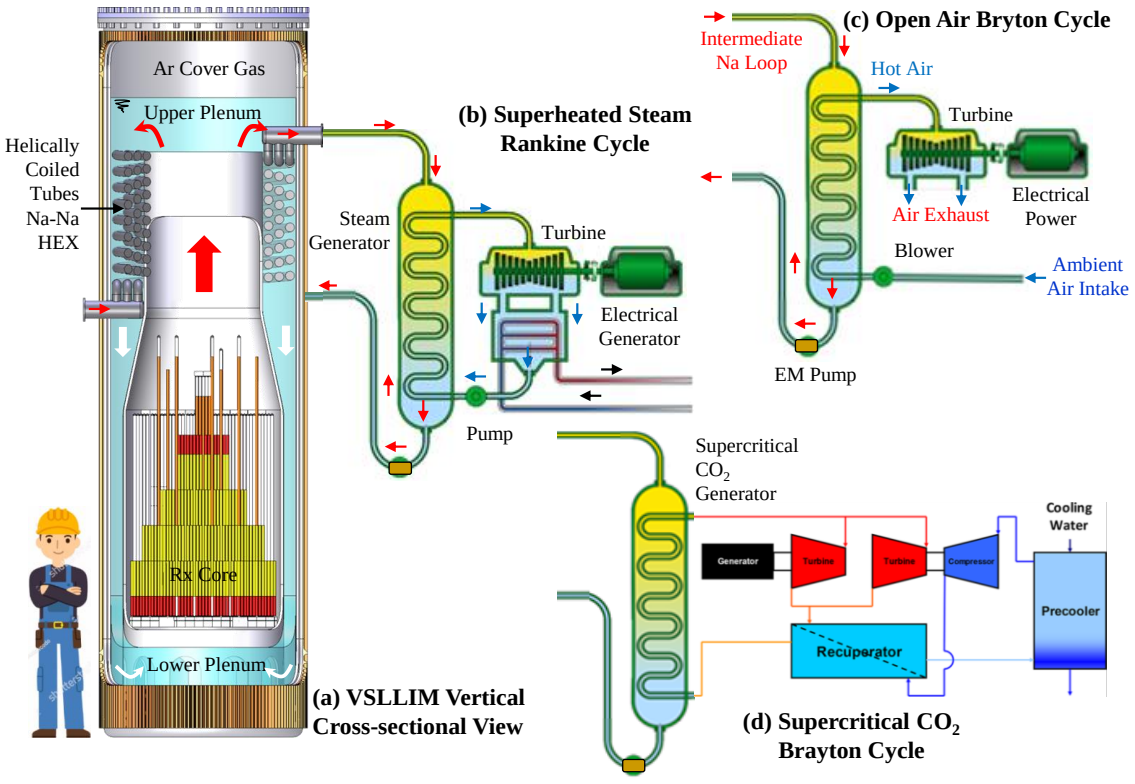

Fig. 3.3. Energy conversion options for VSLLIM installed at a permanent site.

Following an unlikely malfunction of the in-vessel Na-Na HEX (Fig. 3.3), the VSLLIM reactor shuts down by the inserting of the ESS and/or the RC B_4C rods into the

core. However, natural circulation of in-vessel liquid sodium would be maintained for removing the decay heat generated in the core, using redundant and passive means. These include: (a) the variable-conductance, liquid-metal heat pipes (LMHPs) embedded in the reactor primary vessel wall of the upper plenum (Figs. 3.3 and 3.4), and (b) natural circulation of ambient air (Palomino and El-Genk, 2016) along the outer surface of the reactor guard vessel wall (Fig. 3.1). The LMHPs, which could remove 200 - 300 kW_{th} from the reactor vessel wall, are thermally coupled to modules of thermoelectric (TE) elements. With a thermal efficiency of ~8-10% (El-Genk and Saber, 2003; El-Genk et al., 2006), the TE modules could potentially generate ~ 20-30 kW_e of auxiliary DC power, independent of on-site and off-site sources. The auxiliary power generation could support critical instrumentation and control functions, both during nominal reactor operation and after shutdown.

3.2. Reactor Core Design

The VSLLIM reactor core is loaded with hexagonal bundles of UN fuel rods clad in HT-9 steel and are arranged in a triangular lattice with P/D = 1.2. The 19 rod hexagonal bundles have scalloped BeO shroud walls (Fig. 3.5). These walls ensure equal flow area for the fuel rods in the assemblies (Figs. 3.4, 3.5). They are encased in HT-9 steel for structural support and strength, and safe handling (Hickman and Pryor, 1964). The high heavy metal atom ratio of UN helps reduce the core size and increase the operation life of the VSLLIM reactor, at relatively low fuel enrichment. This enrichment will be determined based on the results of extensive neutronics and fuel depletion parametric analyses, which are part of this research to increase BOL excess reactivity, for achieving a long full power operation life of the VSLLIM reactor.

In addition to the UN fuel enrichment, the BeO in the VSLLIM partially contributions to BOL reactivity due to neutrons production by the high energy reactions of (n, 2n) and (γ, n) in the walls of the fuel assemblies and in the radial wedges around the driver core (Fig. 3.4b). It is worth noting that the contribution of BeO to the BOL reactivity should not be a safety concern, given the redundant control and potentially the overall large negative temperature reactivity of the VSLLIM reactor.

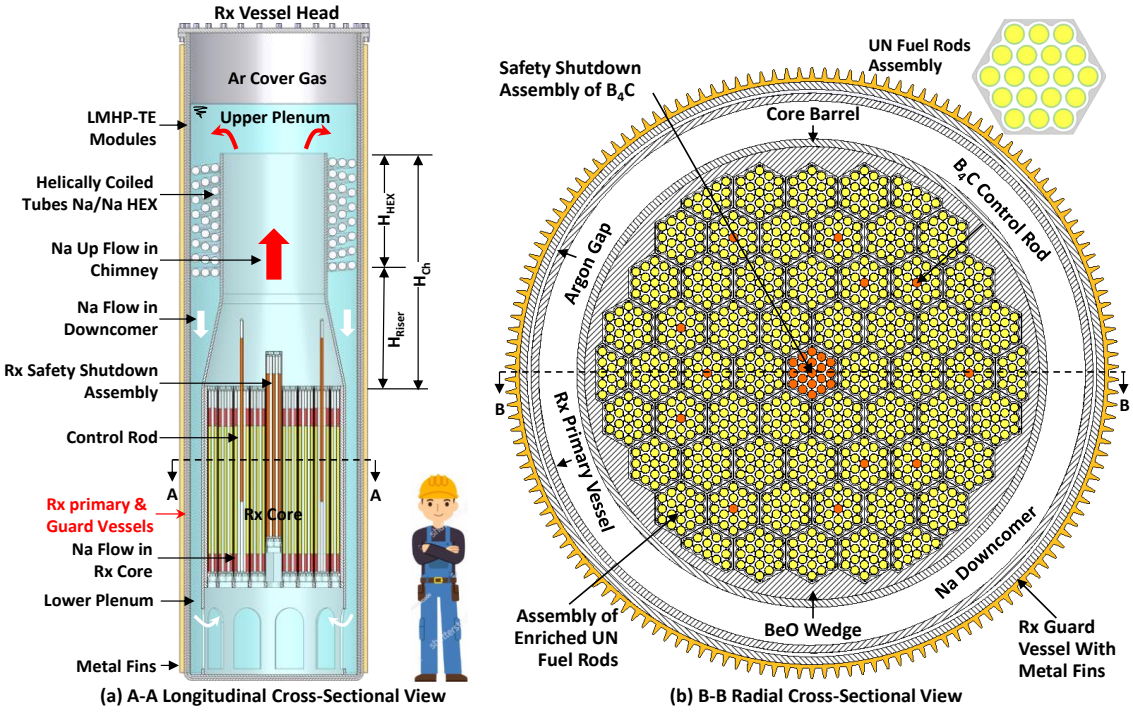

Fig. 3.4. Cross-Sectional views of the VSLLIM assembled reactor and of the core.

The UN fuel in the VSLLIM core experiences practically no swelling and fission gas release, because of its low operating temperatures, ($\leq$ 812 K) (Table 4.1). Such low temperatures are because of the low fission power density in the VSLLIM core (Table 4.2) and the high thermal conductivity of UN (Ross and El-Genk, 1988, 1990; Hayes et al., 1990; IAEA, 2008; Barret et al. 2012; Brown and Todosow, 2014). The UN fuel has been developed, fabricated and tested in the SP-100 space nuclear reactor power system program, in the 1980s and early 1990s (Matthews, et al., 1988; Makenas, et al., 1994; El-Genk, 1994; Mason and El-Genk, 1994; El-Genk and Seo, 1988).

The SP-100 space reactor power system has never been launched, but a lot of hardware development was successfully accomplished during the program. The fast spectrum and liquid lithium cooled SP-100 reactor would have operated at UN fuel temperatures up to 1900 K (Ross and El-Genk, 1988), significantly higher than the maximum UN fuel temperature than in the VSLLIM reactor (Tables 4.1, 4.2). The compatibility of UN fuel with different cladding materials in liquid Na and Li cooled reactors, has also been investigated in the space reactor program in the 1960s, 1970s and 1980s (Angelo and Buden, 1987; Mason and El-Genk, 1994; Matthews, et al., 1988;

Makenas, et al., 1994; El-Genk and Tournier, 2005). The VSLLIM reactor design benefits from the technology and gained experience in these programs and of the compiled UN properties and testing database (Ross and El-Genk, 1988, 1990; Mason and El-Genk, 1994; Matthews, et al., 1988; Makenas, et al., 1994; El-Genk, 1994; Hayes, et al., 1990).

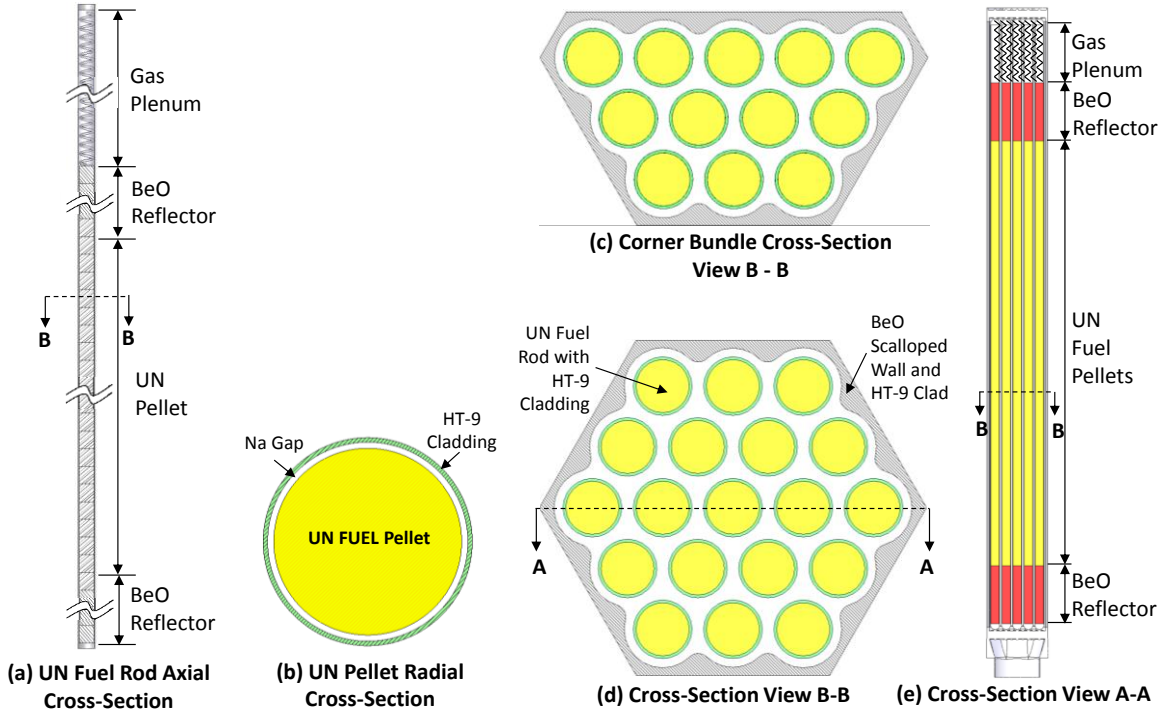

Fig. 3.5. Cross-sectional views of the UN fuel assemblies in the VSLLIM reactor core.

The driver core of the VSLLIM reactor comprises of 54, UN fuel rods full hexagonal assemblies and 6 partial assemblies. The fuel rod assemblies in the core are arranged in 4 concentric rings: six full assemblies in the first ring, 12 in the second ring, 18 in the third, and 18 full and 6 partial assemblies in the fourth ring (Fig. 3.4b). Each full assembly is loaded with 19 UN rods and the partial assembles each is loaded with 12 UN rods (Figs. 3.4, 3.5). The BeO wedges that surround the driver core assemblies serve as a radial neutron reflector, and are surrounded by the HT-9 steel core barrel (Fig. 3.4b). The radial gap in the fuel rods (Fig. 3.5b) is filled with liquid Na for good thermal coupling between the UN pellets and the HT-9 steel cladding and to accommodate the fuel pellets thermal expansion. The HT-9 steel has a good track record for operating reliably in contact with liquid sodium at temperatures between 600 and 850 K, to avoid low temperature

embrittlement and high temperature corrosion (Anantatmula and Berham, 1985; Klueh and Nelson, 2007; Maloy et al, 2011; Caro, 2012). Nonetheless, future work needs to address the issue of using H-T9 steel in the VSLLIM reactor for a long operation life.

The scalloping of the BeO shroud walls of the fuel assemblies in the VSLLIM reactor core is optimized using interactive CAD and thermal-hydraulics analyses (Fig. 3.5). The analyses also calculate the pressure losses for inclusion in the natural circulation model of the in-vessel liquid sodium in the VSLLIM reactor (Haskins and El-Genk, 2016). The design and sizing of the Na flow orifices to the fuel assemblies (Figs. 3.5e), developed using CAD analysis, are used in the CFD analyses of the pressure losses.

3.3. Reactor Control and Emergency Shutdown

The VSLLIM reactor has independent control (RC) and Emergency Safety Shutdown (ESS) systems (Fig. 3.6). The central assembly of 19 naturally-enriched (20%) B_4C rods with HT-9 cladding, is for the emergency safety shutdown of the VSLLIM reactor. This assembly has a scalloped HT-9 steel wall, and the arrangement of the B_4C rods is identical to that of the UN rods in the core assemblies (Figs. 3.5, 3.6c, d). The reactor control employs 12 B_4C rods with HT-9 cladding, for reactor startup and shutdown, and for adjusting the reactivity in the core during nominal operation. These rods are located at the center of 12 fuel assemblies in the core, three in the second ring, and nine in the third ring (Figs. 3.4, 3.6b). The three B_4C rods in the fuel assemblies in the second ring (Fig. 3.4) are 40wt% enrichment in boron-10, while the other nine rods use natural boron with 20wt% enrichment in boron-10. The guide tubes for the control rods in the core assemblies have the same outer diameter as the UN fuel rods (Fig. 3.6).

At reactor start up and during nominal operation, the ESS assembly is fully removed from the core, while the axial displacement of the 12 control rods in the core is adjusted to keep critical condition. The axial displacement of the control rods is adjusted upward with operation time, to maintain the reactor critical by compensating for the fuel burnup. At EOL, the 12 control rods would still be partially inserted in the UN fuel assemblies in the core (Fig. 3.6).

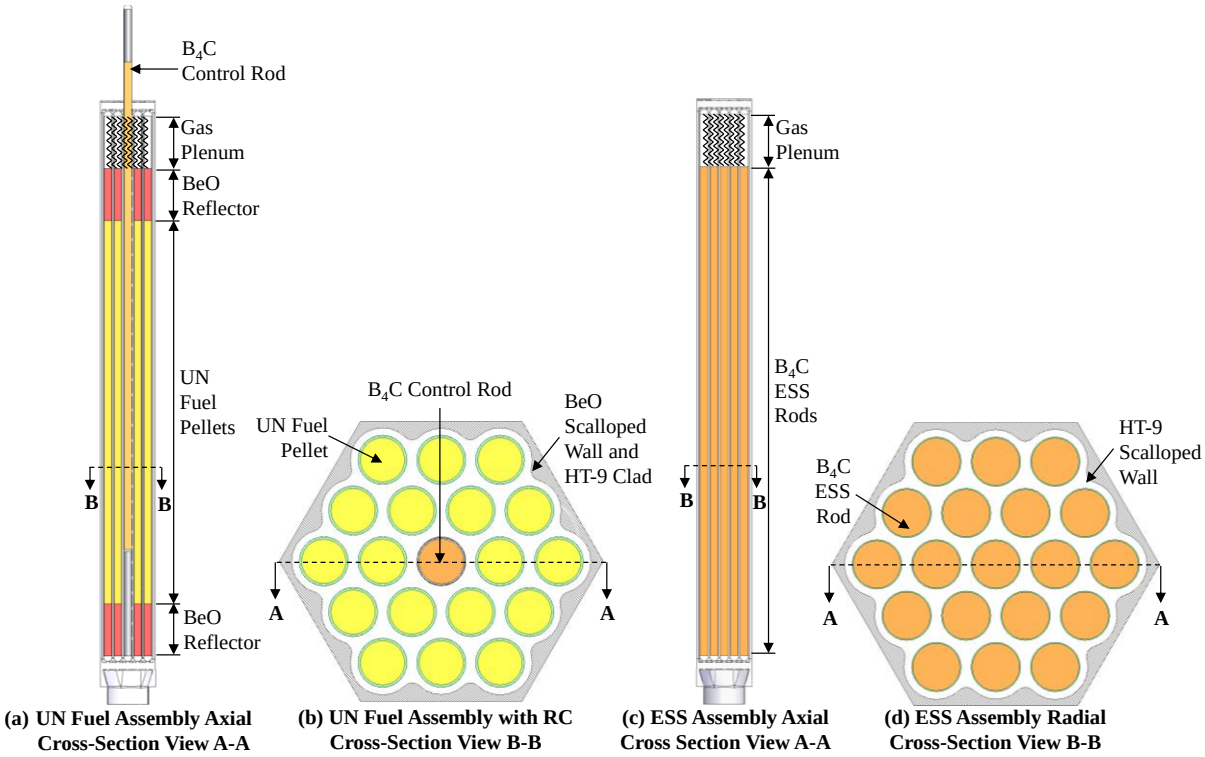

Fig. 3.6. Cross-Sectional View showing control rods placement and of ESS central Assembly.

3.4. Natural Circulation of In-Vessel Liquid Sodium

The VSLLIM reactor core is cooled by natural circulation of in-vessel liquid sodium during nominal operation and after shutdown, with the aid of in-vessel chimney (1-2 m tall), and an annular, helically coiled tubes Na-Na HEX in the downcomer (Figs. 3.1-3.4). (Haskins and El-Genk, 2016; El-Genk et al., 2017). The difference between the static heads in the downcomer and in the core and chimney drives natural circulation of the in-vessel liquid sodium. The circulation rate (Fig. 3.7) depends on the reactor thermal power, P_{Rx}, the chimney height, H_{ch}, and the height and design of the Na-Na HEX (Haskins and El-Genk, 2016). In this figure, H_{Riser} is the height of the portion of the downcomer between the HEX exit and the top of the reactor core (Figs. 3.4-3.6).

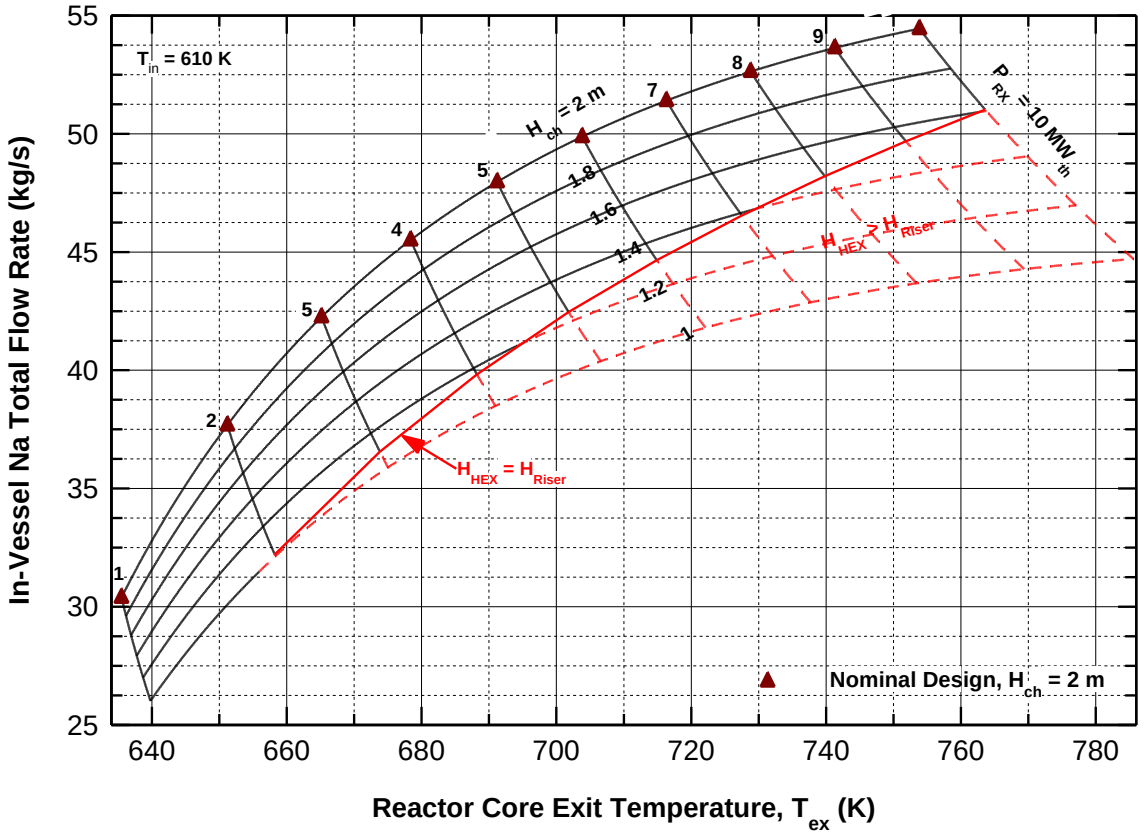

Fig. 3.7. Performance of VSLLIM reactor cooled by natural circulation of in-vessel liquid sodium.

During nominal reactor operation, in-vessel liquid sodium enters the core at 610 K. and exits at $T_{ex} \leq 760$ K, depending on the reactor thermal power and the chimney height (Fig. 3.7). These temperatures are fully compatible with the HT-9 steel cladding and core structure (Anantatmula and Bethm, 1988; Klueh and Nelson, 2007; Maloy et al, 2011; Caro, 2012). As Fig. 3.7 shows, with a 2-m tall chimney, the VSLLIM reactor power could vary from 1.0 at 10 MW_{th}, while with 1.6 m tall chimney, the reactor power could vary from 1.0 to 7 MW_{th}.

Figure 3.7 also shows that for a given chimney height, $\leq$ 2 m, decreasing the reactor thermal power decreases both the flow rate of the in-vessel liquid sodium and its core exit temperature, T_{ex}. However, at a given reactor thermal power, decreasing the in-vessel chimney height decreases the flow rate of the in-vessel liquid sodium, but increases its core exit temperature (Fig. 3.7). Therefore, with the same reactor core, the nominal thermal power of the VSLLIM reactor scales up from 1.0 to 10 MW_{th} (Fig. 3.7), by

simply increasing the height of the in-vessel chimney, up to 2 m, and the height and number of the helically coiled tubes in the Na-Na HEX (Haskins and El-Genk, 2016; El-Genk et al. 2017).

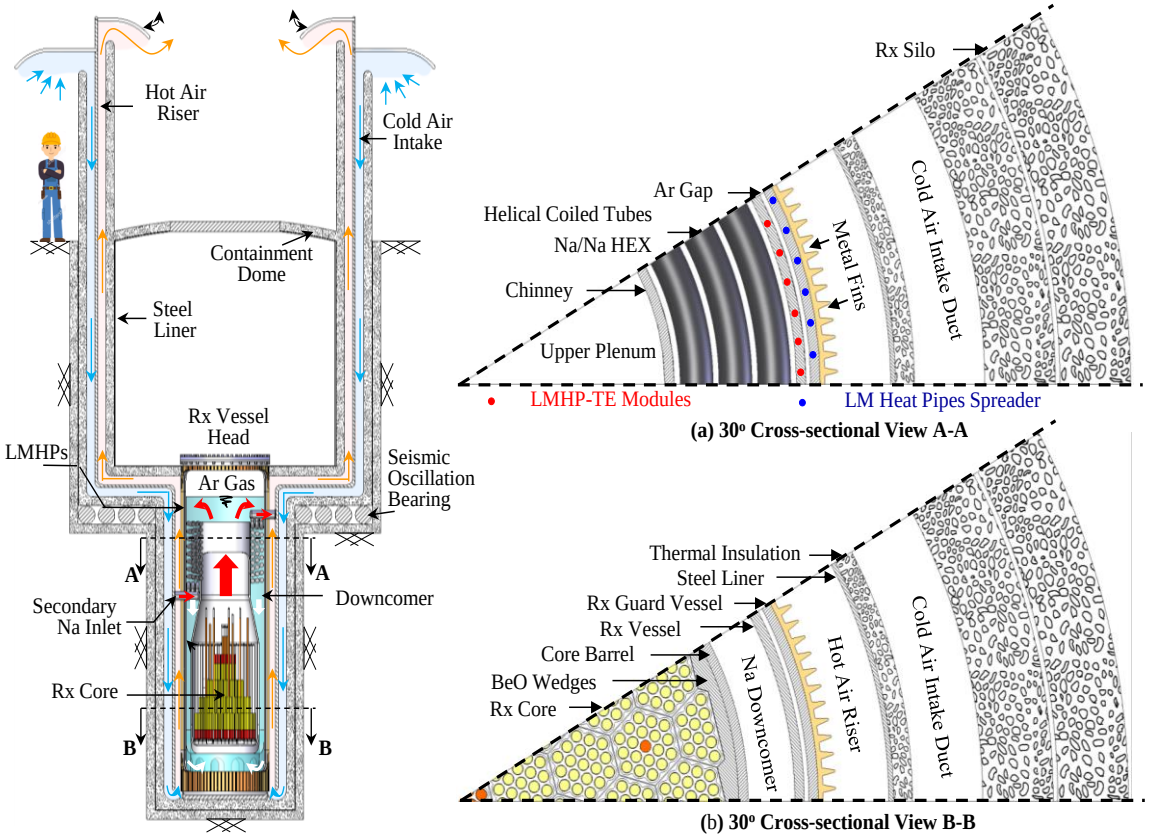

Fig. 3.8. Cross-sectional Views of the VSLLIM reactor placed at a permanent site.

3.5. Passive Decay Heat Removal and Auxiliary Power Generation

After a nominal shut down of the VSLLIM reactor, the decay heat generated in the core assemblies is removed by natural circulation of in-vessel liquid sodium, maintained by the in-vessel Na-Na HEX. However, in case of an unlikely malfunction of the HEX, the reactor shuts down, natural circulation of the in-vessel sodium is maintained using redundant and passive means for safely removing the decay heat. These are: (a) variable-conductance liquid-metal heat pipes (LMHPs) embedded in the reactor primary vessel wall of the upper plenum, and (b) natural circulation of ambient air (El-Genk et al. 2017; El-Genk and Palomino, 2015) along the outer surface of the reactor guard vessel wall (Figs. 3.1, 3.8). The heat removed by the LMHPs from the circulating liquid sodium in the upper plenum is transported passively to redundant modules of TE elements for

generating auxiliary electric power (El-Genk, et al., 2017; El-Genk and Saber, 2003; El-Genk et al., 2006; El-Genk and Tournier, 2003, 2011). The auxiliary power generation also occurs during nominal operation of the VSLLIM reactor. The LMHPs-TE modules could continuously remove several hundred kilowatts of thermal power for the reactor vessel upper plenum and generate more than 10's of kW of auxiliary DC power during nominal reactor operation and after shutdown. This auxiliary power could maintain the plant's vital functions and sensors fully operational, independent of on-site and off-site power sources (Fig. 3.8).

To activate the decay heat removal by ambient air natural circulation, the argon gas in the small gap between the primary and guard vessel in purged and replaced with liquid sodium. This enhances the heat transfer by convection from the circulating liquid sodium in the downcomer by conduction from the primary vessel wall to the guard vessel wall, where removed by ambient air natural circulation (Figs. 3.1, 3.8).

In addition, the thermal energy storage of the in-vessel sodium (5.0 Metric tons with 2-m tall chimney) slows down the riser of its temperature, immediately after shutdown, and maintains a large temperature safety margin, in excess of 450 K, from the boiling temperature of the in-vessel liquid sodium. This has been demonstrated recently for the SLIMM reactor, with an order of magnitude higher nominal thermal power than the VSLLIM reactor (El-Genk and Palomino, 2015; Palomino and El-Genk, 2016).

3.6. Summary

The **V**ery-**S**mall, **L**ong-**LI**fe, and **M**odular (VSLLIM) reactor, has been developed at the University of New Mexico's Institute for Space and Nuclear Power Studies (ISNPS), to provide 1.0 to 10 MW_{th} for electricity generation and process heat, continuously without refueling for long period of time. This scalable reactor design is capable of being factory fabricated, assembled, and sealed. In addition, on-site storage of either fresh or used fuel is not necessary, since the core is a single batch. The reactor operates fully passive, except for the reactor control (RC) and the emergency shutdown system (ESS). In-vessel natural circulation of liquid sodium cools the reactor core during nominal operation and after shutdown. The nominal reactor power between 1.0 and 10 MW_{th} depends on the height of the in-vessel chimney, H_{ch} = 1-2 m, and the height and design of the in-vessel Na-Na HEX, placed at the top of the downcomer. In case of malfunction of

the Na-Na HEX, the decay heat generated in the reactor core can also be removed safely and effectively using either natural circulation of ambient air along the outer surface of the guard vessel and/or LMHPs embedded in the upper part of the reactor primary vessel.

The VSLLIM reactor with passive operation and safety features could be transported by rail, truck or barge to a permanent site or deployed fully integrated to other power plant components, on a portable or a floating platform. In addition to the primary electricity generation, the reactor units passively generate auxiliary electric power using LMHPs-TE modules, to support critical functions during nominal reactor operation and after shutdown, independent of off-site and on-site power sources.

At a permanent site, the VSLLIM reactor is installed below ground, to protect against impact by an airplane or missiles, and mounted on seismic isolation bearing, to guard against earthquakes. For primary electric power generation, the unit module could use a superheated steam Rankine cycle or a supercritical CO_2 Brayton cycle, with a conversion efficiency of up to 40%, or even higher. As many as 10-30 units could be deployed incrementally at a single site, commensurate with the increase in electricity demand, for a plant total electricity generation of up to 120 MW_e. These VSLLIM power plant modules could also be integrated into either a distributed or a central grid, with renewable energy sources, or operated alone (Rodriguez, 2017; Locatelli et al., 2014; Lokhov et al., 2016). They can also provide both electricity and process heat for industrial uses and district heating.

The VSLLIM reactor could be integrated with all other system components at the factory and then mounted on a portable or a floating platform, for immediate deployment for operation at remote locations and to support disaster relief efforts. With an open-air Brayton cycle for electricity generation, the portable VSLLIM power modules eliminate the need for wet or dry cooling, thus are suitable for use in remote and arid communities, and remote mining and metals processing. The deployed VSLLIM power modules on floating platforms could also support deep-water mineral extraction and exploration for oil and natural gas, particularly at remote sites and in the artic.

4. NEUTRONICS AND FISSILE DEPLETION ANALYSES

This chapter presents the methodology and results for the neutronics analysis and fissile depletion of the VSLLIM reactor concept to demonstrate its potential to achieve long operation life >5 FPY without refueling. The analyses parametrically investigated the effects of changing the UN fuel enrichment and the various core materials on the cold-clean and hot-clean reactivity for the VSLLIM reactor. These materials are those of the axial reflector in the UN fuel rods (Fig. 3.5b), the radial wedges surrounding the reactor core (Fig. 3.4), and the scalloped walls of the hexagonal UN fuel rod assemblies in the core. The analyses also investigated the effect of these materials and UN fuel enrichment on the cold-clean reactivity shutdown margins for ESS and RC systems. The obtained hot-clean reactivity values are used to calculate the operation life of the VSLLIM as a function of nominal reactor thermal power from 1.0 to 10 MW_{th}.

4.1. Methodology

The criticality calculations with and without reaction rate tallies, used the Monte Carlo neutron transport code MCNP6 version 1.1 (Goorley, 2014, Brown and Kiedrowski, 2008). The calculations without reaction rate tallies used 50,000 source particles per history and 50 skipped and 1,000 active histories. Those with reaction rate tallies used 50,000 source particles per history and 50 skipped and 5,000 active histories. The calculated cold-clean reactivity is for uniform temperature of 400 K throughout the reactor core. However, the hot-clean reactivity is determined at the calculated average temperatures in the various regions of the core components, except for UN fuel it is conservatively evaluated at its maximum temperatures (Table 4.1). These temperatures vary with the nominal power of the VSLLIM reactor (1.0 - 10 MW_{th}). The large number of sources particles used in the neutronics analyses helps reduce uncertainties. The uncertainties in the calculated cold-clean and hot-clean k_{eff} values for the VSLLIM driver core are very small, ranging from 0.0004 – 0.00008.

Table 4.1 lists the calculated temperatures in the VSLLIM reactor core at a nominal power of 10 MW_{th}. These temperatures are based on single channel CFD and thermal-hydraulics analyses for each ring of UN fuel assemblies in the core. The analyses assumed sinusoidal axial distribution of the fission power and varied the coolant mass

flow rate commensurate with the fraction of the total reactor thermal power generation in each of rings of the core UN fuel assembles in the core. The low average UN fuel temperatures in Table 4.1 are because of the low fission power density in the VSLLIM reactor core and the high thermal conductivity of the UN (Ross and El-Genk, 1988; Hayes, et al., 1990). At such low temperatures, the UN fuel swelling and the release of fission gasses from the fuel pellet are negligible (Ross and El-Genk, 1990). To avoid distorting the neutron flux profile in the core and removing the tally dependence on k_{eff}, the calculations of the neutron reaction rates, flux tallies, and energy spectrum in the VSLLIM reactor core are performed at critical hot condition ($k_{eff} = 1.0$).

Table 4.1. Calculated temperatures in the VSLLIM core at nominal reactor power of 10 MW_{th}.

Reactor Core Region	**Calculated Temperatures (K)**			
	Ring 1 Assemblies	**Ring 2 Assemblies**	**Ring 3 Assemblies**	**Ring 4 Assemblies**
UN Fuel	814	804	786	770
Na Gap in UN Rods	755	755	755	754
HT-9 Steel Cladding	754	754	754	754
Lower BeO Reflector	610			
Upper BeO Reflector	754			
Sodium Coolant	681			
HT-9 Core Structure	681			
Core Radial BeO Wedges	681			

For calculating the neutron energy spectrum and the spatial distribution of the fission power in the UN fuel assemblies (Fig. 3.5a) in the VSLLIM driver core is divided into 4 concentric rings and 55 axial sections. In these sections, the tallies for the fission power in the UN fuel and the neutron energy spectrum are calculated using the MCNP6 code version 1.1 (Goorley 2014). This code is also used to tracks the fissile production and depletion in the core throughout the reactor's operation life, and as functions of the reactor nominal thermal power (1.0 - 10 MW_{th}).

The values of the temperature reactivity feedback in the VSLLIM reactor core are also obtained using the MCNP6 code. These are those due to the thermal expansion of

UN fuel, liquid Na and the BeO, and the Doppler broadening of the neutron cross-sections for the UN fuel and various materials in the reactor core. The various estimates of the temperature reactivity feedback are determined separately at mean temperatures of 400 K, 600 K, 800 K, 900 K, 1000 K, and 1200 K, while keeping the rest of the reactor core at a reference temperature, T_{ref}, of 400 K.

4.2. Results and Discussion

The performed neutronics analyses parametrically investigated the effects of changing the UN fuel enrichment on both the cold-clean and hot-clean excess reactivity and on the cold-clean reactivity shutdown margins for the ESS and RC systems (Fig. 4.1). These reactivity shutdown margins are conservative, since the reactor would typically shuts down from a hot condition, whereas the accumulated fission products in the fuel and the negative temperature reactivity feedback in the core would increase the negative reactivity shutdown margins. The hot-clean excess reactivity results in Fig. 4.1 are for the VSLLIM reactor at nominal thermal powers of both 1.0 and 10 MW_{th}, and with 2-m tall in-vessel chimney (Fig.3.7 and Table 4.1).

4.3. Parametric Analyses

The results in Fig. 4.1a show that increasing the UN fuel enrichment in the core, from 13.65% to 13.85% increases both the cold- and the hot-clean excess reactivity and decreases the cold-clean reactivity shutdown margins (k_{eff} - 1). These margins for RC are negative 0.0126, 0.0094, and 0.0068 with UN fuel enrichment of 13.65%, 13.76% and 13.85%, respectively. The corresponding cold-clean reactivity shutdown margins for ESS are negative 0.0161, 0.0129, and 0.0103, respectively. The cold-clean excess reactivity in the VSLLIM reactor core with UN fuel enrichment of 13.65%, 13.76% and 13.85%, is 0.0241, 0.0273, and 0.0298, respectively. However, the corresponding hot-clean excess reactivity values are much lower; 0.0033, 0.0067, and 0.0094, respectively. For all UN fuel enrichments investigated in Fig. 4.1a, the RC and ESS cold-clean negative reactivity shutdown margins are more than adequate for safe reactor shutdown. The RC cold-clean reactivity shutdown margin decreases slightly with increasing the UN fuel enrichment to 13.76%, but is still considered adequate.

The cold- and hot-clean excess reactivity values (k_{eff} - 1) increase with increased UN fuel enrichment at an average rate of ~0.0287/wt%-^{235}U, thus a small increase in the UN fuel enrichment results in large increases in both the cold- and hot-clean excess reactivity values (Fig. 4.1a). Increasing the UN fuel enrichment, from 13.65% to 13.85%, increases of hot-clean excess reactivity by ~0.0057. With an enrichment of 13.65%, the hot-clean excess reactivity of only 0.0033 is insufficient for a long operation life. However, with UN fuel enrichment of 13.85%, the hot-clean excess reactivity of 0.0094 is sufficient for achieving longer operation life, but the corresponding cold-clean reactivity shutdown margin is the lowest (Fig. 4.1a).

Based on the parametric analyses results in Fig. 4.1a, a UN fuel enrichment of 13.76% ensures high enough hot-clean excess reactivity (0.0067) for a long operation life and sufficient cold-clean reactivity shutdown margin, thus was selected for the VSLLIM reactor nominal design. At this fuel enrichment, the hot-clean reactivity is ~ 0.0142 lower than the cold-clean reactivity at 10 MW_{th}. This difference is due to the Doppler broadening of the neutrons cross-sections and the thermal expansions of the UN fuel, the HT-9 cladding, the in-vessel liquid Na, and the BeO axial reflector and core wedges, and other core HT-9 structural materials. At a nominal thermal power of 1.0 MW_{th}, the hot-clean excess reactivity for the VSLLIM reactor is ~57% higher than at 10 MW_{th} (Fig. 4.1a). This is because the lower operating temperatures at the lower reactor thermal power decrease the contribution of the negative temperature reactivity feedbacks in the core.

The parametric analyses results in Fig. 4.1b show the effect of using depleted uranium nitride (DUN), BeO, or HT-9 steel as the top and bottom axial reflectors in the fuel rods (Fig. 3.5), with the selected UN fuel enrichment of 13.76%. The results are compared to those without a solid axial reflector, but with liquid sodium (Na). The cold-clean reactivity shutdown margins with BeO, HT-9, DUN, and liquid Na axial reflectors are adequate for safe shutdown of the VSLLIM reactor. However, with the BeO reflectors, the hot-clean reactivity (k_{eff} - 1) is positive 0.0067, compared to negative 0.0028, 0.0069, and 0.0050, with HT-9, DUN, and Na reflectors, respectively. Therefore, the BeO axial reflector is an acceptable choice for the axial reflectors with 13.76% UN fuel enrichment (Fig. 4.1b).

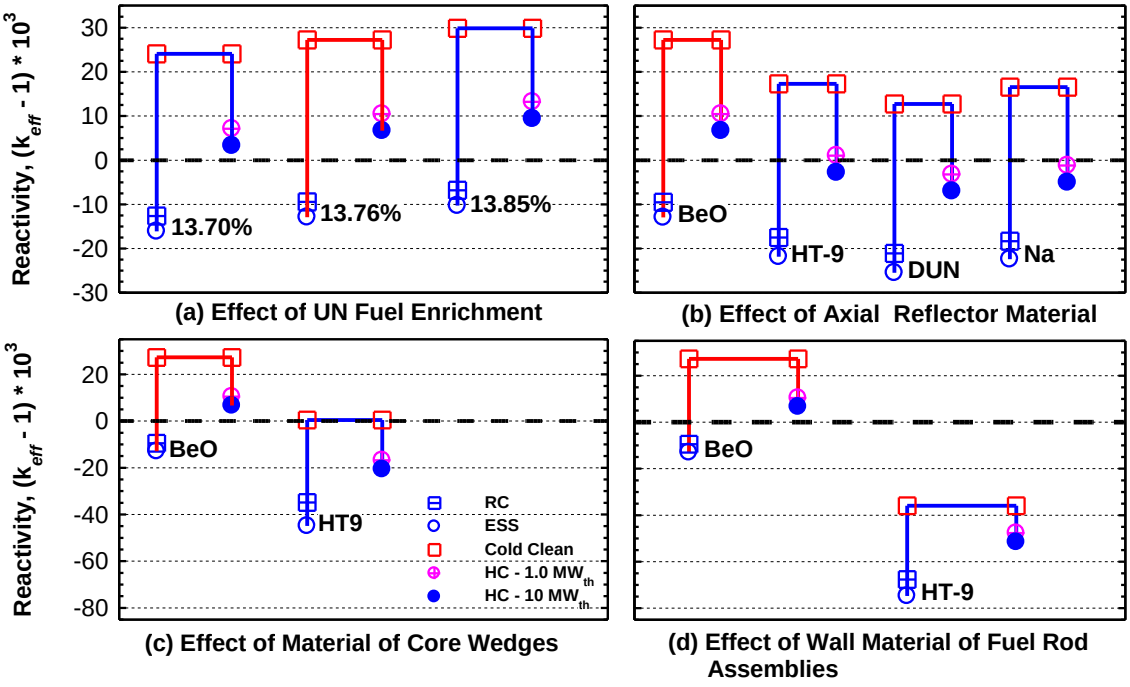

Fig. 4.1. Effect of Different Core Materials on hot- and cold-clean excess reactivity and cold-clean reactivity shutdown margins for the VSLLIM reactor.

The results in Figs. 4.1c show that using radial BeO wedges in the core (Fig. 3.4) increases the cold- and the hot-clean excess reactivity (k_{eff} - 1) values compared to using HT-9 steel wedges, by ~0.0268. Consequently, the cold-clean reactivity shutdown margin with HT-9 steel wages is much smaller than that with BeO wedges, and the hot-clean reactivity is insufficient. Thus, the BeO wedges are selected for the nominal design of the VSLLIM reactor (Fig. 4.1c).

The parametric analyses results in Fig. 4.1d show that using BeO shrouds for the hexagonal UN fuel rod assemblies in the core (Figs. 3.5) helps increase the cold- and the hot-clean reactivity values, with adequate cold-clean reactivity shutdown margins for ESS and RC systems. Using HT-9 steel shrouds, however, is unacceptable because of the negative cold- and hot-clean reactivity values. With BeO shroud walls, the cold-clean excess reactivity is 0.0272, compared to negative 0.0359 with HT-9 steel shrouds (Fig. 4.1d). This is because of the high parasitic neutron absorption in the HT-9 steel, as contrasted to the BeO (El-Genk and Palomino 2015). Besides, the high energy (γ,n) and (n,2n) reactions in BeO increase the neutron population in the reactor core by ~1.4% and the moderating effect of the beryllium increases the neutron fission cross in the core.

Based on the results of the parametric analyses presented in Figs. 4.1a - c, with a UN fuel enrichment of 13.76%, BeO is the optimal choice for the axial reflectors in the UN fuel rods, the walls of the UN fuel rod assemblies, and the radial wedges surrounding the core loaded with UN fuel assemblies (Fig. 3.4).

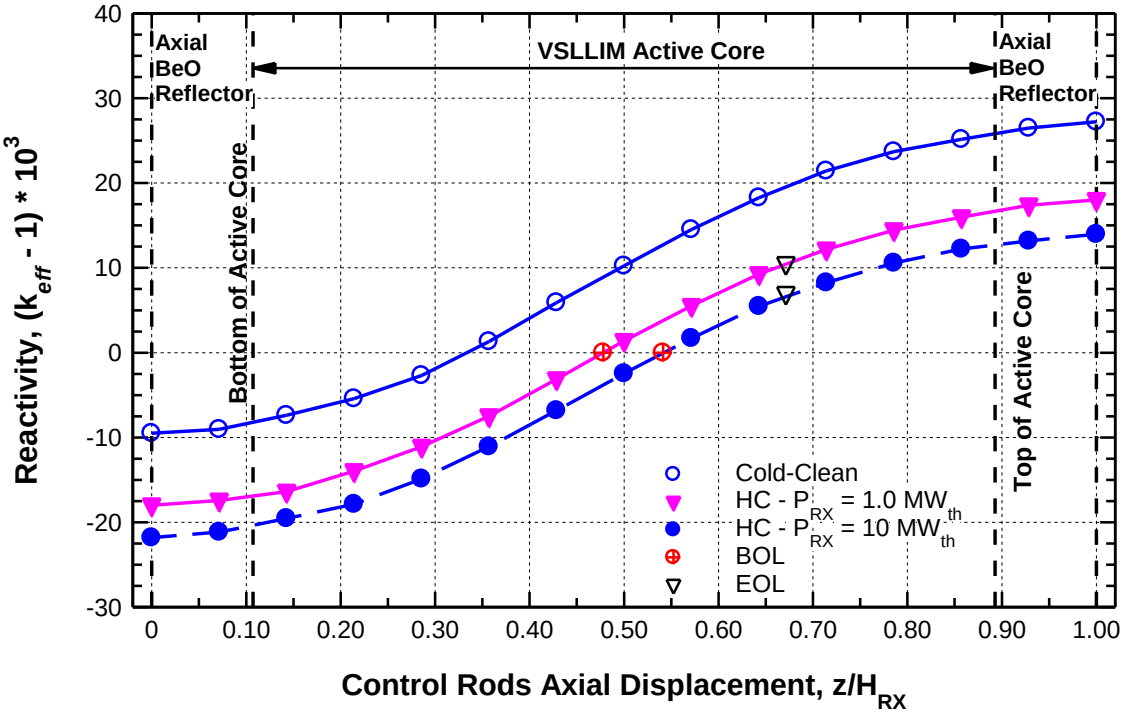

Fig. 4.2. Estimate of BOL and EOL axial displacements of the control rods in the VSLLIM core.

The determined EOL axial displacements of the 12 B_4C control rods, inserted at the center of the UN fuel assemblies in ring 2 and ring 3 of the VSLLIM core (Fig. 3.4), are presented in Fig. 4.2, at nominal powers of 1.0 and 10 MW_{th}. These results are for the nominal VSLLIM reactor design with UN fuel enrichment of 13.76%, BeO walls for the UN fuel assemblies, axial reflectors, and the radial wedges, and with HT-9 steel cladding, core support structure, and reactor primary and guard vessels (Figs. 3.1-3.4). In Fig. 4.2, a displacement of $z/H_{RX} = 1$ of the control rods in the UN fuel assemblies indicates that the control rods are fully removed from the fuel assemblies, while a displacement $z/H_{RX} = 0$ indicates that the control rods are fully inserted into the fuel assemblies. The calculated cold-clean reactivity (k_{eff}-1) is positive 0.0272, and negative 0.0095, when the control rods are fully removed and fully inserted in the core fuel assemblies, respectively.

The effect of the axial displacement of the control rods on the cold-clean reactivity is the highest in the middle of the active core, z/H_{RX} = 0.1 - 0.9, and the lowest near the bottom, $z/H_{RX} \leq 0.1$, and the top, $z/H_{RX} \geq 0.9$ of the core, with axial BeO reflectors in the UN fuel rods. For nominal reactor thermal powers of 1.0 and 10 MW_{th}, the BOL displacement of the control rods in the VSLLIM core with UN fuel assemblies is z/H_{RX} = 0.48, and 0.54, respectively. At EOL, the axial displacement of these control rods is z/H_{RX} = 0.67, regardless of the nominal reactor thermal power (Fig. 4.2).

4.4. Neutron Energy Spectrum and Spatial Distributions of Flux and Fission Power

Figure 4.3a, b present the calculated BOL neutron energy spectra in the VSLLIM reactor core during nominal operation at 10 and 1.0 MW_{th}, respectively. Fig. 4.3a compares the energy spectra for the whole core and the UN fuel assemblies in ring 1- 4 (Fig. 3.4) at 10 MW_{th}, to that of prompt, fission, for reference. Results confirm that the VSLLIM reactor core has a relatively soft fast neutron energy spectrum with a most probable value of ~136 keV, compared to ~0.72 MeV for the prompt fission neutrons (Fig. 4.3a).

The neutron energy spectra for the UN fuel assemblies in rings 1, 2 and 3 are harder than the energy spectrum for the assemblies in ring 4 of the core. However, the energy spectrum for the fuel assemblies in ring-4 has larger fractions of epi-thermal and slow neutrons (0.1 eV-1.0 keV). This is due to the neutrons being moderated by the beryllium in the shrouds of the fuel assembles and the radial wedges surrounding the core (Figs. 3.4, 3.5). This spectrum also has a larger fraction of high energy neutrons (> 0.1 MeV) because of the neutrons production by (γ, n) and (n, 2n) reactions in the BeO wedges. Over all, the VSLLIM core has generally the same energy spectra at 1.0 and 10 MW_{th} (Fig. 4.3b), with a small tail of epi-thermal and slow neutrons, which contributes to increasing the average fission cross-section and the BOL excess reactivity.

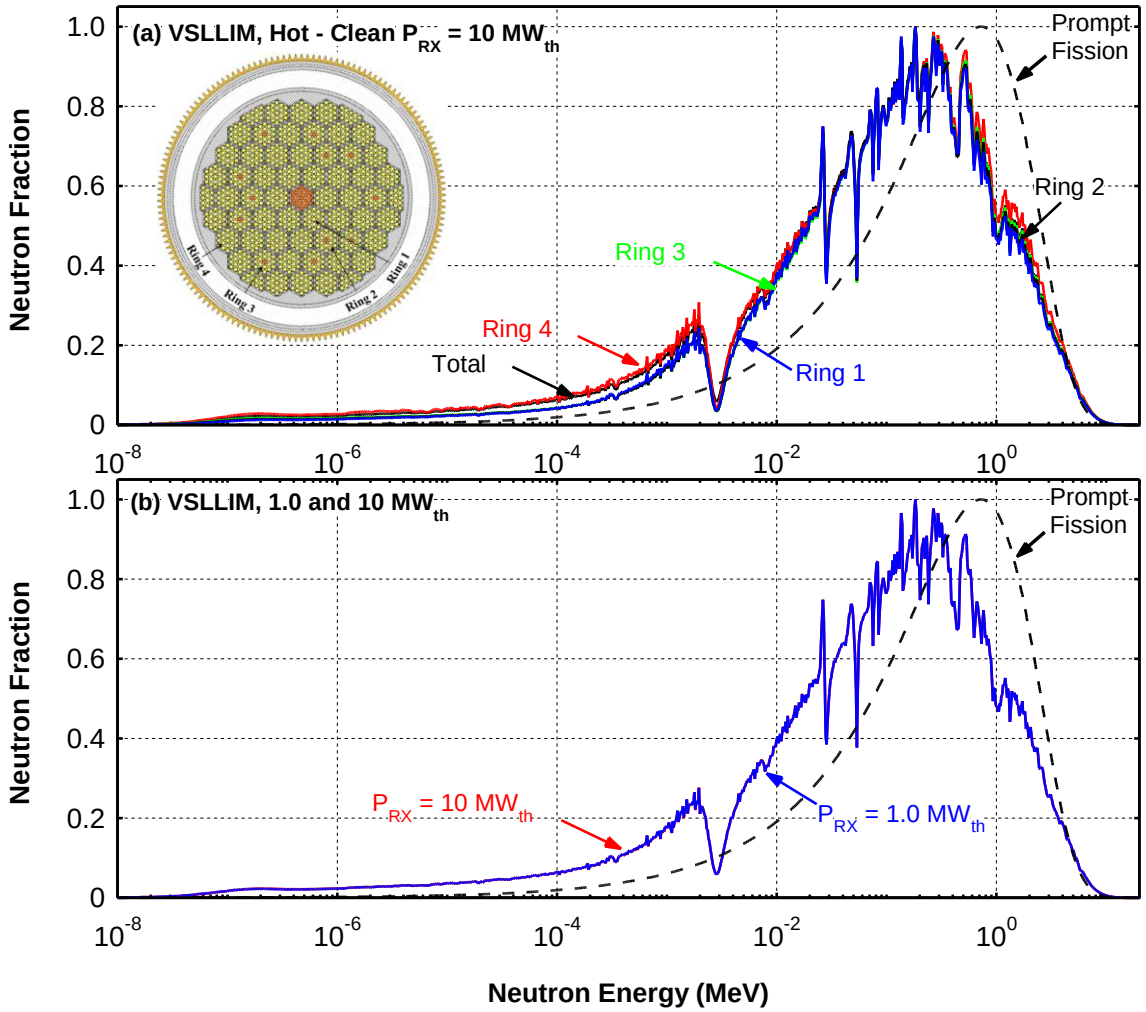

Fig. 4.3. Neutron energy spectra for the VSLLIM reactor core at 1.0 and 10 MW_{th}.

The calculated BOL radial and axial distributions of the neutron flux in the VSLLIM reactor core at 10 MW_{th}, are presented in Fig. 4.4a,b. These distributions correspond to an axial displacement of the control rods in the UN fuel assemblies, $z/H_{RX} = 0.54$ (Fig. 4.2). Fig. 4.4a compares the normalized radial neutron flux distributions at different axial locations, z/H_{RX} = 0.11, 0.30, 0.50 (core mid-plane), 0.70, and 0.89. There are steep drops in the normalized radial flux distribution at z/H_{RX} = 0.70 and 0.89, which correspond to the radial locations of the B_4C control rods inserted in the UN fuel assemblies in rings 2 and 3 (Fig. 3.4). Results in Figs. 4.4b show that the BOL normalized axial neutron flux distribution peaks at $z/H_{RX} = 0.45$, which is slightly below the core mid plane. This is because the control rods are partially inserted into the reactor core from the top to $z/H_{RX} = 0.54$.

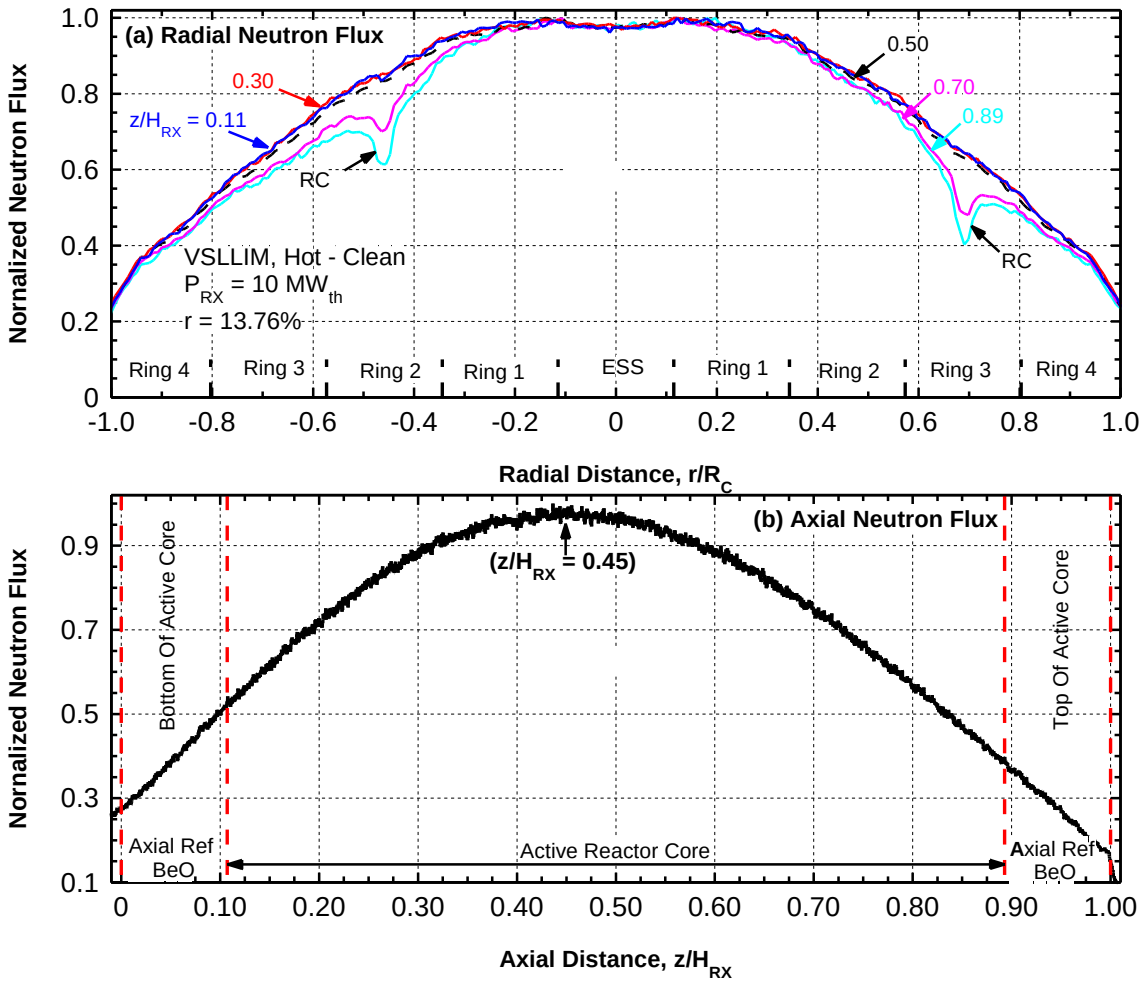

Fig. 4.4. BOL radial and axial flux distributions in VSLLIM reactor core at 10 MW_{th}.

A desirable operation and safety feature is low peak fission power density (23.47 MW/m^3, Table 4.2) and, hence, low maximum temperature in the UN fuel rods (~812 K) at a VSLLIM reactor nominal thermal power of 10 MW_{th}. The low peak power density would improve the fuel utilization in the core and reduce stress in the fuel rods. At a nominal power of 10 MW_{th}, the calculated BOL and EOL radial fission power profiles in the VSLLIM reactor core show that the fission power density in the UN fuel rods in ring 1, that are closest to the center assembly for ESS. This fission power density peaks at 39.92 W/cm^3 (Fig. 4.5a). This figure also compares the fractions of the fission power generated in each of the four rings of UN fuel assemblies in the VSLLIM reactor core.

When the VSLLIM reactor operates at 10 MW_{th}, the BOL percentages of the total fission power generated in the fuel assemblies in ring 1 to 4 are 14.21%, 24.70%,

29.24%, and 31.85% respectively. The corresponding percentages at EOL are very similar; 14.09%, 24.65%, 29.45%, and 31.81%, respectively. At EOL, the control rods in the core fuel assembles move up to z/H_{RX} = 0.67 (Fig. 4.2) to compensate for the reactivity loss due to fuel burnup. This in turns shifts the EOL peak fission power density of 39.53 W/cm^3 to z/H_{RX} = 0.46 (Fig. 4.5a).

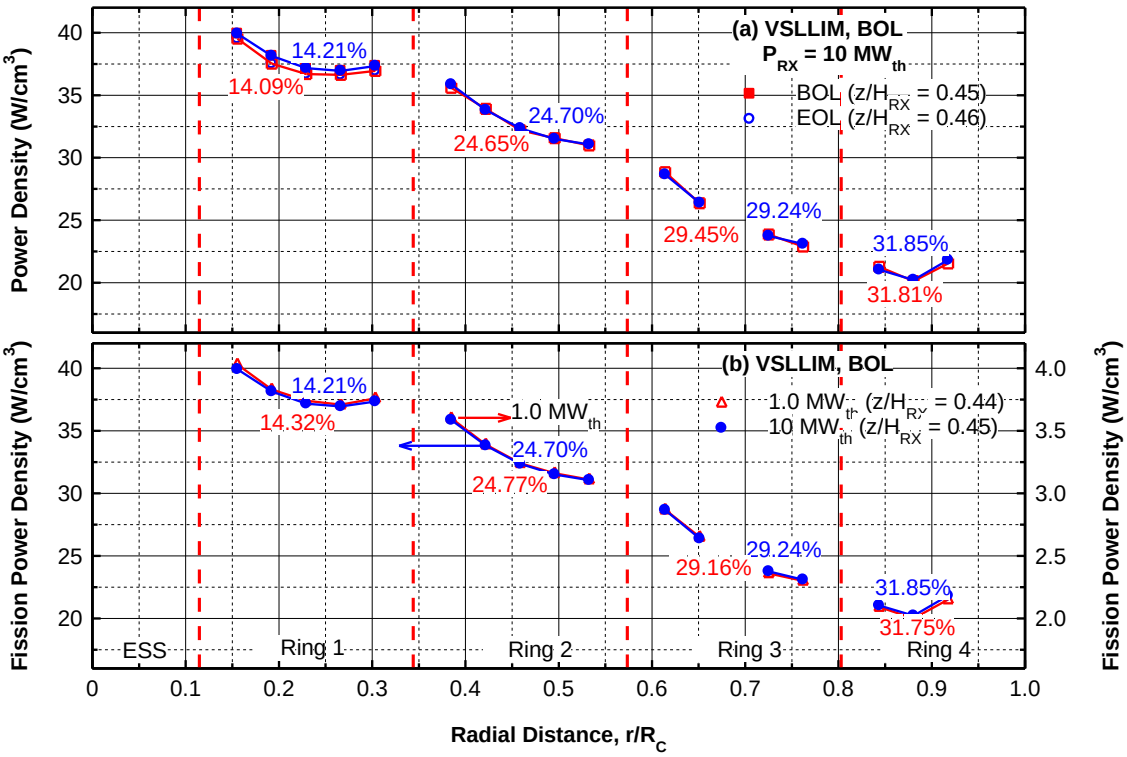

Fig. 4.5. Calculated BOL and EOL radial distributions of the fission power density in VSLLIM reactor core at 1.0 and 10 $MW_{th.}$

Figure 4.5b compares the calculated BOL radial distributions of the fission power density in the VSLLIM core at 1.0 and 10 MW_{th}. The peak power densities at these reactor powers are 4.03 and 39.92 W/cm^3, respectively, and both occur at the same radial location, r/R_C = 0.15. At 1.0 MW_{th}, the peak axial fission power density in the VSLLIM core occurs at a lower axial location of z/H_{RX} = 0.44. This is because the control rods are inserted further into the UN fuel assemblies (z/H_{RX} = 0.48) than at 10 MW_{th}. The percentages of the BOL total fission power generated in the UN fuel assemblies in rings 1- 4 at 1.0 MW_{th} and 10 MW_{th} are practically the same (14.32%, 24.77%, 29.16%, and 31.75% respectively).

Figures 4.6a compares the BOL and EOL axial distributions of the fission power density for the hottest fuel rod (r/R_C = 0.15) in the core at a nominal reactor power of 10 MW_{th}. At this power, the BOL and EOL peak axial fission power densities are 39.87 and 39.658 W/cm^3, and occur at z/H_{RX} = 0.45 and 0.46, respectively. In the middle region of the core, these axial profiles resemble a cosine function, except for the steep rises near the top and bottom of the core. These raised in fission power density are due to the neutron production by the (γ, n) and (n, 2n) reactions in the axial BeO reflectors in the fuel rods. Similar effect can be seen in Fig. 4.5 for the fuel rod assembles in ring-4, which are closest to the radial BeO wedges (r/R = 0.92).

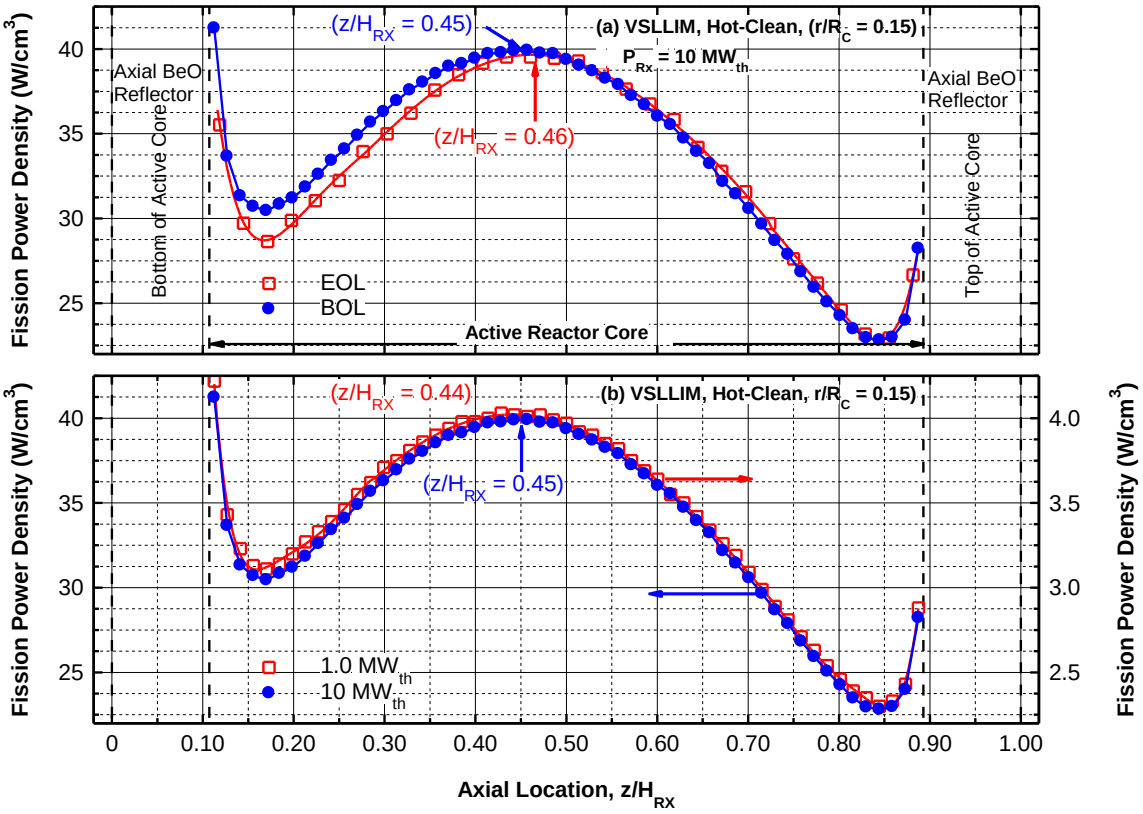

Fig. 4.6. Axial fission power density profiles for the hottest fuel rod in the VSLLIM core.

The results in Fig. 4.6b show that the EOL axial profile of the fission power density in the VSLLIM core at 10 MW_{th} is slightly higher than at 1.0 MW_{th} in the lower half of the core, but lower in the upper half. This is due to the higher accumulation of the fissile Pu isotopes in the fuel rod with burnup. At BOL, the axial profiles of the fission power

density at 1.0 and 10 MW_{th} are very similar, and ratio is the same as that of the reactor powers.

4.5. Temperature Reactivity Feedback Effects

The MCNP6 Code is used in the Neutron Photon mode, with the photonuclear physics enabled, to calculate the temperature reactivity feedback for the UN fuel, sodium coolant, and different core materials at mean temperatures of 400 K, 600 K, 800 K, 900 K, 1000 K, and 1200 K. These calculations used 50,000 source particles per cycle, and 50 skipped and 2000 active cycles. The temperature reactivity feedback due to Doppler broadening of the neutrons cross sections is determined using the MAKXSF cross section processing utility for the ENDF VII.1 cross sections libraries (Brown, 2006; Chadwick, 2006; Mosteller et al., 2003; Mosteller, 2008).

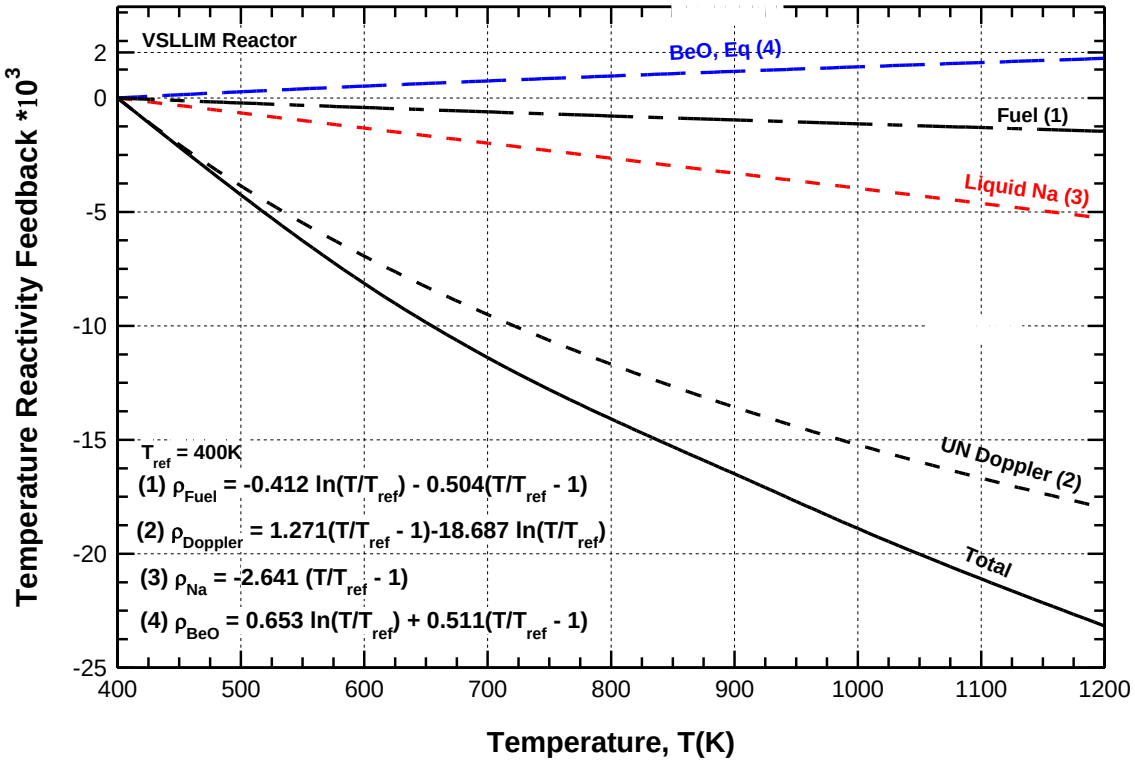

Fig. 4.7. Estimates of different temperature reactivity feedbacks in VSLLIM reactor core.

The estimates of the temperature reactivity feedback are determined by subtracting the calculated reactivities for the different core materials, one at a time, at the different temperatures, from those calculated at a reference temperature, T_{ref} = 400 K, throughout the core. This temperature is slightly higher than the melting temperature of sodium at

atmospheric pressure (371 K) (Thermal Fluids Central, 2016; Bomellburg et al. 1972; Foust, 1972).

The obtained temperature reactivity feedback estimates are those due to the decreases, with increased temperature, in the densities of the UN fuel, in-vessel liquid sodium, HT-9 cladding (Fig. 3.4), and the BeO in the walls of the UN fuel assembles (Fig. 3.5), axial reflectors and core wedges, as well as that due the Doppler broadening of the neutrons cross sections. The temperature reactivity feedback estimates for the BeO in the reactor core are calculated at the same average temperatures of the in-core liquid sodium. That for the UN is the sum of those calculated at the mean temperatures of the fuel rods in the assemblies in rings 1-4 of the reactor core.

The temperature reactivity feedback for each core material is calculated at different temperatures, while keeping the rest of the reactor core at the reference temperature (T_{ref} = 400 K). Each estimate is the sum of those due to thermal expansion. The obtained temperature reactivity feedback estimates in the VSLLIM core as a function of temperature up to 1200 K, are compared in Fig. 4.7. This figure shows that the contribution of the HT-9 cladding is very small (~.0014), and that of the HT-9 core structure is negligibly small (El-Genk et al., 2017).

The positive temperature reactivity feedback due to the BeO axial reflector and the wedges, between the core assemblies and the HT-9 core barrel, is small compared to the total negative temperatures reactivity feedback for the driver core (Fig. 4.7), to raise a concern about the reactor control or safety. It is also worth noting that the contribution of the BeO to the total neutrons population is the VSLLIM core during nominal operation constitutes less than 1.4%. The passive operation and redundant control, the large total negative reactivity feedback, and the redundant and passive means of removing the decay heated after shutdown, would preclude a reactor core overheating or melting, by design.

The total temperature negative reactivity feedback in the VSLLIM core is large (negative 0.0213 at 1100 K), which is desirable for safety consideration (Fig. 4.7). This is consistent with the values reported for the SLIMM reactor, which is similar in design, but operates at 10 times the nominal thermal power for VSLLIM (El-Genk et al., 2017). The safety analysis results for the SLIMM reactor have shown that, following an unlikely malfunction of the in-vessel Na-Na HEX and both the ESS and RC systems, the core

negative temperature reactivity feedback alone would safely and passively shut down the reactor (Schriener and El-Genk, 2018).

The results in Fig. 4.7 also show that for the UN fuel, the temperature reactivity feedback due to the Doppler broadening at 1200 K is negative 0.0185, compared to only negative 0.0014 due to the thermal expansion. The Doppler reactivity feedback is the largest contributor to the total negative temperature reactivity feedback in the VSLLIM reactor core. The thermal expansion of the BeO in the core has a small positive temperature reactivity feedback of ~ 0.0018 at 1200 K. The in-vessel liquid Na has a negative temperature reactivity feedback of ~ 0.0053 at 1200 K. As such temperature, the in-vessel liquid sodium in the reactor would still be sufficiently below its boiling point. This is partially because the corresponding thermal expansion of the in-vessel liquid sodium would increases the pressure of the argon cover gas in the reactor primary vessel, and hence the boiling temperature of sodium (Figs. 3.1-3.4). The sodium temperature reactivity feedback is the net sum of the negative reactivity due to thermal expansion and the positive reactivity feedback due to the decrease in neutron capture in sodium as its density decreases with temperature.

4.6. Operation Life Time Estimate

The estimates of the VSLLIM reactor operation life are those for continuous operation without refueling at nominal powers from 1.0 to 10 MWt_h. These estimates are obtained using MCNP6 code version 1.1 (Goorley, 2014). It performs the burnup calculation using CINDER90, a nuclide inventory code, which tracks the fissile depletion, the production and accumulation of fission products, and the transmutation of the different nuclides by neutron capture and radioactive decay (Pelowitz, 2011). Through the BURN card, the user inputs the reactor thermal power and the size of the burn time step in days. MCNP6 performs criticality calculations of k_{eff} at the beginning and at the end of each time step.

The CINDER90 code offers three options, or tiers, for tracking the different isotopes of fission products in the VSLLIM reactor core. Tier (1) tracks the 12 most common fission products, tier (2) track 87 fission product isotopes and tier (3) track 220 fission product isotopes (Pelowitz, 2011). Increasing the number of the fission isotopes to be tracked, increases the running time, but improves the accuracy of the results (El-Genk

and Palomino 2015, El-Genk et al., 2017). The tier (3) option is used in the present burnup calculations and the operation life estimates for the VSLLIM reactor, as a function of the nominal thermal power (1.0 - 10 MW_{th}).

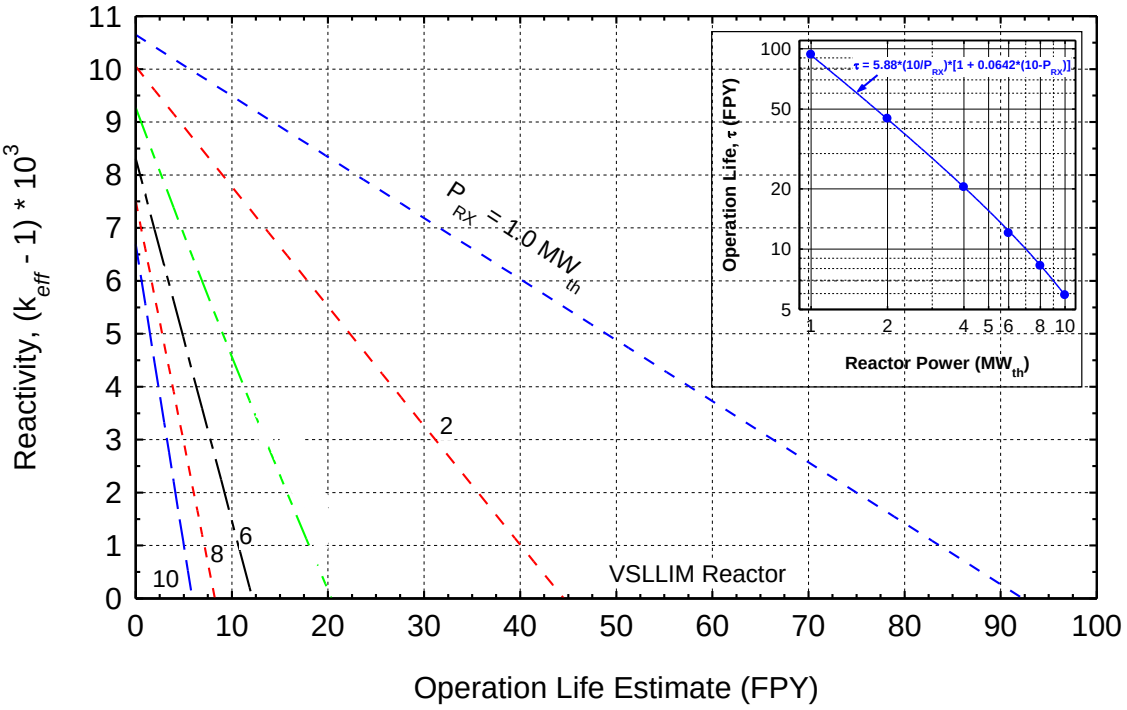

Fig. 4.8. Operation life estimates of the VSLLIM reactor at different powers (1.0 -10 MW_{th}).

Figure 4.8 presents estimates of the operation life of the VSLLIM reactor, for continuous operation without refueling, at a nominal power from 1.0 - 10 MW_{th}, and with a 2-m tall in-vessel chimney (Fig. 3.7). At 10 MW_{th}, the operation life estimate is ~5.88 full power year (FPY). The insert in Fig 4.8 shows that the operation lifetime, τ, increases rapidly with decreasing the reactor thermal power, P_{Rx}, in MW_{th}; and it is ~92.8 FPY at 1.0 MW_{th}. Considering the reactor thermal power, P_{RX}, in MW_{th} and the BOL hot-clean excess reactivity, the operation life estimates for the VSLLIM reactor, τ, in FPY are correlated as (Fig. 4.8):

$$\tau = (58.8/P_{Rx})\{1 + 6.42x\,10^{-2}\,(10 - P_{Rx})\}. \qquad (4.1)$$

This correlation and the results delineated in Fig. 4.8 indicate that the operation life of the VSLLIM reactor when operating at a nominal power of 2 and 6 MW_{th} is ~ 45 and ~ 12 FPY, respectively.

The depletion of the excess reactivity decreases, but the total energy generated through the end of life increases, with decreased nominal power of the VSLLIM reactor. At nominal powers of 10 and 1.0 MW_{th}, the reactivity (k_{eff} - 1) depletion rate is ~ 0.0011/FPY and ~ 0.0001/FPY, respectively. At these nominal reactor thermal powers, the total fission energy generated through EOL is ~93 and ~58.8 MWY, respectively. While the depletion rate of reactivity in the VSLLIM reactor core at 1.0 MW_{th} is an order of magnitude smaller than at 10 MW_{th}, the total energy generated through the EOL is ~58% higher. When operating at 1.0 MW_{th}, the core temperatures are lower than when operating at 10 MW_{th}, resulting in the BOL excess reactivity in the VSLLIM reactor being ~57% higher than at 10 MW_{th} (Fig. 4.8).

4.7. Fissile Inventory

The fissile' total inventory in the VSLLIM core changes with the reactor operation time due to the fission of the ^{235}U isotope in the UN fuel, and the accumulation of the fissile Pu isotopes, produced by neutron capture in ^{238}U in the fuel (Fig. 4.9). At BOL, the ^{235}U fission is the major contributor to the power generation in the core, followed by the fast neutron fission in the ^{238}U isotope in the UN fuel. A small amount of power is generated by the fission of other uranium isotope of ^{234}U and ^{236}U (Table 4.2). The depletion rate of ^{235}U in the core by fission decreases, while the accumulation of the fissile Pu isotopes (^{239}Pu, ^{240}Pu, ^{241}Pu, and ^{242}Pu) in the core progressively increases with operation time (Fig. 4.9).

At a nominal reactor power of 10 MW_{th}, the contribution of ^{235}U fission to the total power generation at BOL is 86.34%, decreasing to 84.19% at the EOL (after 5.88 FPY). The corresponding contributions of the ^{238}U fission are 13.49% and 13.51% of the total reactor power, respectively. The contribution of the fissile Pu isotopes to power generation in the VSLLIM reactor core is zero at BOL, but increases with operation time to reach 2.1% at the EOL (Fig. 4.9, Table 4.2). It worth noting that the fission cross-section and the numbers of neutrons produced per fast neutrons fission of the accumulating Pu isotopes in the core are higher than by the fission of either ^{235}U or ^{238}U.

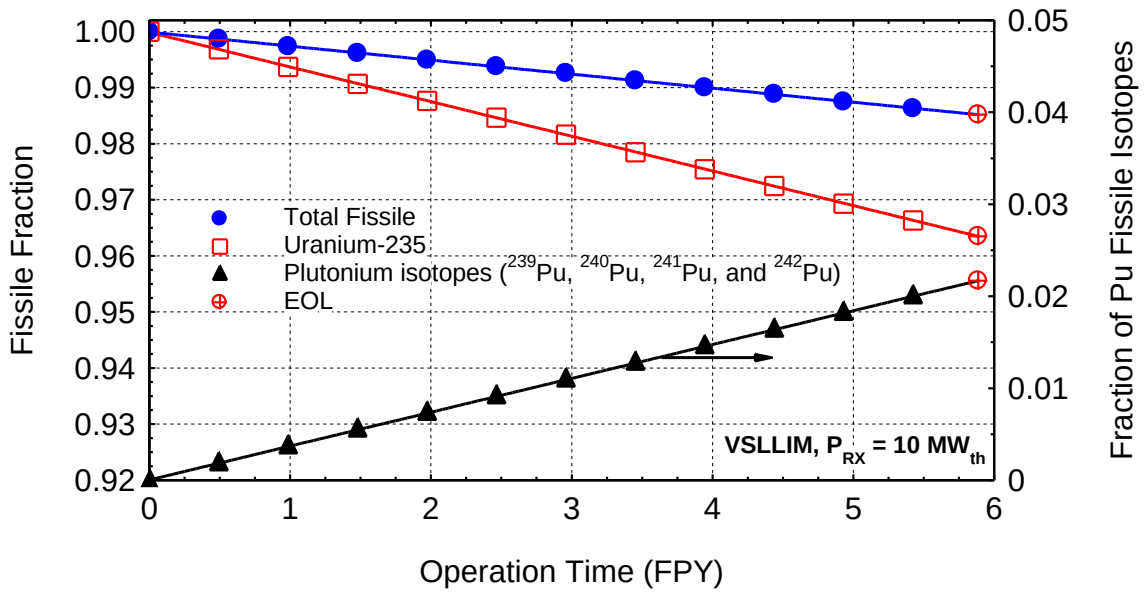

Fig. 4.9. Estimates of fissile inventory in VSLLIM reactor core with operation time at 10 MW_{th}.

Results indicate that at EOL, the percentage of the thermal power generated in the VSLLIM core due to fissions of the fissile Pu isotopes is ~3.1% and 2.1%, at a nominal reactor power of 1.0 and 10 MW_{th}, respectively. The results in Fig. 4.9 show that the inventory of ^{235}U decreases, while that of the fissile Pu isotopes increases with operation life of the reactor operating at 10 MW_{th}. The net effect is that the total fissile inventory in the VSLLIM core with operation time of the reactor decreases much slower than that of the fissile ^{235}U (Fig. 4.9).

For the same reactor thermal power the accumulation of the Pu fissile isotopes in the core decrease the depletion of ^{235}U in the UN fuel, partially contributing to the long operation life of the VSLLIM reactor. At EOL, ~96.3% of the original amount of ^{235}U remains in the UN fuel. When accounting for the buildup of the Pu fissile isotope, the total fissile in the reactor core at EOL is 98.5% of that of ^{235}U in the UN fuel at BOL (Fig. 4.9). This large fissile inventory in the VSLLIM reactor at EOL could be used to fuel thermal spectrum reactors, such as very high temperature gas cooled and heavy water moderated and light water cooled reactors (El-Genk and Shriener, 2018).

Table 4.2 compares the design features and performance parameters of the SLIMM and VSLLIM reactor concepts. Both designs are scalable, offer similar passive operation

and redundant safety features, could provide both electricity and process heat, and would be fabricated, assembled and sealed in the factory. While both SLIMM and VSLLIM reactors could be installed and operated at a permanent site, the VSLLIM reactor together with the energy conversion subsystem could also be deployed on a portable or a floating platform.

4.8. Summary

Performed neutronics analyses and reactivity depletion calculation for **V**ery-**S**mall, **L**ong-**LI**fe, and **M**odular (VSLLIM) reactor, this work investigates the effects of several design choices on the hot-clean reactivity, for achieving long operation life without on-site refueling with modest UN fuel enrichment, and the cold-clean shutdown margins of the RSS and RC. The investigated design choices include (a) changing the UN fuel enrichment below 18%, (b) replacing the axial material (BeO, HT-9, Na or DUN), (c) replacing the core wedges material (HT-9 or BeO), (d) replacing the BeO shrouds walls of the UN fuel assemblies in the driver core with HT-9, (e) estimate the temperature reactivity feedback, and (f) estimate the full-power operation lives of the reactor at different thermal powers (1.0 - 10 MW_{th}).

Results demonstrated that the choices for the VSLLIM reactor base design are most favorable for achieving the highest hot-clean reactivity and hence, the longest full-power operation lives, while maintaining sufficient cold- clean reactivity shutdown margin. Based on the parametric analyses on the UN fuel enrichment, 13.76% is considered the best choice for ensuring high enough hot-clean excess reactivity for a long operation life and sufficient cold-clean reactivity shutdown margin. Best results are with BeO axial reflectors, shrouds walls, ands core wedges.

In addition to having two independent systems for safety (RC and ESS), the negative temperature reactivity feedback is capable of shutting down the reactor with modest increases in the temperatures of the core UN fuel and the in-vessel liquid sodium. The estimated operation life of the SLIMM reactor base design is ~92 and ~5.8 full power years when operating at a thermal power of 1.0 and 10 MW_{th} respectively.

The results also show that the neutron energy spectrum is the VSLLIM reactor core is hard, for reducing the inventory of minor actinides in UN fuel during reactor operation. The UN fuel in the VSLLIM core experiences practically no swelling and fission gas

release, because of its low operating temperatures, $\leq$ 812 K at 10 MW_{th} and average power density up to 23.47 MW_{th}/m^3.

Table 4.2. Comparison of the design and operation and safety parameters of the SLIMM (El-Genk et al. 2017) and the present VSLLIM modular reactors.

Item / Feature	Salient Design, Operation, and Safety Features	
	SLIMM	**VSLLIM**
Design / Modularity		
- Scalable power range (MW_{th})	10 – 100	1.0 – 10
- Operation life (FPY)	66 – 6.35	92 – 5.8
- In-vessel chimney height (m)	2 – 8	1 – 2
- Coolant type	Liquid sodium (Na)	Liquid sodium (Na)
- Cooling during nominal operation and after shutdown	Natural circulation (NC) of in-vessel liquid Na	Natural circulation of in-vessel liquid Na
- Auxiliary power generation	Yes, LMHPs-TE Modules	Yes, LMHPs-TE Modules
- Operating pressure	Slightly below atmospheric	Slightly below atmospheric
- Fabricated/assemblies/sealed	In factory	In factory
Deployment		
- At a permanent site	-Yes, below ground and on seismic insolation bearings	-Yes, below ground and on seismic insolation bearings
- On a portable platform	No	Yes
- Transportation	Rail, Truck, Barge	Rail, Truck, Barge
Operation		
- Connected to distributed grid	Yes	Yes
- Connected to central grid	Yes	Yes
- Stand alone	Yes	Yes
- Electricity generation	Yes	Yes
- Process heat	Yes	Yes
Control and Passive Safety		
- Redundant options of passive decay heat removal	In-vessel Na-Na HEX, LMHPs, and NC of ambient air	In-vessel Na-Na HEX, LMHPs, NC of ambient air
- Control rods	Enriched B_4C	Enriched / natural B_4C
- Nominal reactor control	Yes	Yes
- Emergency shutdown	Yes	Yes
- On-site fuel storage	No	No
- EOL handling and replacement	2-6 mon. after shutdown	$\geq$ 6 mon. after shutdown
Reactor Core Design		
- Fuel material (enrichment)	UN (15.35%)	UN (13.76%)
- Fuel loading in core	37 rod hexagonal bundles	19 rod hexagonal bundles
- Fuel bundles wall	Scalloped BeO clad in HT-9 SS	Scalloped BeO clad in HT-9 SS
- BeO axial reflector	Yes	Yes
- DUN radial blanket	Yes	NA
- H_c/D_c (Normalized)	0.69 (1.0)	0.92 (1.33)
Operation Parameters @ 10 MW_{th}		
- EOL fissile depletion (%)	8	1.5
- Fuel av. power density (MW_{th}/m^3)	19.0	23.5
- Max. UN fuel temperature (K)	814	812

.

5. DECAY HEAT REMOVAL BY NATURAL CIRCULATION OF AMBIENT AIR

The worked presented in this section investigates passive decay heat removal for the VSLIMM reactor by natural circulation of ambient air from the outer surface of the guard vessel. The approach is similar to that applied to the SLIMM reactor (El-Genk and Palomino 2015, Palomino and El-Genk 2016). Although the sizes of the vessels for the two reactors are different, the analyses use the same methodology used successfully for the SLIMM reactor. The objective is to parametrically investigate the potential of the passive removal of the decay heat generated in the core of the VSLLIM reactor after nominal shutdown, or following an unlikely malfunction of in-vessel HEX, by natural circulation of ambient air along the guard vessel wall. The performed 3-D thermal-hydraulics and Computational Fluid Dynamics (CFD) analyses also investigate the effects of using metal fins along the guard vessel wall and changing the width of the cold air intake duct on the decay heat removal rate and the time after shutdown for cooling in-vessel liquid sodium to 400 K.

5.1. Methodology

The performed 3D-CFD and thermal-hydraulics analyses quantify the passive decay heat removal by natural convention of ambient air from the outer surface of guard vessel wall after shutdown of the VSLLIM reactor (El-Genk and Palomino 2018). The analyses employ the commercial code package STAR-CCM+, version 12.02.010 (CD-ADAPCO, 2017). After reactor shutdown, following an unlikely malfunction of the Na-Na HEX (Figs. 3.4, 3.8), natural circulation of the in-vessel liquid sodium is maintained, removing the decay power generated in the core by radioactive decay of fission products in the UN fuel rods. The primary vessel wall serves as a heat sink for maintaining natural circulation of the in-vessel liquid sodium after reactor shutdown, the removed thermal power is transported by the in-vessel liquid sodium to the downcomer (Figs. 3.4, 3.8), where it is removed by convection to the inner surface of the primary vessel, then by conduction in the primary vessel wall and the sodium gap to the guard vessel wall cooled by natural circulation of ambient air at its outer surface. The present analyses do not take credit for the simultaneous removal of the decay power from the primary vessel wall by

the LMHPs embedded in the upper part of the vessel wall. Therefore, the present estimates of the decay heat removal by natural circulation of ambient air would be as much as 50% of the total rate possible, when including the LMPHs.

The decay heat conducted through the walls of the reactor primary and guard vessels, separated by Na gap, is removed by ambient air from the outer surface of the guard vessel wall. As the rate of decay heat generation in the core decreases with time after shutdown, so does the circulation rate and the average temperature of the in-vessel liquid sodium, in the downcomer.

Immediately after the VSLLIM reactor shutdown, the rate of decay heat generation rate in the core is higher than that removed from the outer surface of the guard vessel by natural circulation of ambient air, alone. The difference would be stored temporary in the in-vessel liquid sodium, raising its average temperature only slightly. This continues until the rate of decay heat generation drops below that of the heat removal by natural circulation of air, causing the average temperature of the in-vessel sodium to peak, then decrease thereafter with time after shutdown. The present analyses for nominal reactor power of 10 MW_{th} before shutdown estimates the time for the average temperature of the in-vessel liquid sodium to drop to as low as 400 K, after the VSLLIM reactor shutdown (Figs. 3.4, 3.8, 5.1).

In the performed CFD and thermal-hydraulics analyses, the temperatures of the circulating liquid sodium in the downcomer of the VSLLIM reactor immediately after shutdown are the same as during nominal operation at 10 MW_{th} (core inlet and exit temperatures of 610 K and 754 K, respectively). The Na temperature in the downcomer is assumed to change linearly with distance from the free surface of liquid sodium in the upper plenum (Fig. 5.1c). The calculated average temperature of the liquid sodium circulating in the down comer, as function of the reactor thermal power after shutdown, are used in the present analyses. In these analyses, the heat transfer coefficient along the inner surface of primary vessel wall is practically constant because of the low Peclet number of the circulating liquid sodium in the downcomer (Schriener and El-Genk, 2015).

5.2. Numerical Meshing

The full computational domain for the CFD and thermal-hydraulics analyses of the decay heat removal by natural circulation of ambient air from the outer surface of the VSLLIM reactor's guard vessel wall is very large, requiring long computational time and large computation resources (Fig. 5.4). Instead, the analyses use a 6^o pie section with symmetry boundary conditions (Figs 5.1a, b). This approach effectively decreased the number grid mesh elements and the computational time for convergence without affecting the results. As shown in Fig. 5.1, the total heated length along the reactor primary vessel wall, H_o, for 10 MW_{th} VSLLIM with 2-m tall in-vessel chimney, is 4.91 m.

The performed analyses solve the steady-state conservation equations of mass, momentum and energy for natural circulation of ambient air in the cold intake duct and the hot riser (Fig. 5.1). They calculate the total heat removal rate from outer surface of the guard vessel wall by air and quantify the contributions of thermal radiation to the steel liner along the opposite wall in the hot air riser, and of natural convection to the air in the hot riser. The CFD analyses use the SST k-ω turbulence model to simulate the ambient air flow in the cold intake duct and in the hot riser (Fig. 5.1). Wilcox (Wilcox, 1998) had introduced the original formulation of the k-ω model, for improving the treatment in the boundary layers, with adverse pressure gradients and separating flows. Menter (Menter 1994) formulated the SST k-ω model, by blending a k-ε behavior-like model in the free-stream of the bulk flow with a k-ω model in the boundary layer near the wall. The SST k-ω model overcomes the solution sensitivity to free-stream conditions of the classical k-ω model. The present analyses of the ambient air flow and convection heat transfer use a turbulent Prandtl number, $Pr_t \sim 0.8$ and both the second order upwind convection option and the Durbin Scale limiter realizability scheme for the SST k-ω model.

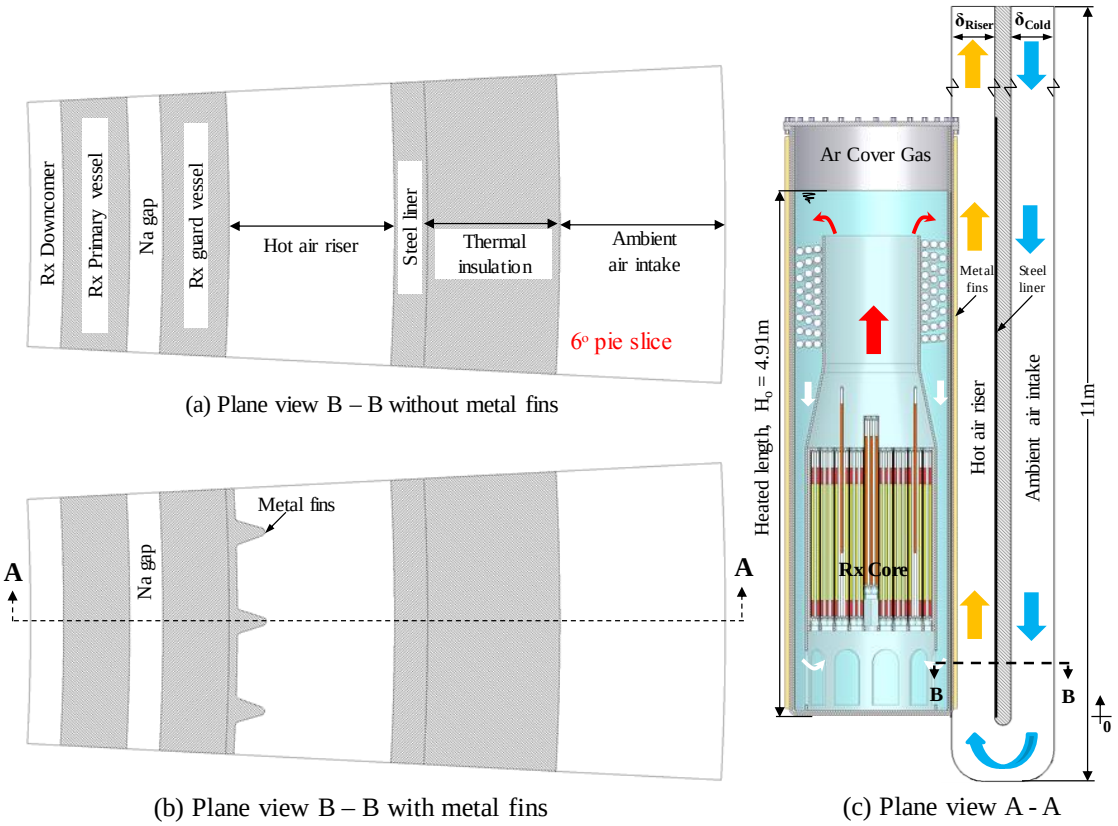

(a) Plane view B – B without metal fins

(b) Plane view B – B with metal fins

(c) Plane view A - A

Fig. 5.1. Cross-section views and an illustration of the decay heat removal by natural circulation of ambient air from the guard vessel outer surface, without and with metal fins.

In addition to the total flow rate and both the lateral velocity and temperature distributions with axial distance in the hot air riser (Fig. 5.1c), the present analyses calculates the fractions of the heat removal rate from the guard vessel wall by thermal radiation to the steel liner that is located at the opposite side on the concrete wall and by natural convection. This is for the cases with and without metal fins, along the surface of the reactor guard vessel (Figs. 5.1a and 5.1c). In order to account for the heat dissipated by thermal radiation, the analyses use the gray thermal radiation surface-to-surface model in the STAR-CCM+ code package, version 12.02.010 (CD-ADAPCO., 2017), and assume an effective surface emissivity of 0.8. Such surface emissivity is achievable by applying a back coating onto the surface of the guard and the metal fins (Ackatar Advanced Coatings, 2019; He et al., 2009). The analyses of natural circulation of ambient air couple the convection and radiation heat transfer from the surface of the guard vessel

or the metal fins to the convection heat transfer from the circulating sodium in the downcomer of VSLLIM reactor to the primary vessel wall, and by conduction in the primary vessel wall, them sodium gap and the guard vessel wall (Fig 5.1a and 5.1b).

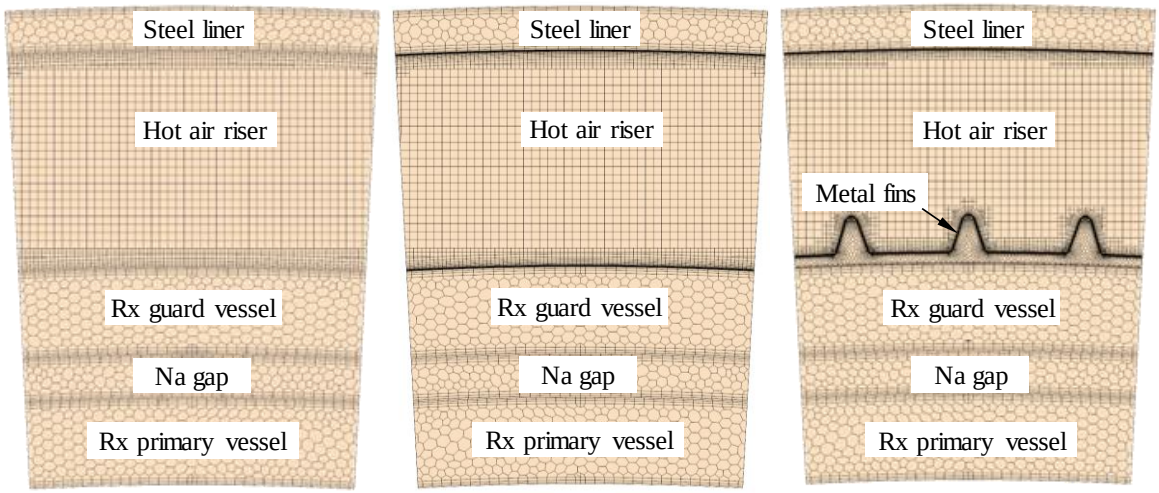

(a) Coarse mesh grid without metal fins

(b) Finer mesh grid without metal fins

(c) Finer mesh grid with metal fins

Fig. 5.2. Numerical mesh grid elements in present analyses of decay heat removal by natural circulation of ambient air from the VSLLIM's guard vessel wall, with and without metal fins.

The CFD-thermal-hydraulics of the VSLLIM reactor's passive decay heat removal by natural circulation of ambient air use a finer mesh (Fig. 5.2), developed using the polyhedral mesher, trimmer, the surface re-mesher, and the prims layer mesher models in the STAR-CCM+ code (CD-ADAPCO, 2017). The mesh grid elements in the solid regions are polyhedral with an average volume of 134 mm^3 (Figs. 5.2a and 5.2b). In addition, there is a 1.5 mm-thick region of 3 prismatic layers of equal thickness which are parallel to the surface to better capture the temperature gradients at the interfaces. The hexahedral mesh grid elements in the ducts of the cold air intake and the hot air riser are generated by the trimmer mesher (Figs. 5.2a and 5.2b). The mesh elements in the bulk flow of the cold air intake duct have an average volume of 250 mm^3. In the bulk of the hot air flow, the mesh grid elements are 16 mm^3 in average volume (Fig. 5.1). In the hot air riser, smaller size elements (~1 mm^3) are used next to the steel liner and the guard vessel surface, with and without metal fins, to capture the temperature gradients in the

boundary layers at theses surfaces. In order to capture the boundary layer effect, prismatic layers are added in the air boundary layer along the solid surfaces of the guard vessel, with and without metal fins, and of the steel liner on the opposite side of the hot air riser duct (Figs. 5.1 and 5.2). The thickness of these layers increases with distance from the solid surfaces with a multiplier of 1.3 (Figs. 4). Table 5.1 lists the number of numerical mesh elements used in different regions of the computation domain for the VSLLIM decay heat removal by natural circulation of ambient air (Figs. 5.2a, b, c).

Table 5.1. Numerical elements in the CFD analyses of decay heat removal from the outer surface of the VSLLIM guard vessel wall surface, with and without metal fins.

Computation Region		**Total mesh elements**		
		Without metal fins		**With metal fins**
		(a) Coarse Mesh	**(b) Finer Mesh**	**(c) Finer Mesh**
Ambient air	Intake duct	0.73 M	0.73 M	0.74 M
	Hot air riser	13.29 M	23.7 M	73.02 M
Rx primary vessel wall		0.50 M	0.50 M	0.50 M
Liquid sodium gap		0.36 M	0.36 M	0.36 M
Rx guard vessel wall		0.50 M	0.50 M	0.50 M
Steel liner in hot riser		0.39 M	0.39 M	0.39 M
Metal fins in hot riser		N/A	N/A	2.16 M
TOTAL mesh elements		**15.77 M**	**26.19 M**	**77.68 M**

The refinement from the coarse to the finer mesh grid in the computation domain involved increasing the number of prismatic layers in the 3-mm thick boundary layers along the surfaces of the guard vessel wall and the steel liner in the hot riser. The number of the prism layers is 5 and 15 in the coarse and finer mesh grid, respectively, with a thickness growth multiplier of 1.3. This approach generates 0.33-mm and 0.018-mm thick elements next to the solid surfaces in the air riser duct, in the coarse and finer mesh grid, respectively. Without metal fins along the surface ofthe guard vessel wall, the coarse mesh grid has ~1.75 million elements in the solid and ~14 million elements in the fluid, for a total of 15.77 million elements (Table 5.1, Fig. 5.2a). This is compared to ~1.75 million elements in the solids and ~24.44 million elements in the fluid for a total of 26.19 million elements in the finer mesh (Table 5.1, Fig. 5.2b). These elements represent a 66% increase in the total number of mesh elements, which increases the computational

time for converges by approximately the same amount. With metal fins along the vessel wall, the numerical mesh grid also accounts for the boundary layers, at and in between the metal fins, increasing the total number of mesh elements of the finer grid from 26.19 to 77.68 million elements, ~95% is in the hot air riser duct, ~1% in the cold air intake duct, and 5% in the solids (Table 5.1, Fig. 5.2c).

In the present CFD analyses, the value of the y+ parameter, a dimensionless ratio of the turbulent-to-laminar influence in the mesh grid elements near the solid surfaces, helps assess the quality of the mesh grid refinement (Salim and Cheah, 2009; Roache, 1994). For natural circulation of ambient air (Palomino and EL-Genk., 2016), $y+ < 1$ for the cases without and with metal fins along the outer surface of the guard vessel, suggesting that the mesh refinement near the solid boundary in the present CFD analyses is acceptable. In addition, a sensitivity analyses is carried out to quantify the effects of the mesh refinement on the calculated results. These include the total mass flow rate of the ambient air in the hot riser, the rate of heat removal from the outer surface of the guard vessel wall, the temperature of the air exiting the hot riser, and the maximum temperatures in the solid structure. Table 5.2 lists the calculated values of the Grid Convergence Index (GCI) in the hot air riser and solid structure. The values of the GCI are estimated by performing separate calculations with two mesh grid refinements listed in Table 5.1.

The GCI represents the discretization error due to the mesh grid and time refinement (Roache 1994). The GCI is the relative difference in the values on the calculated parameters in the hot air riser with the coarse and the finer mesh grids. Results in Table 5.2 show that the GCI for the solid structure is < 0.1%, suggesting that the mesh refinement in the solids is likely converged. The GCI for the mass flow rate and the air bulk exit temperature in the hot riser is ~ 0.7% and1.5%, respectively. However, the GCI for total rate of heat removal from the outer surface of the guard vessel and steel liner by natural convection of ambient air is 4.7%, despite a 66% increase in the total mesh elements, compared to the coarse grid (Table 5.1). This suggests that further refinement of the mesh grid may not considerably decrease the GCI of the total rate of heat removal in the hot riser, but would increase the computational time for convergence. Therefore,

the CFD results presented in the reminder of this paper are obtained using the finer mesh grid (Fig. 5.2b and 5.2c).

Table 5.2. Mesh refinement sensitivity analysis results and GCI estimates.

Grid Convergence Index (GCI)		
Computation Region	**(a) Coarse Mesh**	**(b) Finer Mesh**
Ambient air		
• Mass flow rate (kg/s)	0.910 (1.00)	0.916 (1.007)
• Hot air riser exit temperature (K)	461 (1.00)	468 (1.015)
• Total heat removed (kW_{th})	148 (1.00)	155 (1.047)
Structural maximum temperature (K)		
• Rx primary vessel	743 (1.00)	742 (0.999)
• Liquid sodium gap	736 (1.00)	735 (0.999)
• Rx guard vessel	735 (1.00)	734 (0.999)
• Steel liner in hot riser	673 (1.00)	670 (0.999)

5.3. Results and Discussion

The presented results are of the 3-D, thermal hydraulics and CFD analyses of the decay heat removal by natural convection of ambient air from the outer surface of the VSLLIM reactor guard vessel, after shutdown, nominally and in case of a malfunction of the in-vessel Na-Na HEX. The results are for the reactor with 2-m tall chimney and nominal thermal power of 10 MW_{th} before shutdown (Figs. 3.4a and 3.8). The analyses investigated the effects of using metal fins along the guard vessel wall, and reducing the width of the cold air intake duct on the rate of heat removal by natural circulation of ambient air. This rate is compared to that of the decay heat generation in the reactor core, with time after shutdown. The calculated relative contributions of natural convection and thermal radiation to the total rate of heat removal from the outer surface of the guard vessel wall by ambient air are also compared. The 3-D, CFD and thermal-hydraulics analyses account for the changes in the thermal conductivities of the various solid structures and in the thermophysical properties of the in-vessel liquid sodium and ambient air with temperature.

5.4. Axial Temperature Distribution

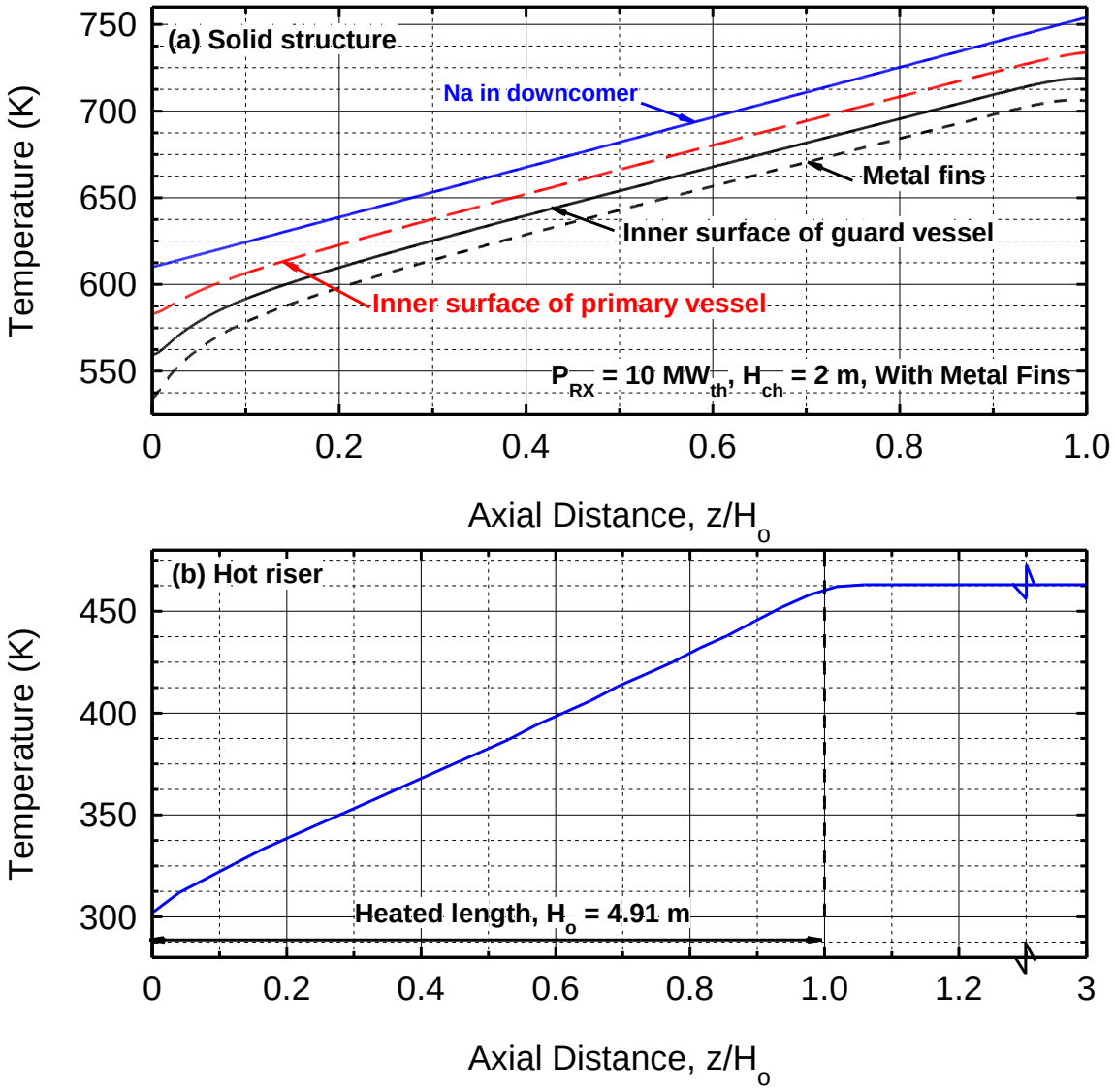

Fig. 5.3. Calculated axial temperature distributions for the removal of decay heat by natural circulation of ambient air, after VSLLIM reactor shutdown.

Figures 5.3a,b presents the calculated axial temperature distributions in the solid structure and the hot air riser (Figs. 5.1). The decay heat from the in-vessel liquid sodium circulating by natural convection in the downcomer is removed by convection to the inner surface of the reactor primary vessel. It is then conducted through the primary vessel wall, the small sodium gap, and the guard vessel wall (Fig. 5.1). The dissipated heat in then removed from the outer surface of the guard vessel wall, without or with metal fins, by natural circulation of ambient air in the hot riser. The heat is removed by

radiation to the steel liner on the opposite wall of the hot air riser, and by convection from the surfaces of the guard vessel and the steel liner (Figs. 5.2, 5.3).

Figure 5.3 compares the calculated axial temperature distributions in the downcomer of the VSLLIM reactor, along the inner surfaces of the primary and guard vessels walls, at the surface of the metal fins along the guard vessel outer surface, and of the air bulk temperature in the hot riser. These temperatures, calculated immediately after reactor shutdown, are plotted versus the axial distance, z, from the entrance of the hot air riser (z = 0), normalized to the heated length along of the primary vessel wall, H_o (Fig. 5.1).

Immediately after reactor shutdown, the in-vessel liquid sodium enters the downcomer ($z/H_o = 1.0$) at 754 K and exits the downcomer to the lower plenum ($z/H_o = 0.0$) at 610 K (El-Genk and Palomino, 2018). Although these temperatures change with time after reactor shutdown, they help quantify the potential of passively removing the decay heat generated in the VSLLIM reactor core after shutdown. That is by natural circulation of ambient air along the surface of the guard vessel wall (Fig. 5.2), in an unlikely malfunction of the in-vessel Na-Na HEX (Figs. 3.8, 5.1).

Results in figure 5.3, show that the average temperature drop between the liquid sodium in the downcomer and the inner surface of the primary vessel wall is constant ~ 17 K. The calculated average temperature drop from the inner surface of the primary vessel to the inner surface of the guard vessel is ~13.3 K, and is 23.7 K at $z/H_o = 0.0$. Similarly, the temperature drop across the guard vessel wall and the metal fins (Fig. 5.3a) averages ~12 K along the heated length; but as much as ~25.6 K at the bottom of the heated length ($z/H_o = 0.0$). The calculated temperature drops across the small Na gap between the primary and guard vessels, and the metal fins are 1.8 K and 0.63 K, respectively. The larger temperature drops at the bottom of the heated length are because of the low temperature and flow mixing of the ambient air at that location (Figs. 5.2, 5.3). The cold air flowing down the intake duct reverses direction at the bottom of the heated length and enters the hot air riser. It creates a flow vortices and mixing at that location ($z/H_o = 0.0$). Figure 5.3b shows that the air bulk temperature in the hot riser increases linearly with distance up the riser duct. It enters the hot air riser at 301 K (assumed ambient temperature) to exits at ~463K.

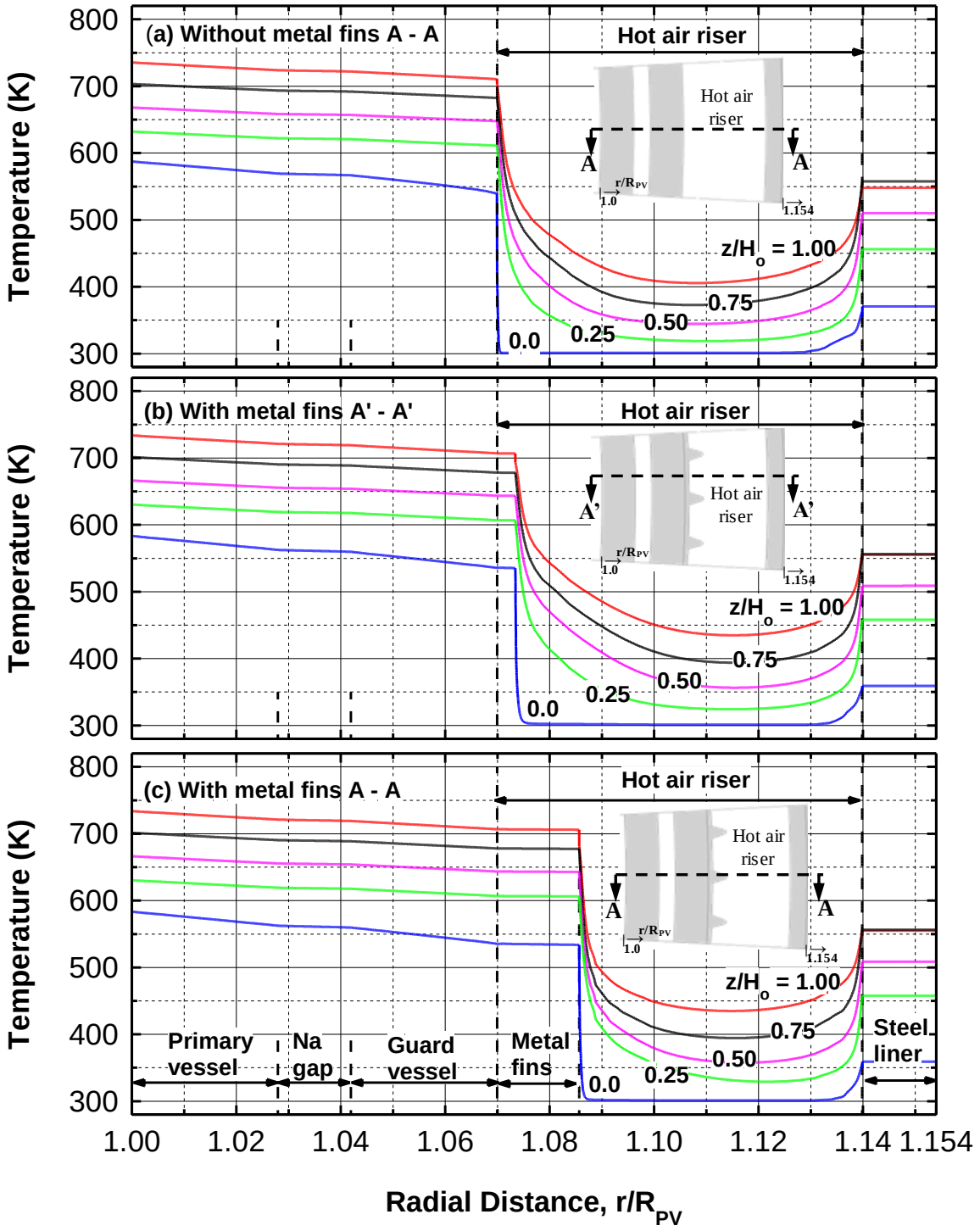

Fig. 5.4. Calculated radial temperature profiles at different elevations in the solid structure and the hot air riser.

5.5. Radial Temperature Distribution

Figures 5.4 and 5.5 present the calculated radial temperature profiles in the walls of the reactor's primary and guard vessel walls, without and with metal fins, and the hot air riser at five axial elevations (z/H_o = 0.0, 0.25, 0.5, 0.75 and 1.0). These results show the effects of thermal radiation from the surface of the guard vessel to the steel liner at the opposite wall in the hot air riser, on natural convection of air at their surfaces (Figs.5.4, 5.2). The dividing wall, between the duct for ambient air intake and the hot air riser, is thermally insulated along its surface in the cold air duct. The radial temperature in the steel liner is uniform and lower than at the surface of the guard vessel, or the metal fins, but much higher than the air bulk temperature in the hot riser (Fig 5.2 and 5.3).

The calculated radial temperature distributions (Fig. 5.4), extend from the inner surface of the reactor primary vessel wall (r/ R_{PV} = 1 where, R_{PV} in the inner radius of the reactor primary vessel) to the surface of steel liner (r/R_{PV} = 1.154), the radial temperature profiles at different axial location, without metal fins, and the temperatures in the solid regions increase with axial elevation up to the end of the heated length (z/H_o =1). Such increases are commensurate with temperature of the liquid sodium flow in the downcomer of the VSLLIM primary vessel. From the inner surface of the reactor primary vessel (r/R_{PV} = 1) to the outer surface of the guard vessel (r/R_{PV} = 1.07), the temperature decreases almost linearly with increasing r/R_{PV}. The average temperature drop in the solid structure is ~21 K, and very small in the Na gap, due to the high thermal conductivity of Na. At z/H_o = 0, the radial temperature drop in the solid structure increases to ~47 K. The temperature of the steel liner increases with elevation because the heat transport by thermal radiation from the facing surface of the guard vessel is directly proportional to the surface temperature, which also increases with axial distance (or z/H_o). It increases from 370 K at z/to 557 K at z/

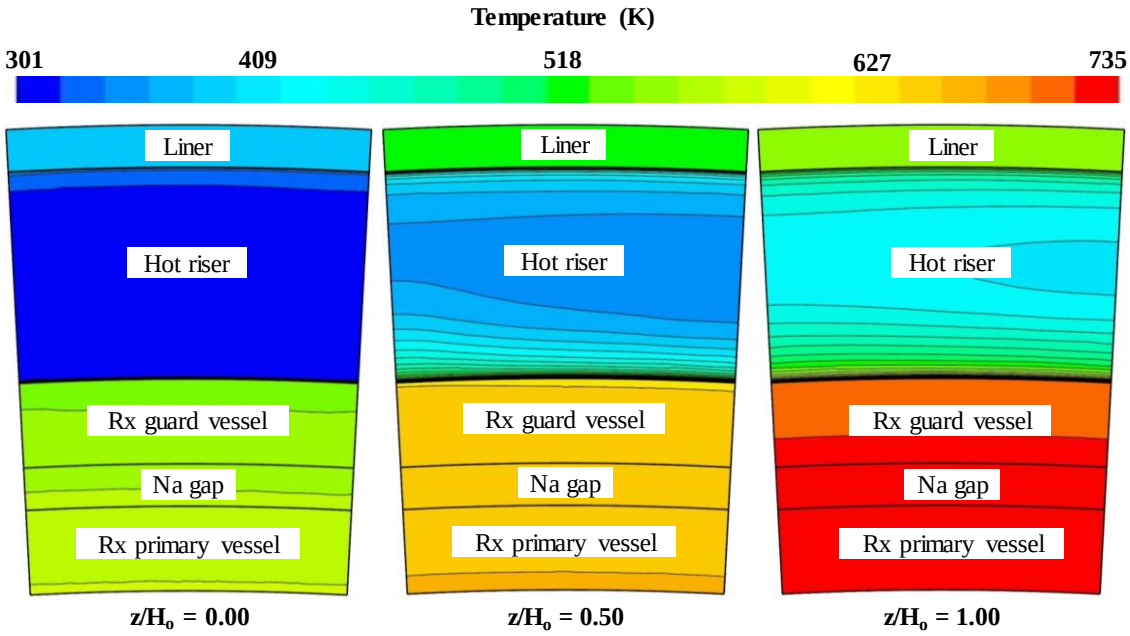

(a) Without metal fins

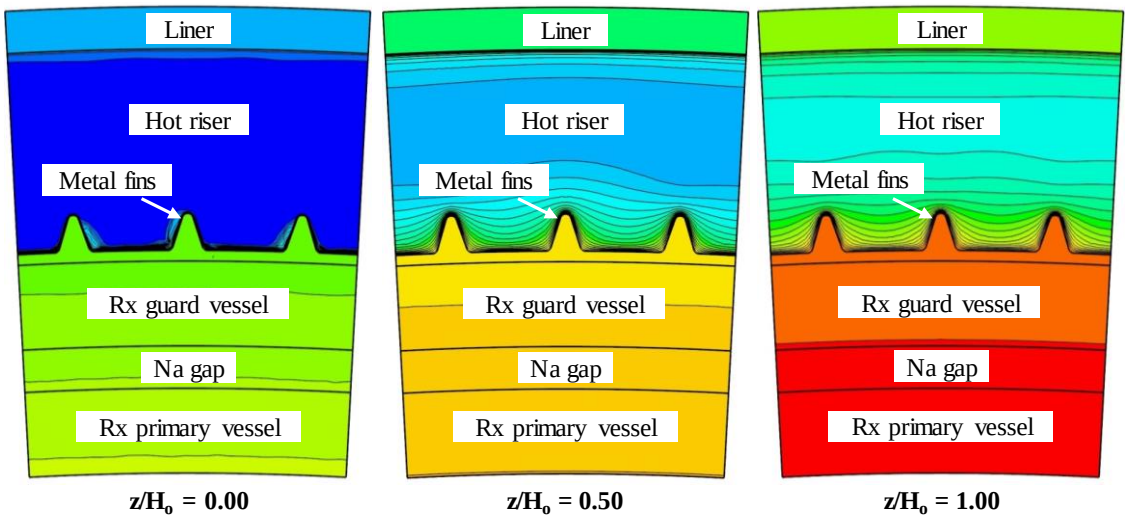

(b) With metal fins

Fig. 5.5. Calculated radial temperature contours at different elevations in the walls of the reactor primary and guard vessels and hot air riser.

Figure 5.4a also shows that the highest temperatures in the hot air riser are those next to the surfaces of the guard vessel and the steel liner. There are steep temperature drops in the boundary layers at these two surfaces. The temperature drops from the outer surfaces of the guard vessel wall and the steel liner to that of the bulk air flow in the hot riser decrease with axial location. Figures 5.4b, c compare the calculated radial

temperature distributions for the guard vessel with metal fins at two angular locations (θ = 0, A - A and $\theta = 1^o$, A'- A') and at five axial locations (z/H_o = 0.0, 0.25, 0.5, 0.75 and 1.0). The radial temperature from the inner surface of the primary vessel wall ($r/ R_{PV} = 1$) to the steel liner surface ($r/R_{PV} = 1.154$), decreases linearly with r/R_{PV}. The temperature drop across the metal (Cu) fins is very small ~ 0.6 K because of the high thermal conductivity of Cu. The average temperature drop from the fins outer surface to the air bulk flow is ~280 K, which is about 8% lower than for the guard vessel without metal fins. The metal fins which affect the heat dissipation from the outer surface of the guard vessel by thermal radiation.

Figures 5.5a,b presents images of the calculated temperature contours in the reactor primary vessel wall, the guard vessel walls, without and with metal fins, and the hot air riser, at three axial elevations (z/H_o =0.0, 0.5 and 1.0). These images confirm the results in Figs. 5.4a, c. The surface temperature of the guard vessel wall, without and with metal fins, ranges from 534 K-711 K, depending on the axial elevation. The total heat dissipated by thermal radiation from the guard vessel to the steel liner, on the opposite wall of the annular hot air riser, is proportional to the surface temperature to the forth power.

The total radial temperature drop in the solid structurers represents only about ~8% of the total temperature drop to bulk temperature of the air flow in the hot riser, in which the temperature drop across the boundary layer is the highest. As the air moves up the hot riser, the thickness, and hence the temperature drop across thermal boundary layer, increases. This is because the dynamic viscosity of air increases with temperature. The thermal boundary layer doubles in size between the entrance ($z/H_o = 0$) and exit (z/H_o = 1.0) of the hot riser.

5.6. Radial Velocity Profile in Hot Air Riser

Cold air travels down to the bottom of the air intake duct, and then reverses direction to flow upward in the hot riser, driven by buoyant force. The air in the hot riser removes, by natural convection, the heat dissipated from surface of the guard vessel, with or without metal fins; and the steel liner on the opposite wall of the riser.

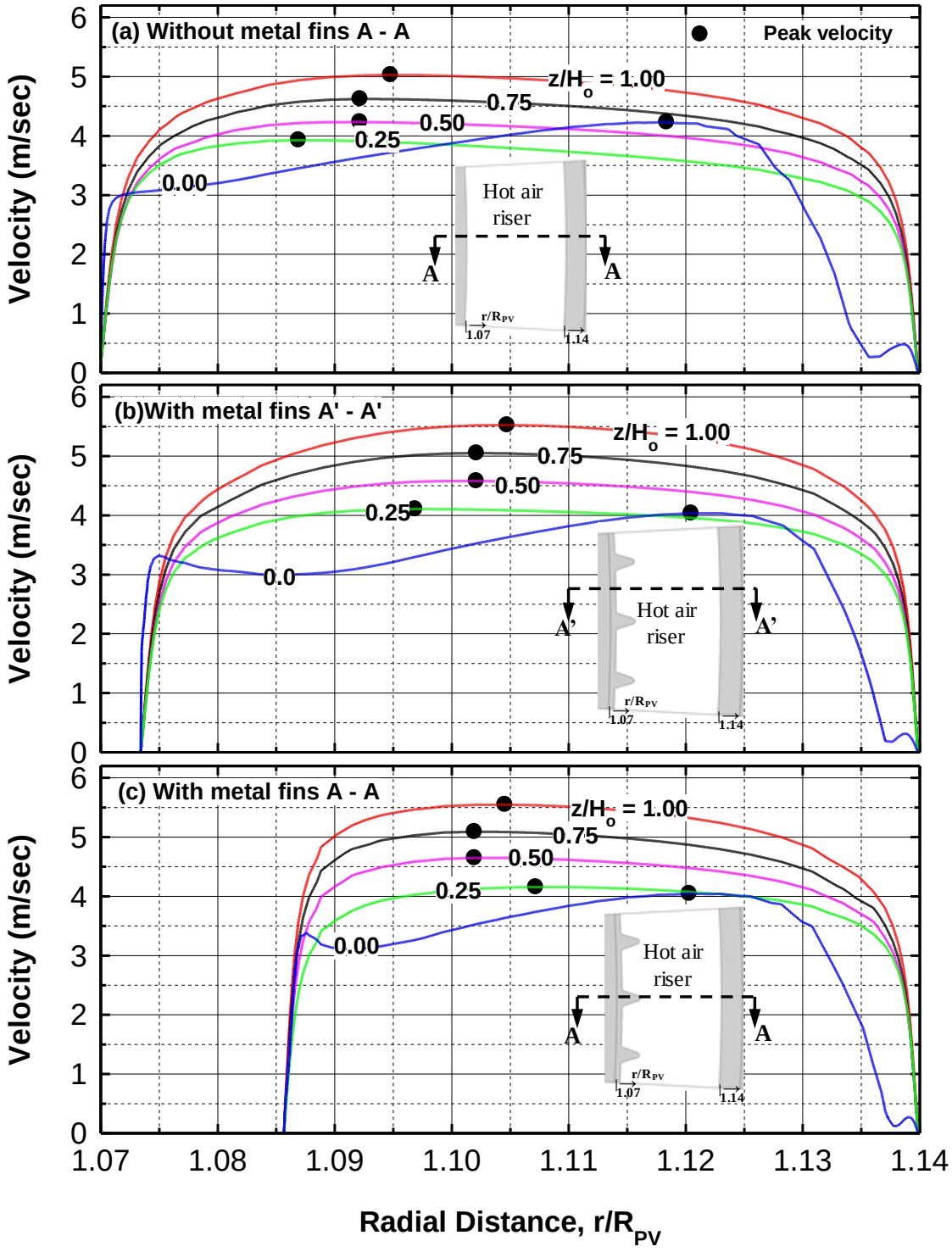

Fig. 5.6. Calculated radial velocity profiles of the ambient air flow at different elevations in the hot air riser, for the guard vessel wall without and with metal fins.

Figures 5.6a, c present the calculated radial velocity profiles in the hot riser at different axial location (z/H_o = 0.0, 0.25, 0.5, 0.75 and 1.0) along the dashed line in the

insert. With and without metal fins, the air velocities in the hot riser increase with axial elevation, and are highest at the exit of the riser ($z/H_o = 1.0$). This increase in velocity is due the increased buoyant driving force and the decreased in the density of the rising air with increased temperature, with distance from the entrance of the riser ($z/H_o = 0.0$). The almost uniform air velocity profiles across most of the cross section of the annular hot riser are indicative of turbulent flow of the rising hot air. However, the radial velocity profile of the air at the entrance of the hot riser ($z/H_o = 0$), has its maximum velocity shifted closer to the outer radius of the hot riser, nearer to the steel liner. Such distortion in the air velocity profile is caused by the asymmetric air flow mixing and the formation of vortices, particularly near the surface of the guard vessel wall (Figs. 5.7, 5.8).

Without metal fins along the surface of the guard vessel wall, the velocity profile near the entrance of the hot riser ($z/H_o = 0.25$) is slightly asymmetric with a maximum velocity of 3.93 m/sec close to the surface of the guard vessel ($r/R_{PV} = 1.087$). This is because of the annular geometry of the riser and that the surface temperature of the guard vessel wall is higher than that of the steel liner at the opposite surface. At the exit of the riser ($z/H_o = 1$), however, the maximum air velocity increases by ~28% and shifts outward to $r/R_{PV} = 1.095$ (Fig. 5.6a). Figures 5.6b, c compare the calculated radial velocity profile for guard vessel wall with metal fins along the dash lines in the inserts. As in Fig. 5.6a, the radial velocity profiles at different axial location, excluding at the entrance of the hot riser, where flow vortices and mixing occurs, are indicative of turbulent flow in the rising hot air. At $z/H_o = 0.25$, the maximum velocity is 4.03 m/sec occurs at $r/R_{PV} = 1.097$ (Fig. 5.6b), while in Fig. 5.6c it occurs at $r/R_{PV} = 1.107$. At the exit of the hot riser ($z/H_o = 1$), the maximum air velocity of 5.52 m/sec, occurs at the radial distance, $r/R_{PV} = 1.105$, which is about the middle of the annular hot riser.

The images in Figs. 5.7a,b, are of the velocity contours in the hot air riser at three different axial locations ($z/H_o = 0.0$, 0.50 and 1.0). In the absence of metal fins along the outer surface of the guard vessel (Fig. 5.7a), the calculated velocity contours indicate that the air bulk flow velocity is not uniform. At $z/H_o = 0$, the contours show the air mixing at the entrance of the hot riser, while at $z/H_o = 0.50$ and 1.0, the rising hot air is moving increasingly faster. The images in Fig. 5.7b show the velocity contour for air flow in the hot riser, at three different axial locations ($z/H_o = 0.0$, 0.50 and 1.0). Again, the velocity

contours at the entrance of the hot riser (z/H_o = 0.0) show the air mixing at that location due to the change in air flow direction from the cold air intake duct to the hot riser. The images in both Figs. 5.7a, b, clearly illustrate the increase in the boundary layer thickness near the solid surfaces of the guard vessel and the steel liner in the hot riser with increased elevation.

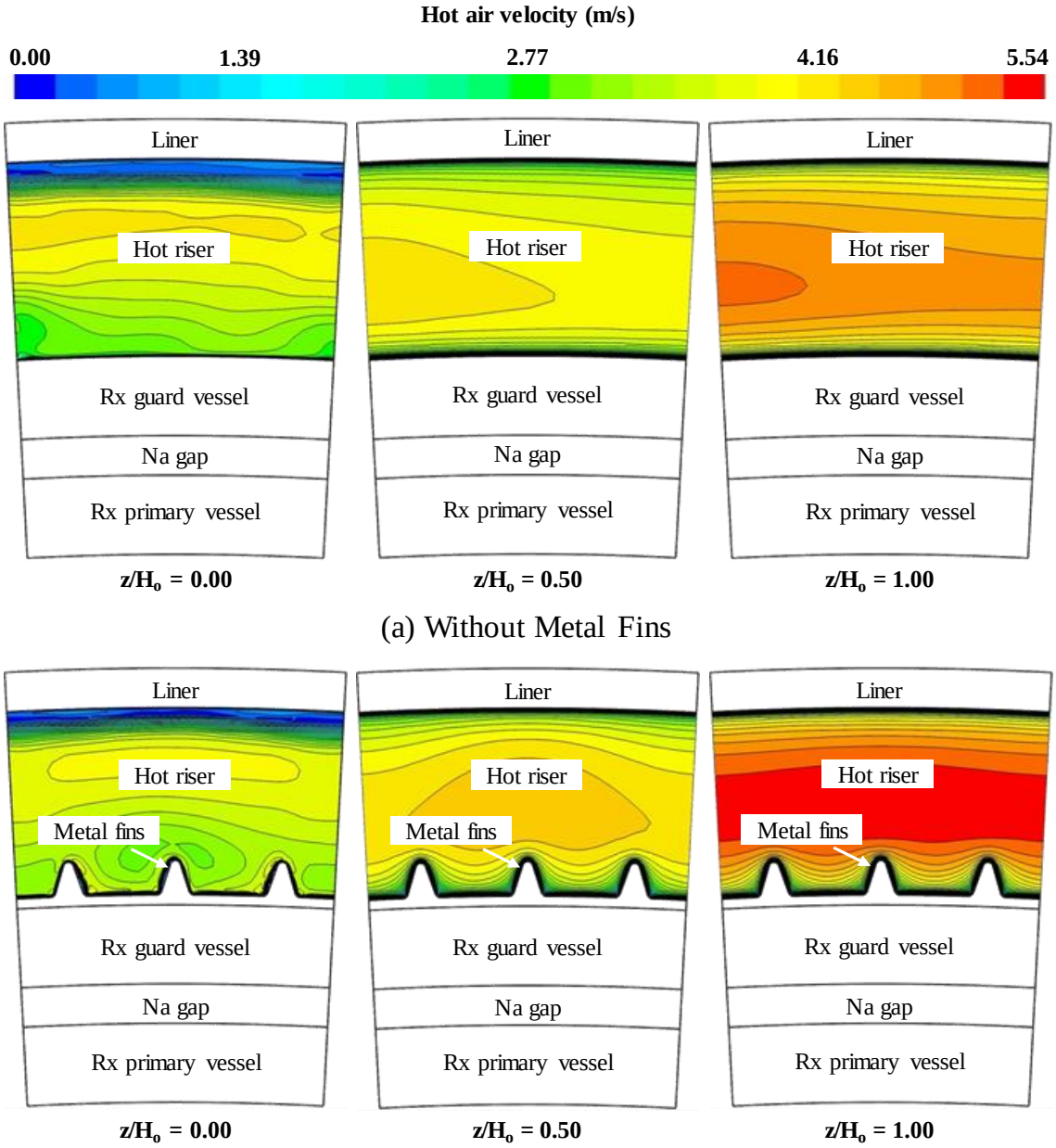

Fig. 5.7. Calculated velocity contours at different elevations in hot air riser.

Figures 5.8a,b present images of the velocity contours of the cold air entering the hot riser, for the cases without and with metal fins along the surface of the guard vessel wall. In both cases, the ambient air travelling down the annular cold intake duct becomes hydro-dynamically fully developed at point (1). At (2), the air flow is distorted somewhat as it begins to reverse direction and enters the hot riser. Between points (2) to (3), the air flow is distorted with more of the air flowing along the surface of the guard vessel, away from the steel liner on the opposite wall of the hot rise. This asymmetric flow develops vortices at the entrance of the hot riser. However, the rising air flow becomes gradually more developed with increase axial elevation in the hot riser.

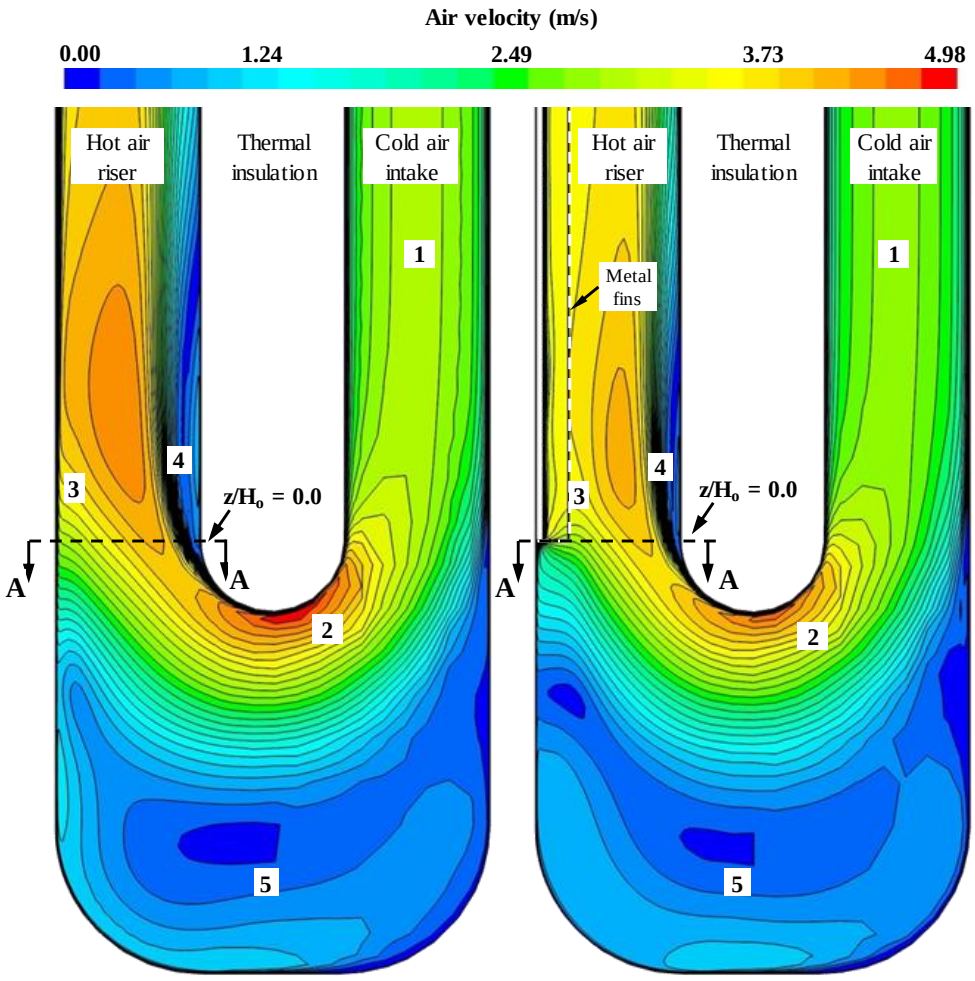

(a) Without metal fins A - A (b) With metal fins A' – A'

Fig. 5.8. Calculated velocity contours and mixing vortices of air flow at entrance of the hot riser.

Figure 5.8a shows the air velocity contours at point (3) near the bottom of the hot riser, where there are no metal fins along the guard vessel wall. At point (4), the rising hot air travels tangential to the reactor guard vessel surface, resulting in a flow-stagnation along the steel liner, on the opposite wall of the riser. The image in Fig. 5.8b shows that the developing air flow pattern near the entrance of the hot riser is similar to that in Fig. 5.8a. This is except that at point (3), the air flow turns quicker due to the presence of the metal fins along the guard vessel wall. The image in Fig. 5.8a shows that the air velocity between the fins is slightly lower than that of the bulk flow in the hot riser. Without and with metal fins, the air stagnates at point (5), at bottom of the hot riser and cold air intake duct (Figs. 5.8a,b).

5.7. Contribution of Thermal Radiation and Natural Convection

This section presents the results of the performed 3-D thermal-hydraulics and CFD analyses, which quantify the partial contributions of thermal radiation and natural convection of ambient air to the total rate of removing the decay heat from the outer surface of the guard vessel of VSLLIM reactor. The results are for a nominal reactor power before shutdown of 10 MW_{th}, and an unlikely malfunction of the in-vessel Na-Na HEX. Because of the relatively high surface temperature of the guard vessel wall (Figs. 5.5-5.7), thermal radiation to the steel liner, on the opposite wall of the annular hot air rise, is a primary contributor to removing the decay heat from the vessel surface.

The heat deposited in the steel liner is removed by natural convection of the ambient air flowing upward in the hot riser. Air natural convection also contributes to the decay heat removal from the surface of the guard vessel wall. The presented results in Fig. 5.8 are for the same average temperature ($\bar{T}_{Na}$) of 682 K at the liquid sodium circulating through the downcomer, immediately after the VSLLIM reactor shutdown.

The pie chart in Fig. 5.9a shows that, without metal fins along the outer surface of the guard vessel wall, the total decay heat removal rate, immediately after reactor shutdown, is ~244 $kW_{th,}$ of which 48% is dissipated by thermal radiation to the steel liner, where it is subsequently removed by natural convection of ambient air in hot riser. The remaining 52% is removed directly from the surface of the guard vessel wall by natural convection of air in the hot riser.

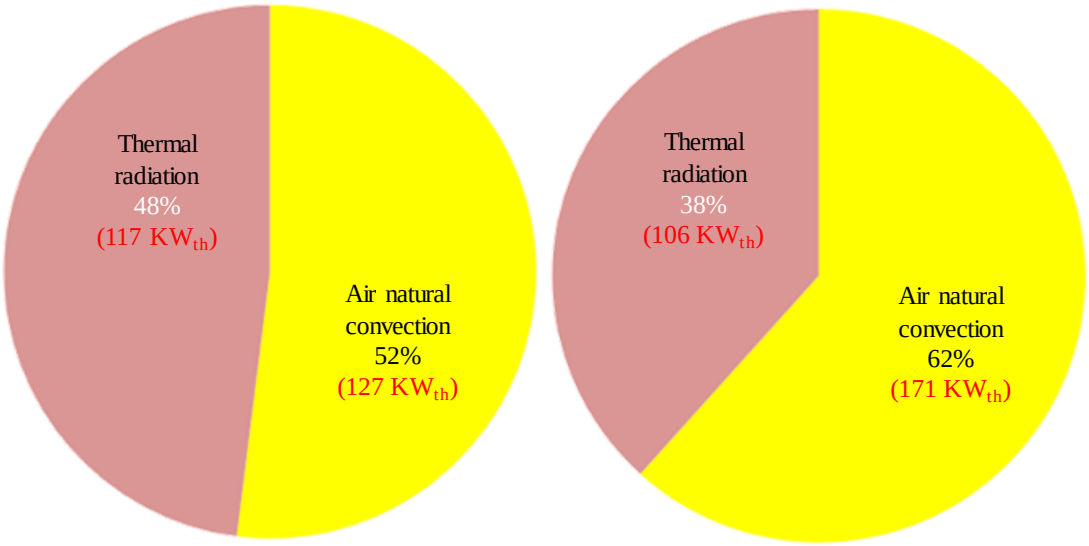

(a) Without metal fins ($\overline{T}_{Na}$ = 682 K, P_{Air} = 244 KW$_{th}$)

(b) With metal fins ($\overline{T}_{Na}$ = 682 K, P_{Air} = 277 KW$_{th}$)

Fig. 5.9. Estimates of contributions of thermal radiation and natural convection to the decay heat removal from the outer surface of VSLLIM's guard vessel wall.

With metal fins along the guard vessel wall outer surface (Figs. 3.4a, 2, 5.1b and 5.2b), the total decay heat removal rate by ambient air flowing in the hot riser increases by ~13.5% to 277 kW$_{th}$. However, the contribution of thermal radiation decreases to 38%, and the contribution natural convection of ambient air directly from the outer surface of the guard vessel increases to 62%. The decrease in the thermal radiation contribution is because metal fins reduce the surface temperature. Conversely, the induced flow mixing and the increased surface area (~10%) increase the rate of decay heat removal by natural convection of air from the guard vessel wall with metal fins. These results confirm the importance of having a steel liner on the opposite wall of the annular hot riser for enhancing the rate of decay heat removal from the outer surface of the VSLLIM reactor guard vessel, with and without metal fins.

5.8. Total Rate of Decay Heat Removal with Time After Reactor Shutdown

As the decay heat generation rate in the core of the VSLLIM reactor decreases with time after shutdown, so does the average temperature of the in-vessel liquid sodium ($\overline{T}_{Na}$), circulating in the downcomer of the VSLLIM reactor primary vessel (Figs. 3.8, 5.1). The obtained results of the total rate of decay heat removal from the outer surface of

guard vessel wall by natural convection of the ambient air in the hot riser are plotted in Fig. 5.10, versus the average temperature of the in-vessel liquid sodium in the downcomer ($\bar{T}_{Na}$). The results in this figure are for three cases: (a) without metal fins along the outer surface of the guard vessel wall, (c) with metal fins along the outer surface of the guard vessel wall, and (c) without metal fins along the outer surface of the guard vessel wall but with 50% reduction of the width of the cold are intake duct, δ_{cold} (Figs. 3.8, 5.1)

Figure 5.10 shows that total decay heat removal by natural circulation of ambient air decrease almost exponentially as the average temperature of the in-vessel liquid sodium in the downcomer ($\bar{T}_{Na}$) decreases. Results show that, with metal fins on the outer surface of the guard vessel wall, the total rate of decay heat removal by ambient air in the hot riser (Figs. 3.8, 5.1) is higher than without metal fins. The difference, however, decreases rapidly with time after the VSLLIM reactor shutdown or decreasing ($\bar{T}_{Na}$).

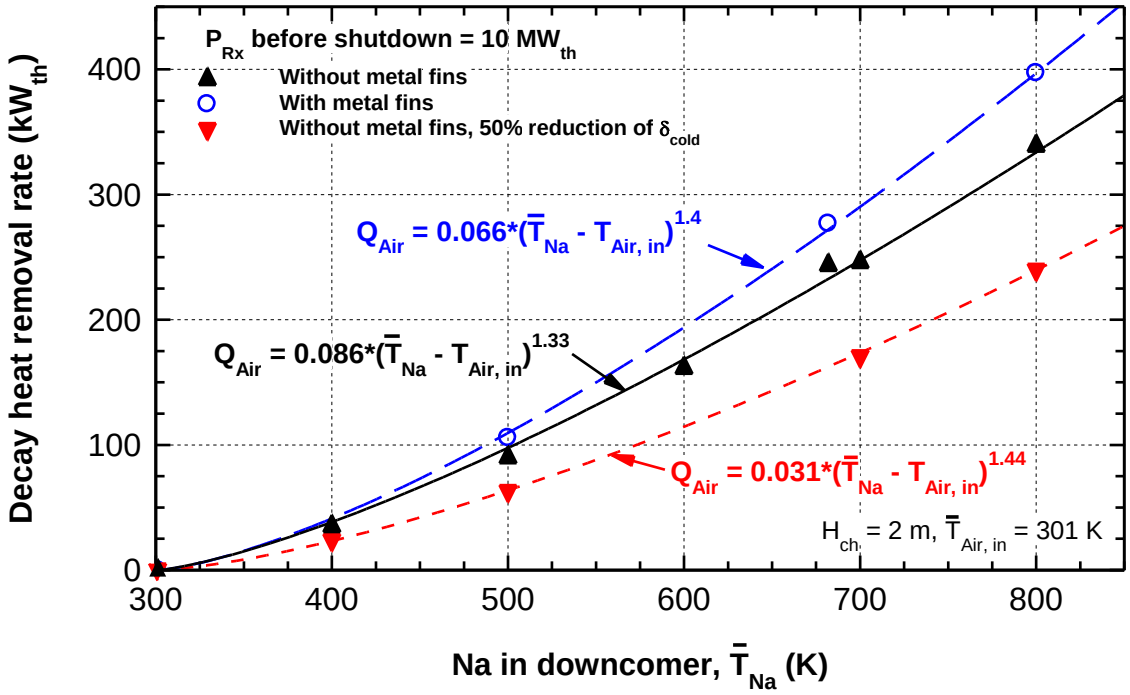

Fig. 5.10. The total rate of decay heat removal by natural circulation of ambient air as function of the average sodium temperature in the downcomer, ($\bar{T}_{Na}$).

Reducing the width of the cold air intake decreases the total rate of decay heat removal from the outer surface of the guard vessel wall by ≤ 35%. For all three options in Fig. 5.10, the natural circulation of ambient air is more than adequate for removing the

decay heated generating in the VSLIMM reactor core after shutdown, following a malfunction of the in-vessel Na-Na HEX (Figs. 3.8, 5.1). Thus, the selection among the option delineated in Fig. 5.10, would be based on the desired time for the in-vessel liquid sodium to cool down to 400 K (~ 29 K above the freezing point) (Figs. 5.11a, b).

The results presented in Figs. 5.11a-c, are for a reduced width of the annular cold air intake duct (Figs. 3.8, 5.1), and with and without metal fins on the outer surface of the guard vessel wall. Results in Figs. 5.11a,b show that the difference between $\bar{T}_{Na}$ and the temperature of the air exiting the hot rise, immediately after reactor shutdown, is ~ 240 K and 420 K, without and with metal fins, respectively. These temperature differences decrease exponentially with time after reactor shutdown, commensurate with the decrease in the rate of decay heat generation in the VSLLIM reactor core.

The results in Figs. 5.11c, d, compare the rate of decay heat generation in the reactor core to that of the heat removal from the outer surface of the guard vessel wall by the natural circulation of the ambient air (Figs. 3.8, 5.1), with time after shutdown. The results in Figs.5.11c show that without metal fins on the outer surface of the guard vessel, the rate of decay heat removal by natural circulation of ambient air is higher than that of decay heat generation in the VSLLIM only during the first 0.34 hrs after shutdown. With metal fins along the guard vessel wall, this time decrease to ~ 0.2 hr (Fig. 5.11d). Hence thereafter, the rate of decay heat generation in the core drops below that removed by natural circulation of ambient air. This causes decreasing the average temperature of the in-vessel sodium to decrease rapidly with time after shutdown (Figs. 5.11a, b). In order to reduce the cooling rate of the in-vessel liquid sodium with time after shutdown, the width of the annular cold air intake duct, δ_{cold} (Figs. 3.8, 5.1) is reduced by 50%. The obtained results are presented in Fig. 5.12.

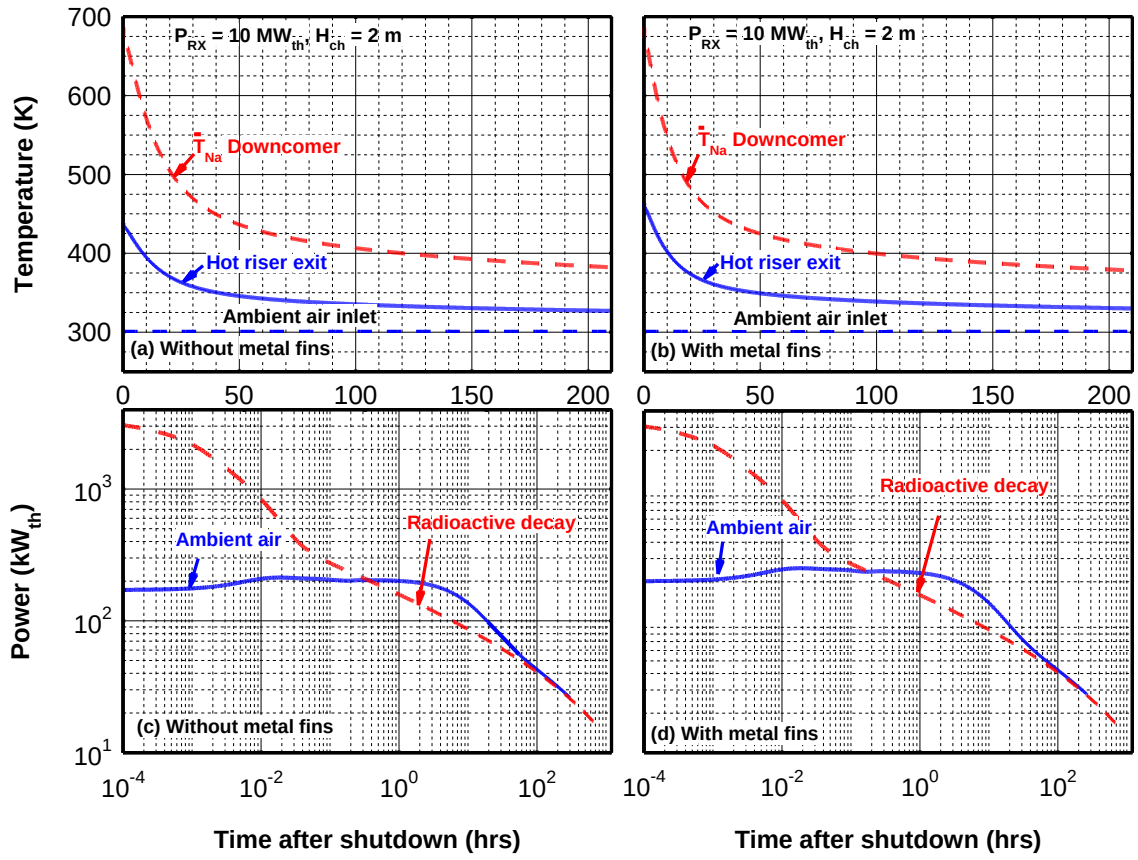

Fig. 5.11. Changes in $\overline{T}_{Na}$, air temperature exiting hot riser, and the rates of decay heat generation and removal by natural circulation of ambient air, versus time after shutdown.

Figure 5.12a,b present the results for the case without metal fins along the guard vessel wall, and with 50% reduction in the width of the cold air intake duct. The latter decreases the rate of decay heat removal by natural circulation of ambient air and maintains the average temperature of the in-vessel liquid sodium in the downcomer of the VSLLIM reactor almost constant at ~678 K during the first 3 hrs after reactor shutdown. During the same time period, the temperature of the ambient air exiting the hot riser (Figs. 3.8, 5.1) is almost steady at ~ 467.5 K (Fig. 5.12a). Hence thereafter, the temperatures of the in-vessel liquid sodium in the reactor primary vessel and that of the ambient air exiting the hot riser decrease almost exponentially with time after shutdown, and so is the difference between these temperatures.

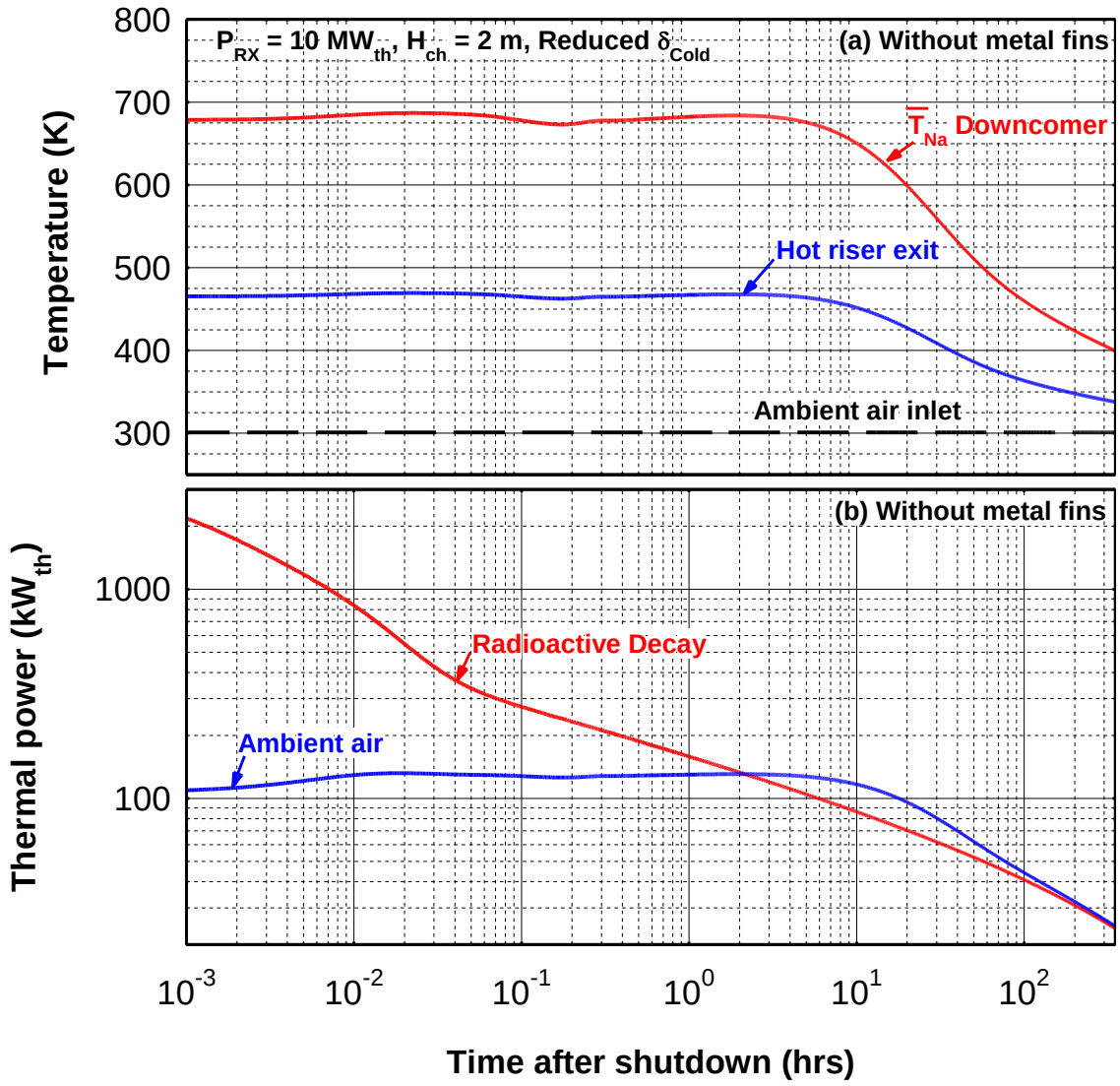

Fig. 5.12. Effects of reducing the width of the cold air intake duct on the passive decay heat removal from the outer surface of the VSLLIM reactor's guard vessel wall.

The results in Fig. 5.12b, shows that during the first 2 hrs after shutdown, the rate of decay heat generation in the core of the VSLLIM reactor is higher than that of the heat removal from the outer surface of the guard vessel by natural circulation of ambient air. Beyond this time, the decay power drops below that removed by ambient air, causing the average temperature on the in-vessel liquid sodium to decrease (Fig. 5.12a). As this figure shows, it would take ~ 346 hrs (> 2 weeks), after the reactor shutdown, for the average temperature of the in-vessel liquid sodium decrease to 400 K. The results presented in figure 5.12 confirm the effectiveness of natural circulation of ambient air for

passively and safely removing the decay heat generated in the VSLLIM core after shutdown, following an unlikely malfunction of the in-vessel Na-Na Hex. The results in Figs. 5.11, 5.12 demonstrate that there would be a large temperature margin (~ > 470 K) from the boiling temperature of in-vessel liquid sodium (~1156 K at 0.1 MPa) after reactor shutdown, while removing the decay heat by natural circulation of ambient air along the surface of the guard vessel (Figs. 3.8, 5.1)

5.9. Summary

Presented are the results of 3-D CFD and thermal-hydraulics analyses that confirmed the effectiveness of natural circulation of ambient air for safely and passively removing the decay heat generating in the core of the VSLLIM reactor after shutdown. The results of the performed CFD and thermal-hydraulics analyses demonstrated that passive decay heat removal after a reactor shutdown, following an unlikely malfunction of the in-vessel Na-Na HEX, is possible with and without metal fins along the outer surface of the guard vessel wall. The metal fins increase the rate of decay heat removal by natural circulation ambient air by ~ 13.5%. Thus the time after shutdown, when the rate of decay heat generation in the reactor core drops below that removed by natural circulation of ambient air, decreases from 0.34 to 0.2 hr. Reducing the width of the cold air intake duct by 50%, without metal fins along the guard vessel wall, decreases the rate of decay heat removal by natural circulation of ambient air by 35%. The reduced rate is still safe and more than adequate extends the time for the average temperature of the in-vessel liquid sodium to cool down to 400 K, from ~100 hr. (or > 4 days) to as much as 346 hrs. (or > 2 weeks).

6. CFD ANALYSES AND FRICTION FACTOR CORRELATION FOR HEXAGONAL ROD BUNDLES

Hexagonal bundles of bare tubes and with flat walls are being used in many industrial applications such as oil refineries, terrestrial and space nuclear reactors, desalination, waste heat recovery, and compact heat exchangers. Hexagonal bundles, loaded with different number of nuclear fuel rods in a triangular lattice (Fig. 6.1a), have been used and are used in liquid-metals large, medium and in small modular nuclear reactors (SMRs) (El-Genk et al., 2017; IAEA , 2012, 2014, 2016; Ingersoll et al., 2014; Ueda et al., 2005; El-Genk and Palomino, 2015; Palomino and El-Genk, 2016; Westinghouse 2016; Babcock and Wilcox, 2011; Triplett et al., 2012, Smith et al., 2008; Choi et al., 2011; Zhang, 2013).

Some of the liquid metal cooled SMRs are cooled by natural circulation of in-vessel liquid metals, such as sodium-potassium (NaK) alloy, sodium, lead, or lead-bismuth (LB) alloy, or molten salt, during both normal operation and after shutdown (Ueda et al., 2005; Triplett et al., 2012, Smith et al., 2008; Choi et al., 2011; El-Genk et al., 2008; Zhang, 2013). In this mode of operation, the friction pressure losses in the bundles are a major contributor to the total pressure losses in the reactor core, and hence the circulation rate and temperature of the liquid metal coolant exiting the core (Haskins and El-Genk. 2017; El-Genk et al., 2008).

In flat-walled hexagonal bundles, the flow distribution is not radially uniform, with more of the liquid coolant flowing next to the wall where the local porosity is higher than the central channels. Such mal-distribution of the flow affects both the temperature of the individual fuel rod as well as the pressure losses in the bundles. The bundle friction factor, f_b, also depends on the fluid properties and flow rate as well as the geometrical parameters of the bundle (D, P, W) (Fig. 6.1a). The friction factor has typically been determined as a weighted average of those of the central, corner and wall sub-channels, which are highlighted in Fig. 6.1a (Rehme, 1971, 1972, 1973; Cheng and Tadreas, 1986; Su and Freire, 2002).

For the same diameter, D, and the P/D of the tubes or rods in the hexagonal bundles, W/P affects equivalent hydraulic diameter of the bundle, D_e, (Fig. 6.2) and thus the contributions of the corner and wall sub-channels to the friction factor, f_b, and the fluid

flow through the bundles. For bundles of bare tubes or rods and with flat walls (Fig. 6.1a), D_e, is expressed, as:

$$D_e = D\left[\left(\frac{2\sqrt{3}}{\pi}\right)\left(\frac{P}{D}\right)^2\beta - 1\right]\Big/\left[\left(\frac{2\sqrt{3}}{\pi}\right)\left(\frac{P}{D}\right)\sqrt{\frac{\beta}{N}} + 1\right], \text{ where,} \quad (6.1a)$$

$$\beta = \frac{1}{N}\left[\frac{\sqrt{3}}{2}\left(\frac{\sqrt{3(4N-1)}}{3} - 1\right) + \frac{2*W/D-1}{P/D}\right]^2, \quad (6.1b)$$

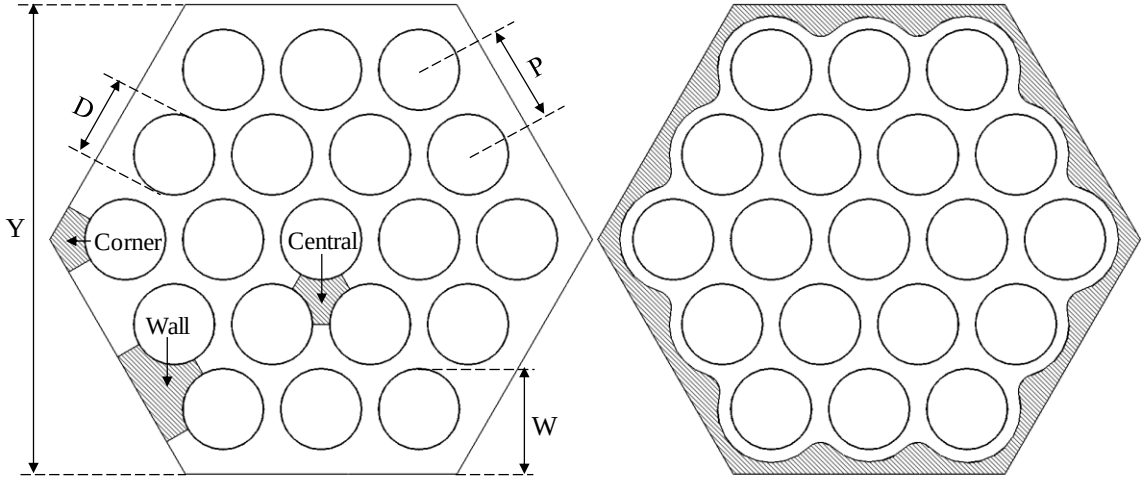

(a) 19 Rod hexagonal bundle with flat walls

(b) 19 Rod hexagonal bundle with scalloped walls

Fig. 6.1. Cross-sectional views of 19-rod hexagonal bundle with flat and scalloped walls.

For hexagonal bundles with scalloped walls (Fig. 6.1b), D_e, is calculated numerically. For very large number of tube or rods, N, the parameter β in Eq. (6.1b) approaches unity and the parameter $\sqrt{\beta/N}$ in Eq. (6.1a) approaches zero, reducing the expression of the bundle equivalent hydraulic diameter in Eq. (6.1a) to that of the subchannel (Fig. 6.1a), $D_{e,sub}$, as:

$$D_{e,sub} = D\left[\left(\frac{2\sqrt{3}}{\pi}\right)\left(\frac{P}{D}\right)^2 - 1\right] \quad (6.1d)$$

This expression for the central subchannel (Fig. 6.1a) applies to the bundles with either flat or scalloped walls (Fig. 6.1).

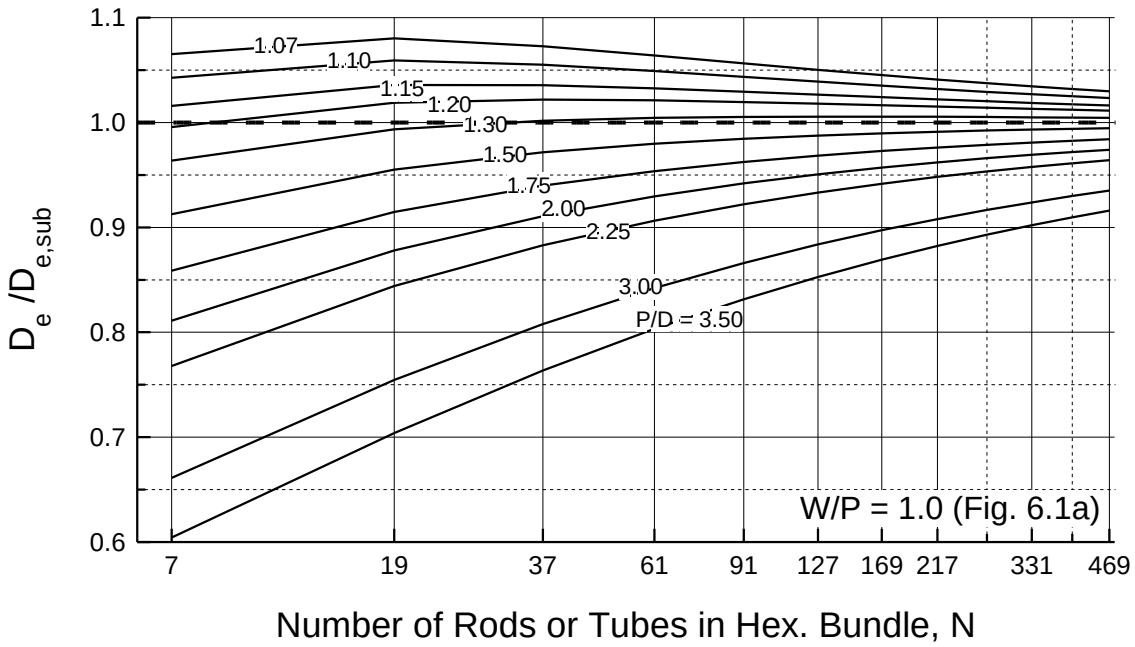

Fig. 6.2. Ratio of the equivalent hydraulic diameters for bundles with flat walls, D_e, to that of the central subchannel, $D_{e,sub}$.

Fig. 6.2 shows that the equivalent hydraulic diameter for bundles of bare tubes in a triangular lattice and with flat walls, D_e, strongly depends on P/D and the number of tubes or rods, N. Increasing P/D or decreasing N, decreases D_e, relative to that of the central subchannel, $D_{e,sub}$. The bundles D_e approaches $D_{e,sub}$ with increased N or decreased P/D. For P/D > 1.3 and N > 19, D_e is smaller than $D_{e,sub}$, but for smaller P/D values, D_e is slightly larger than $D_{e,sub}$. For all P/D values in Fig. 6.2, the difference between De and $D_{e,sub}$ decreases as N increases. The values of D_e would affect those of the friction coefficient, which increase with decreased D_e. It is worth noting, however, that the results in Fig. 6.2 and in the rest of the paper are for W/P = 1.0.

The friction drag at the walls of the bundles affects the contributions of the wall and of the corner sub-channels to bundle's friction factor. For same or close values of P/D and W/D (Fig. 6.1a) the cross-sectional flow areas, and hence the flow rates per rod in the corner, wall, and the interior subchannels are not the same. This difference affects not only the friction factor, but also the cooling and the operating temperatures. For the same inlet flow Reynolds number, Re_{in}, the friction factor of the bundle increases with increased P/D and / or decreased D_e.

To ensure almost the same flow rate per rod in the central, corner and wall sub-channels, hexagonal bundles with scalloped walls (Fig. 6.1b) have been considered in recently developed Small Modular Reactor (SMR) designs, which are cooled by natural circulation of in-vessel liquid sodium, both during nominal operation and after shutdown such as the SLIMM and VSLLIM (El-Genk et al., 2017; Haskins and El-Genk, 2017; El-Genk and Palomino, 2015; Palomino and El-Genk, 2016). Scalloping the bundle wall (Fig. 6.1b), effectively enhances the uniformity of the flow in the bundle, and hence the friction factor and the temperatures of the fuel rods in the various sub-channels. To the best of the author's knowledge, no experimental or theoretical work has been reported on determining the friction factor in hexagonal bundles of bare tubes or rods and with scalloped walls (Fig. 6.1b).

6.1. Introduction and Background

The flow condition in the hexagonal bundles with either flat or scalloped walls (Fig. 6.1) could be either laminar ($Re_{in} < 10^3$), transition ($10^3 < Re_{in} < 10^4$), or turbulent ($Re_{in} > 10^4$). Thus, in order to avoid discontinuities at the transition between these flow regions, it is desirable to develop a continuous correlation of the friction factor that is applicable in all three flow regions, which is a primary objective of the present work.

Historically, the focus of the reported experimental and theoretical work on the friction factor in hexagonal with flat walls has been mostly turbulent flow, with much less data in the laminar and transitional flow regions (Rehme, 1972, Cheng and Todreas, 1986; Fakory and Todreas, 1979, Trupp and Azad, 1975, Su and Freire, 2002; Vijaya et al., 1999; Engel et al., 1979; Gajapathy et al., 2009). As a result, the available experimental data of the friction factor for laminar flow ($Re_{in} < 10^3$) is scarce and insufficient to develop a reliable correlation (Fig. 6.3).

The reported correlations of the friction factor for laminar flow in hexagonal bundle of bare tubes and with flat walls have been based on either analytical or numerical solutions of the Navier-Stokes equations for incompressible, fully developed, and isothermal flows in the central sub-channel (Fig. 6.1a) (Rehme, 1972; Cheng and Todreas, 1986). Fig. 6.3a-d compares the reported correlations by Rehme (1972) and Cheng and Tadreas (1986) to available experimental data of the friction factor for laminar flow in flat-walls hexagonal bundles of different tubes or rods and P/D values. The solid

lines in these figures are those of the predicted mean values of the friction factor calculated using the reported correlations, and the P/D values for the experimental data by Rehme (1972).

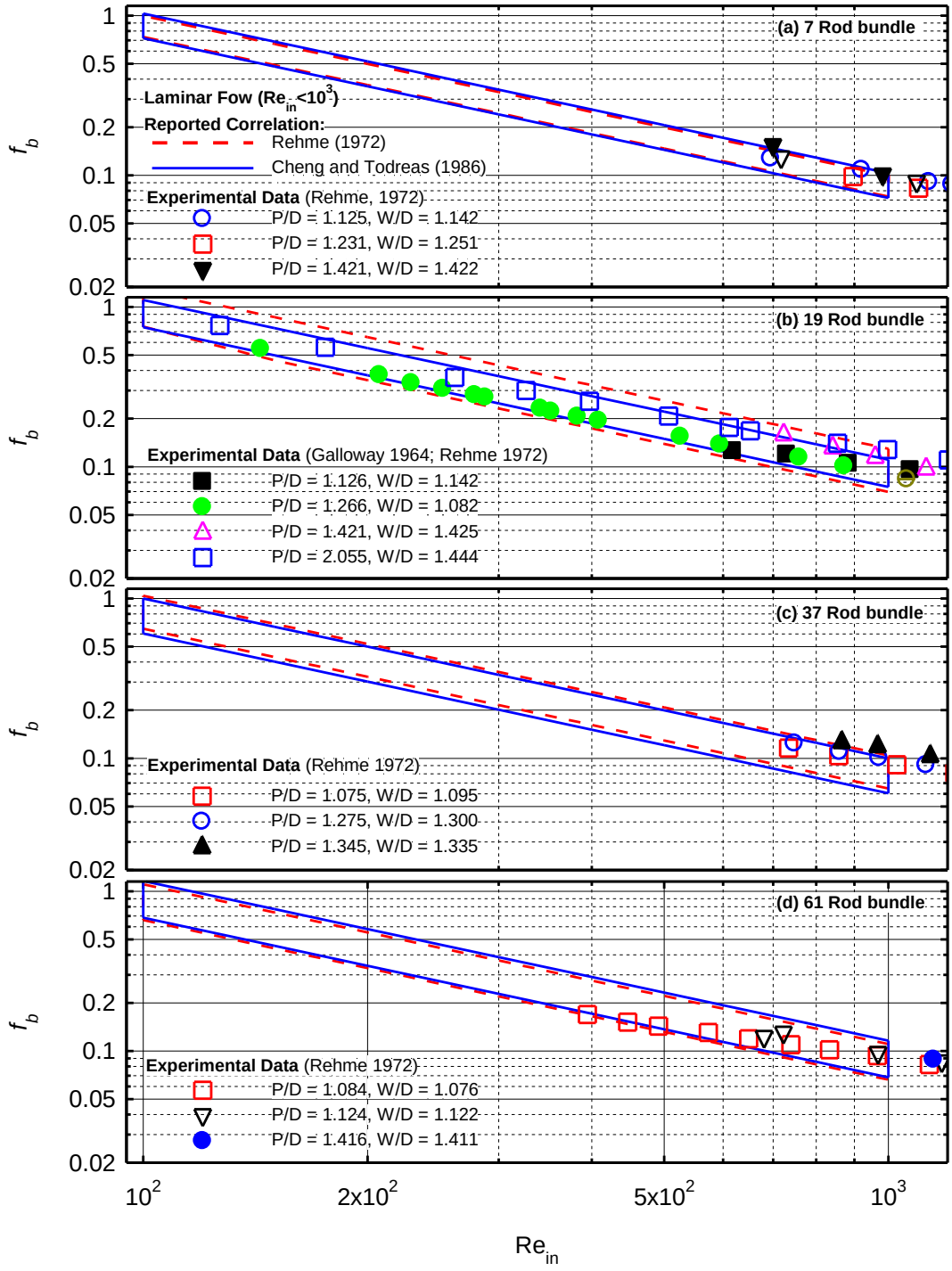

Fig. 6.3. Friction factor data and correlations for laminar flow in bare tubes hexagonal bundles with flat walls.

The laminar flow friction factor in hexagonal bundles, f_l, increases with increased P/D, but decreases with increased Re_{in}, and can generally expressed as:

$$f_l = A / Re_{in} \quad (6.2)$$

In this expression, the geometrical parameter "A" increases with increased P/D. The reported friction factor correlations by Rehme (1972) and Cheng and Todreas (1986) have the same form as Equation (6.2), but the values of geometrical parameter "A", are different. They were calculated using different methods involving several steps, based on the similarities to isothermal and incompressible fully developed flows in circular tubes or annuli.

Figures 6.3a-d, show the close predictions of the friction factor correlations of both Rehme (1972), and Cheng and Todreas (1986) for laminar flow in hexagonal bundles with flat wall. The difference is solely due to the different values of the parameter "A" in the respective correlations. The experimental data of the friction factor for laminar flow in Figs. 6.3a-d is very limited to validate these correlations, particularly for bundles with 7, 37, and 61 bare tubes or rods (Figs. 6.3a, c, and d). For the 19 rod bundle, however, there is relatively more experimental data for four P/D values.

The friction factor correlation by Rehme (1972) is slightly higher than the experimental data, while that of Cheng and Todreas (1986) agrees better with the data for $Re_{in} < \sim 7x10^2$, and but lower than the data for $7x10^2 < Re_{in} < 10^3$. Nonetheless, both correlations show that increasing P/D increases the friction factor for laminar flow, which is consistent with the trend indicated by the experimental data (Rehme, 1972). The analytical solutions for developing the friction factor correlations for laminar flow ($Re_{in} < 10^3$) by Rehme (1972) and Cheng and Todreas (1986), neglect the entrance flow mixing in the bundles. Although this effect might be negligible for tall bundles, it would affect the values of the friction factor for shorter bundles. Such an effect would not be possible to quantify based on the limited experimental available (Fig. 6.3a-d). Therefore, there is need to obtain additional experimental data of the friction factor for laminar flow in hexagonal bundles, which could be expensive and time consuming.

An alternative and less expensive approach to experiments is to use Computational Fluid Dynamics (CFD) to investigate friction pressure losses in hexagonal rod bundles of

bar tubes or rods for a wide range of geometrical and operation parameters, including the number, N, diameter, D, P/D and W/D of the bare tubes or rods, and $Re_{in} < 10^3$. The compiled database of the numerical results and reported experiment data could then be used to develop a correlation of the friction factor and validate the reported correlations by Rehme (1972) and Cheng and Tadreas (1986). However, the refinement of the implemented numerical mesh in the CFD analyses would need to be confirmed for convergence and for accuracy by comparing results to exiting experimental data.

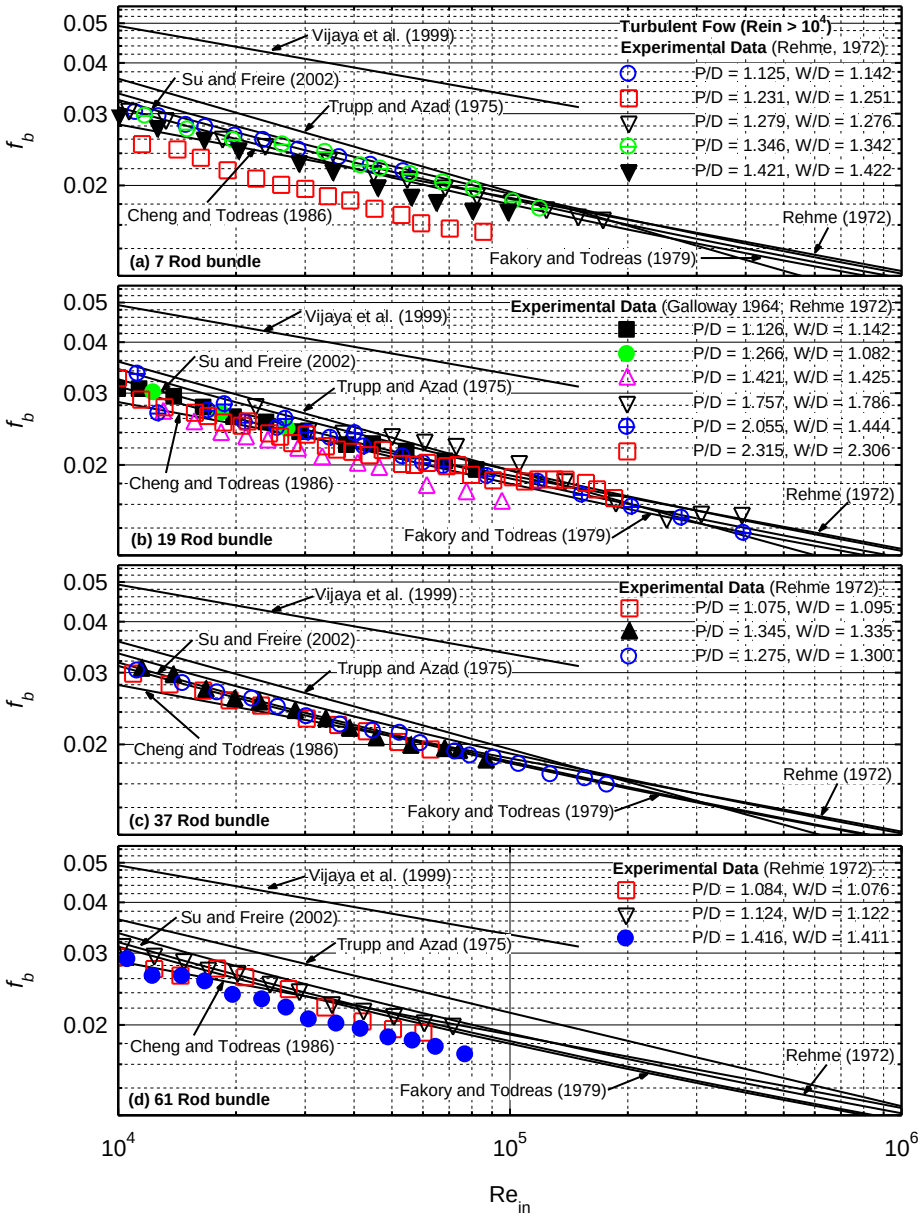

Fig. 6.4. Friction factor data and correlations for turbulent flow in bare tubes hexagonal bundles with flat walls.

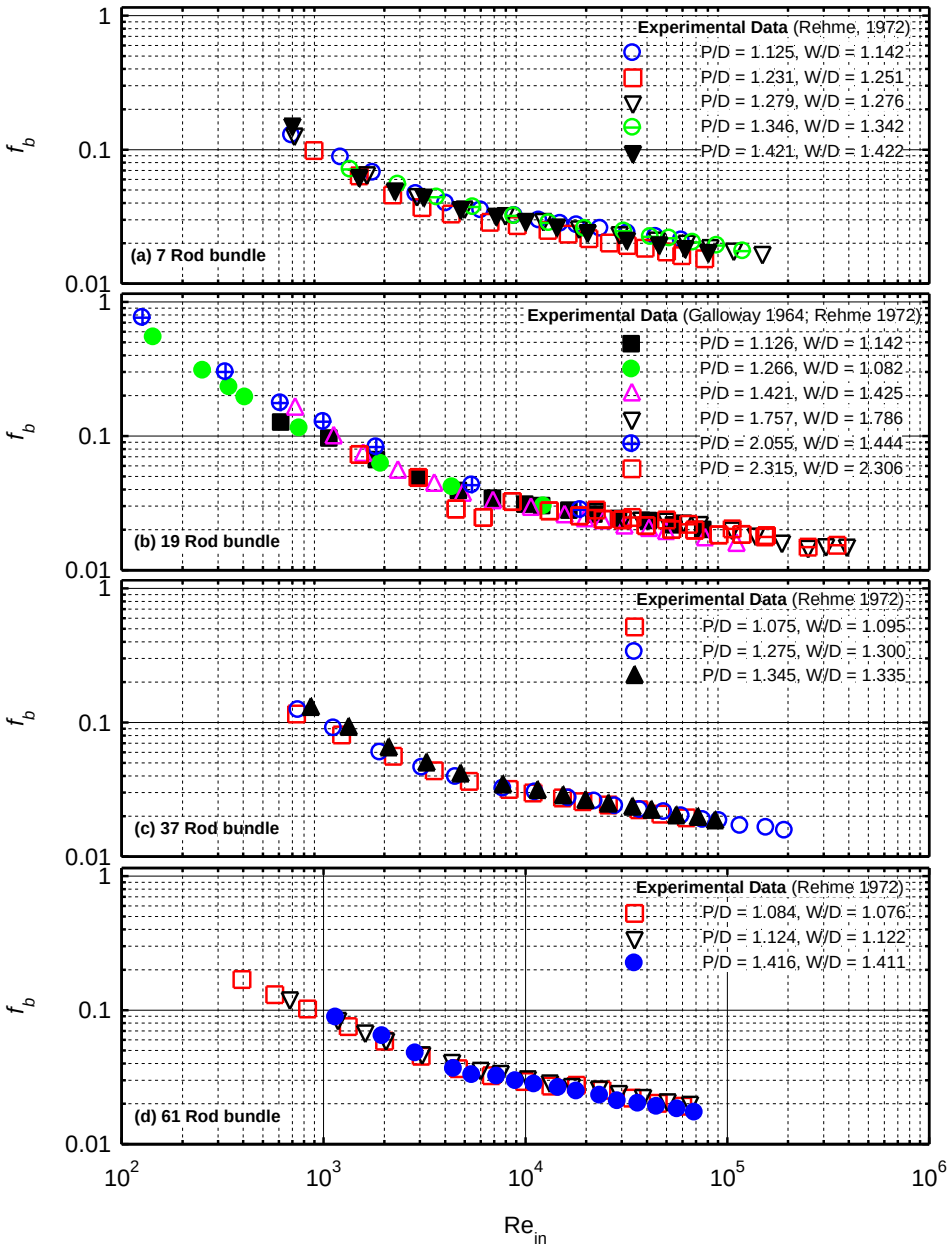

Fig. 6.5. Some of the reported experimental data of the friction factor in hexagonal bundles of bare tubes and with flat walls (Rehme, 1972).

6.2. Needs

There is a large experimental database (Fig. 6.4) of the friction factor in hexagonal bundles of bare tubes or rods and with flat walls in the transition ($10_3 < Re_{in} < 10^4$) and the turbulent ($Re_{in} > 10^4$) flow regions (Rehme, 1972). However, all reported correlations (Figs. 6.4a-d) of the friction factor have been limited to the turbulent flow region, and

thus could not be extended to the transition flow region (Rehme, 1972; Cheng and Todreas, 1986; Fakory and Todreas, 1979; Trupp and Azad, 1975; Su and Freire, 2002; Vijaya et al., 1999). Despite the smooth decrease in the reported experimental data of the friction factor in the various flow regions in hexagonal bundles with increased Re_{in} (Laminar, transition, and turbulent), there is no continuous correlations, that span all three flow regions, have been reported.

The comparisons in Fig. 6.4a-c, of the friction factor experimental data and the reported correlations for the turbulent flow region, show a divergence between the data and the correlation. Although, consistent with the trend displayed by the experimental data of the friction factor decreasing with increased Re_{in}, some of the correlations seem to over predict the friction factor (e.g., Su and Freire, 2002; and Trupp and Azad, 1975). The correlation by Vijaya et al. (1999), significantly over predict the friction factor for turbulent flow in hexagonal bundles by more than 60%. The closest correlation to the reported experimental data are those of Rehme (1972), Cheng and Todreas (1986), and Fakory and Todreas (1979).

As for laminar flow, the experimental data in Fig. 6.4a-d show that the friction factor for turbulent flow increases with increased P/D. In summary, there is a need to develop a consistent correlation of the friction factor for turbulent flow that is not only accurate, but also in good agreement with the reported experimental data, subject to the inherent uncertainties in the data. In addition, it is desirable to avoid having separate correlations in the various flow regions, as this causes discontinuities at the transition among the flow regions. Instead, it is preferable and useful to develop a continuous friction factor correlation that is applicable to all three all flow regions, and in good agreement with the reported experimental data (Rehme, 1972), e.g. Fig. 6.5. This would require having proportionally more data in the laminar flow and transition regions (Figs.6.3 and 6.4).

6.3. Objectives

The objectives of the present work are to perform CFD analyses of the pressure losses in hexagonal bundles of bare tubes and with flat walls, for wide ranges of, N, Re_{in} and P/D, and confirm the convergence of the CFD results by investigating the effect of increasing the refinement of the numerical mesh grid on the calculated values of the friction factor. Additional objectives are:

(a) Confirm the accuracy of the CFD methodology and the selected mesh grid refinement by comparing the calculated values of the friction factor with the reported experimental data (Rehme, 1972) for different bundle sizes and values of Re_{in}, in the laminar, transition and turbulent flow regions.

(b) Use the confirmed CFD methodology, for convergence and accuracy, to obtain additional friction factor values in the laminar flow and transition regions that complement the reported experimental data.

(c) Based on the compiled database of the numerical results and the reported experimental values (Rehme, 1972), develop a continuous correlation of the friction factor for hexagonal bundles of bare tubes and with flat walls, that traverses all flow regions.

(d) Conduct additional CFD analyses to calculate the friction factor for laminar, transition, and turbulent flows in hexagonal bundles of 19 and 37 bare tubes, but with scalloped walls (Fig. 6.1b), for a wide range of Re_{in}.

(e) Compare the results from (d) with the developed friction factor correlation in (c), and quantify the effect of using scalloped, instead of flat, walls on the friction factor in bundles of bare tubes or rods.

6.4. Approach and Methodology

The CFD analyses of the pressure losses in bare tubes' hexagonal bundles with flat and scalloped wall are carried out using the shear stress transport (SST) k-ω turbulence model with segregated flow in the STAR-CCM+, commercial Code package version 12.02.010 (CDADAPCO, 2017). The analyses are for incompressible, isothermal and fully developed water flow at constant inlet temperature of 295 K, non-slip at the walls, and constant exit pressure. The analyses used the SST k- ω turbulence model (Menter 1994). This model takes advantage of the accuracy of the original k- ω model in the boundary layer at the solid surfaces and that of the k-ε turbulence model in the free stream of the bulk fluid flow. This is the flow between the tubes or rods in the center region of the bundle and between the outer row of tube or rods and the adjacent walls (Fig. 6.1).

Figure 6.6 presents a cross-sectional view of the employed setup of a flat walls hexagonal bundle loaded with 19 bare tubes or rods. This setup is used in the experiments

by Rehme (1972) for different bundle sizes (Table 6.1). In the experiments (Rehme, 1972), as well as in the present CFD analyses, the length of the test section, L_b, for all size bundles is 1000 mm. It is preceded by an entrance section, L_{in} = 250 mm, to allow the water flow to hydrodynamically develop before entering the test section, which is followed by 250 mm long exit section. This section minimizes the exit effect on the measured pressure losses calculations in the test section (Fig. 6.6).

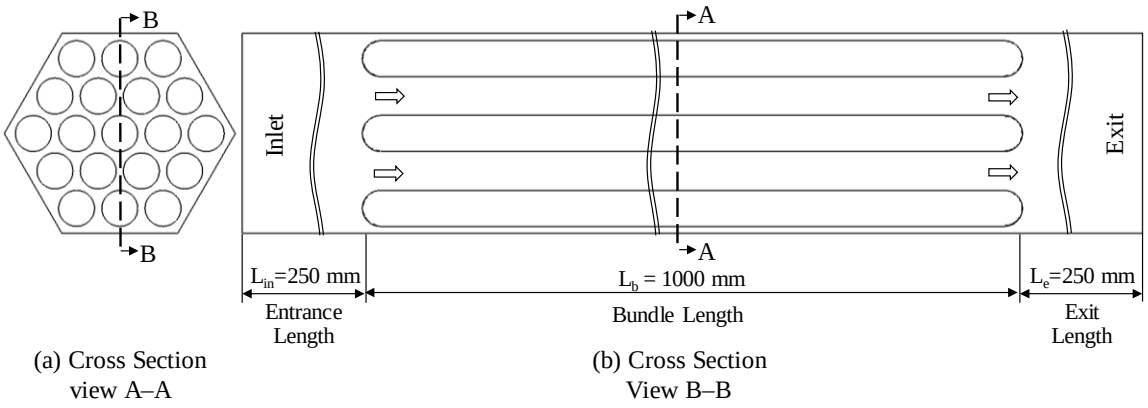

Fig. 6.6. The experimental setup of a 19 rod hexagonal bundle, with flat walls (Rehme, 1972); this setup and dimensions are duplicated in the present CFD analyses for hexagonal bundles of different sizes and P/D values (Table 6.1).

The water entering the entrance section, L_{in}, has a uniform velocity. The value of the velocity depends on the Re_{in} at 295 K. In the CFD analyses, the pressure at the end of the exit length in Fig. 6.6 is kept constant. The calculated total pressure losses in the bundle, ΔP_b, are used to determine the corresponding values of the friction factor, in terms of D_e and Re_{in}, as (Welty et al., 2007):

$$f = \left(2\,\Delta P_b / Re_{in}^2\, L_b\right)\left(\rho_{in}\, D_e^3 / \mu_{in}^2\right) \qquad (6.3)$$

In this relationship all fluid properties are evaluated at the inlet temperature of 295 K.

The flow pressure decreases linearly with distance from the entrance of the test section (Fig. 6.5). In order to reduce the computation time and requirements, the computational domain used in the CFD analyses is only 1/6 of the total volume of the bundle, with symmetry boundary conditions. This approach significantly reduces the

number of mesh elements and the computation time for convergence, (Table 6.2), without compromising the accuracy of the results. These computation requirements also depend on the turbulence model used and the refinement of the numerical mesh grid in the analyses.

Table 6.1. Dimensions and test conditions in the experiments* of Rehme (1972) for determining the friction number of water flow in hexagonal bundles with flat walls and different number of bare tubes (Figs. 6.1a and 6.6).

Rods / Bundle	D (mm)	P/D	W/D	Y (mm)	A_b (mm^2)	Volume Porosity	p_w (mm)	D_e (mm)	Re_{in}	f, Data Points
7	12	1.125	1.142	38.79	511	0.39	398.27	5.14	$695 - 6x10^4$	40
		1.231	1.251	43.61	855	0.52	414.96	8.25	$896 - 9x10^4$	47
		1.279	1.276	45.21	978	0.55	420.50	9.31	$717 - 1.7x10^5$	39
		1.346	1.342	48.18	1219	0.61	430.81	11.32	$700 - 1x10^5$	39
		1.421	1.422	51.66	1520	0.66	442.86	13.73	$1.3x10^3 - 1.2x10^5$	37
		1.867	1.902	72.45	3754	0.83	514.88	29.17	$2.2x10^4 - 4.1*10^5$	22
		2.324	2.445	94.98	7021	0.90	592.93	47.37	$2.0x10^4 - 5.2x10^5$	19
19	12	1.126	1.142	62.21	1203	0.36	931.80	5.17	$618 - 8.8x10^4$	42
		1.231	1.252	69.22	2001	0.48	956.07	8.37	$830 - 5.8x10^4$	37
		1.276	1.308	72.43	2395	0.53	967.20	9.90	$10^3 - 1.9x10^5$	44
		1.344	1.341	76.05	2860	0.57	979.74	11.68	$703 - 2x10^5$	50
		1.421	1.425	81.27	3571	0.62	997.81	14.32	$723 - 1.1x10^5$	46
		1.757	1.786	103.90	7200	0.77	1076.21	26.76	$2.2x10^4 - 4.4x10^5$	24
		1.865	1.88	110.65	8454	0.80	1099.57	30.75	$2.8x10^3 - 4.0x10^5$	39
		2.315	2.306	139.58	14723	0.87	1199.79	49.08	$1.5x10^3 - 1.8x10^5$	45
37	12	1.075	1.095	81.31	1541	0.27	1676.53	3.68	$1.4x10^4 - 2.8x10^5$	33
		1.235	1.25	95.01	3632	0.46	1723.98	8.43	$866 - 4x10^4$	44
		1.275	1.3	98.70	4252	0.50	1736.78	9.79	$748 - 2x10^5$	52
		1.345	1.335	103.91	5165	0.55	1754.81	11.77	$865 - 9.7x10^4$	44
		1.42	1.42	110.62	6413	0.61	1778.07	14.43	$869 - 9.7x10^4$	43
		1.756	1.754	139.59	12690	0.75	1878.42	27.02	$1.4x10^4 - 2.8x10^5$	33
61	12	1.025	1.06	98.66	1530	0.18	2641.40	2.32	$321 - 1.8x10^4$	35
		1.085	1.076	104.03	2473	0.26	2660.01	3.72	$394 - 6x10^4$	43
		1.124	1.122	108.38	3273	0.32	2675.07	4.89	$681 - 7.1x10^4$	47
		1.416	1.411	139.59	9975	0.59	2783.19	14.34	$1.2x10^3 - 7.7x10^4$	47
169	12	1.317	1.285	210.45	19243	0.50	7100.18	10.84	$10^3 - 8x10^4$	43

*Test section length (Fig. 5), L_b = 1000 mm, water, inlet temperature = 295 K, entrance length = exit Length = 250 mm,

To ensure convergence of the CFD results, the numerical mesh used is progressively refined until the determined values of the friction factor become practically independent of mesh refinement (Table 6.2). Since convergence does not necessary mean accuracy, the latter is quantified from comparing the converged values of the friction factor in the CFD analyses to those reported experimentally by Rehme (1972), and summarized in Table 6.1.

Table 6.2. Numerical mesh refinements used in the present CFD analyses for determining the friction factor in hexagonal bundles with flat walls, and the corresponding relative computational time and the Grid Convergence Index (GCI) by Roache (1994).

Meshing Parameters	**Mesh Type**		
	Coarse	**Fine**	**Finer**
Prism layers / growth multiplier	8/1.25	15/1.25	15/1.50
Boundary layer thickness (mm)	1.0	1.0	1.0
Prism layer t at solid surfaces (mm)	0.050	0.009	0.001
Element at surface / in bulk flow (mm^3)	$5.2x10^3$/0.19	10^3/0.19	10^4/0.19
Prism layer elements / total (Millions)			
• 7 Rod bundle	5.5/8.38	10.3/13.21	10.3/13.21
• 19 Rod bundle	12.5/19.98	23.9/29.95	23.9/29.95
• 37 Rod bundle	19.5/28.86	41.7/53.01	41.7/53.01
• 61 Rod bundle	N/A	N/A	64.8/74.07
Relative computational time	1	1.84	1.85
Grid Convergence Index (GCI)			
• 7 Rod bundle			
➢ *Laminar*	<4.0%	<3.0%	<1.0%
➢ *Transition*	<4.0%	<2.0%	<1.0%
➢ *Turbulent*	<30%	<27%	<1.0%
• 19 Rod bundle			
➢ *Laminar*	<0.01%	<1.4%	<1.0%
➢ *Transition*	<0.9%	<15%	<1.0%
➢ *Turbulent*	<38%	<27%	<2.0%
• 37 Rod bundle			
➢ *Laminar*	<3.0%	<3.0%	<1.0%
➢ *Transition*	<5.9%	<15%	<1.0%
➢ *Turbulent*	<35%	<27%	<1.4

The pressure losses for isothermal and fully developed water flows in flat walls' hexagonal bundles with 7, 19, 37 and 61 bare tubes are calculated for the same tube

diameter of 12 mm, same P/D (1.025 – 2.324) and Re_{in} (10^2-10^6) used in the experiments by Rehme (1972), see Table 6.1. For the hexagonal bundles with scalloped walls (Fig. 6.1b), similar CFD analyses for isothermal, and developed flow of liquid sodium. They calculate the pressure losses and the determine the friction factor values in bundles with 19 and 37 bare tubes or rod, at inlet sodium temperatures of 500 and 800 K, and a wide range of Re_{in} (10^2 – 10^6). These temperatures are higher than the melting temperature of sodium of ~ 371 K at atmospheric pressure (Bomelburg et al., 1975; Thermal Fluids Central, 2016). In these analyses for liquid sodium, the test section length, L_b, equals 1,100 mm, the entrance and exit sections length is 250 mm, the rod diameter is 23.7 mm and the P/D = 1.2.

These dimensions are the same as those of the 37 UN fuel rod bundles loaded in the core of the Scalable, LIquid Metal cooled, small Modular (SLIMM) reactor, and the 19 UN fuel rod bundles in the core of the VSLLIM reactor (El-Genk at al., 2017; El- Genk and Palomino, 2015).

6.5. Verification

This section investigates the effect of increasing the numerical mesh refinement in the performed CFD analyses on the convergence of the friction factor results for the isothermal water flow in flat walls' hexagonal bundles of bar tubes or rods. These bundles are the same as those used in the experiments of Rehme (1972), and listed in Table 6.1. The CFD analyses used hexahedral mesh elements, generated by the trimmer and the surface remesher and the prism layer mesher models in the STAR-CCM+ Code (CD-ADAPCO, 2017). The trimmer mesher option generates uniform hexahedral elements in the bulk flow with an average volume of 0.19 mm^3.

In order to capture the boundary layer effects, the prism layer mesher divides the 1.0-mm thick boundary layer at the solid surfaces of the bare tubes / rods and at the bundle walls, into a number of parallel prismatic layers, whose number depends on the desired refinement of the numerical mesh grid (Fig. 6.7). For the coarse grid, the number of the prismatic layers is 8, with a growth multiplier of 1.25 (Table 6.2 and Fig. 6.7a). For the fine and finer mesh grids (Figs. 6.7b, c) the number of prismatic layers is 15, with a growth multiplier of 1.25 and 1.5, respectively (Table 6.2).

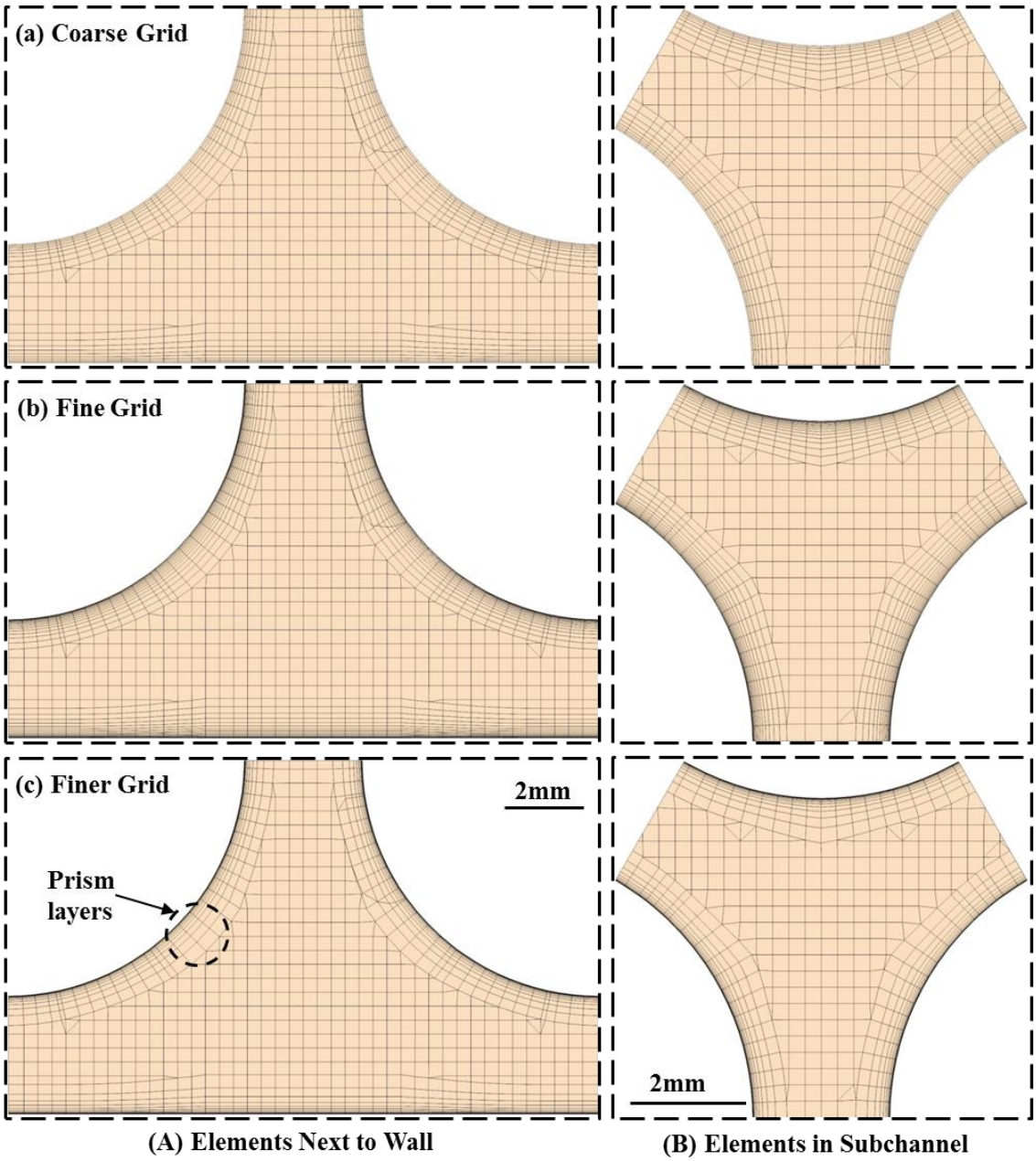

Fig. 6.7. Cross sectional view of the implemented numerical mesh grids in the presents CFD analyses for calculating the friction factors for water and liquid sodium flows in flat and scalloped-walls hexagonal bundles of bar tubes or rods, respectively.

The CFD calculations are performed for hexagonal bundles with 7, 19, and 37 bare tubes or rods with W/P = 1 (Fig. 6.1a), P/D = 1.346, 1.276, and 1.275, respectively, and isothermal water flows at 295 K and Re_{in} = 10^2 to 10^6 (Fig. 6.6). The analyses investigated three numerical mesh grid refinements: coarse, fine, and finer (Fig. 6.7) by

progressively increasing the total number of mesh elements and reducing the size and increasing the number of prism layers in the flow next to the solid surfaces (Fig 6.7a-c and Table 6.2). In all three mesh refinements investigated, the number of the mesh elements in the inlet and exit sections (Fig. 6.6) represent < 1% of the total number of the elements in the computation domain (Table 6.2). In a computational domain that is 1/6 the bundle volume and with symmetry boundary conditions, the total number of mesh elements for the coarse gird is 8.38, 19.8 and 28.86 million for the 7, 19 and 37 rod bundles, respectively. Most of these elements are in the 1.0-mm thick boundary layers, which total 5.5, 12.5 and 19.5 million, for the 7, 19, and 37 rod bundles, respectively.

The fine mesh grid, (Fig 6.7b), increased the total number of mesh elements in the CFD calculation domain for the 7, 19 and 37 tube or rod bundles to 13.21, 29.95 and 53.01 million, respectively. The smallest element volume in the prism layers decreased for 5.2×10^3 mm^3 in the coarse mesh grid to 10^3 mm^3 in the fine mesh grid, while the average element volume in the bulk flow for both grids is the same at 0.19 mm^3 (Table 6.2). In the finer mesh grid (Fig. 6.7c), the thickness of the first of the prism layers decreased from 9×10^3 mm (in the fine mesh) to 10^3 mm (Table 6.2). The total number of elements in the finer mesh gird is 13.21, 29.95, 53.01, and 74.07 million in the computational domain of a 1/6 the volume of the 7, 19, 37 and 61 rod or tube bundles, respectively (Table 6.2).

The y+ parameter, which is a dimensionless ratio of the turbulence-to-laminar influence in the mesh grid elements near the solid surfaces, helps assess the quality of the mesh grid refinement in the CFD analyses (Salim and Cheah, 2009). In the finer mesh, the y+ in the CFD analyses of the 7, 19, 37 and 61 rod / tube bundles is < 1, for $10^2 < Re_{in} < 10^6$. Such low y+ suggests that the friction pressure losses near the solid boundaries are within the acceptable margins. The computation times for convergence with the fine and finer mesh grids are 84% and 85% longer than with the coarse mesh grid. The actual computation time, however, strongly depends on the number of tubes or rods in the bundle. For instance, the computation time with the finer mesh grid for the 19, 37, and 61 rod or tube bundles is 2.26, 4.01, and 5.6 times that for the 7 rod bundle, respectively, at the same Re_{in} and P/D = 1.2.

Table 6.2 lists the calculated values of the Grid Convergence Index (GCI) for calculating the friction factor in the hexagonal bundles with 7, 19, and 37 rods, in the laminar ($Re_{in} < 10^3$), transition ($10^3 < Re_{in} < 10^4$, and turbulent regions ($Re_{in} > 10^4$). The GCI, estimated for the performed CFD calculations with two or more mesh grid refinements, represents the discretization error due to the mesh grid and time step refinement (Roache 1994). The GCI is calculated based on the relative difference in the values of the friction factor determined, from the best fit of the experimental data (Rehme, 1972) and the present CFD analyses results with different numerical mesh refinements (Table 6.2 and Fig. 6.7), using the methodology suggested by Roaches (1994).

The calculated GCI values for the coarse, fine, and finer mesh grids are compared in Table 6.2 in the laminar ($Re_{in} < 10^3$), transition ($10^3 < Re_{in} < 10^4$) and turbulent ($Re_{in} > 10^4$) flow regions in rod or tube bundles with flat walls. The GCIs of the CFD results for the 7 rod or tube bundle with the coarse mesh grid are <4% in the laminar region, compared to ~ 38% in the turbulent region, suggesting the need for further refinement of the numerical mesh grid. With the fine mesh grid, the GCI for the 7 rod bundle is < 3% in the laminar and transition flow regions and <27% in the turbulent region. However, for the 19 and 37 rod bundles, the GCI in the transition flow region is <15%. For the results with the finer mesh grid, the GCI is < 1.4% for all flow regions in the 7, 19 and 37 rod or tube bundles. Such low GCI suggest that no further refinement of the implemented numerical grid is needed. Therefore, the CFD results presented in the reminder of this paper are obtained using the finer mesh grid (Fig. 6.7c, and Table 6.2).

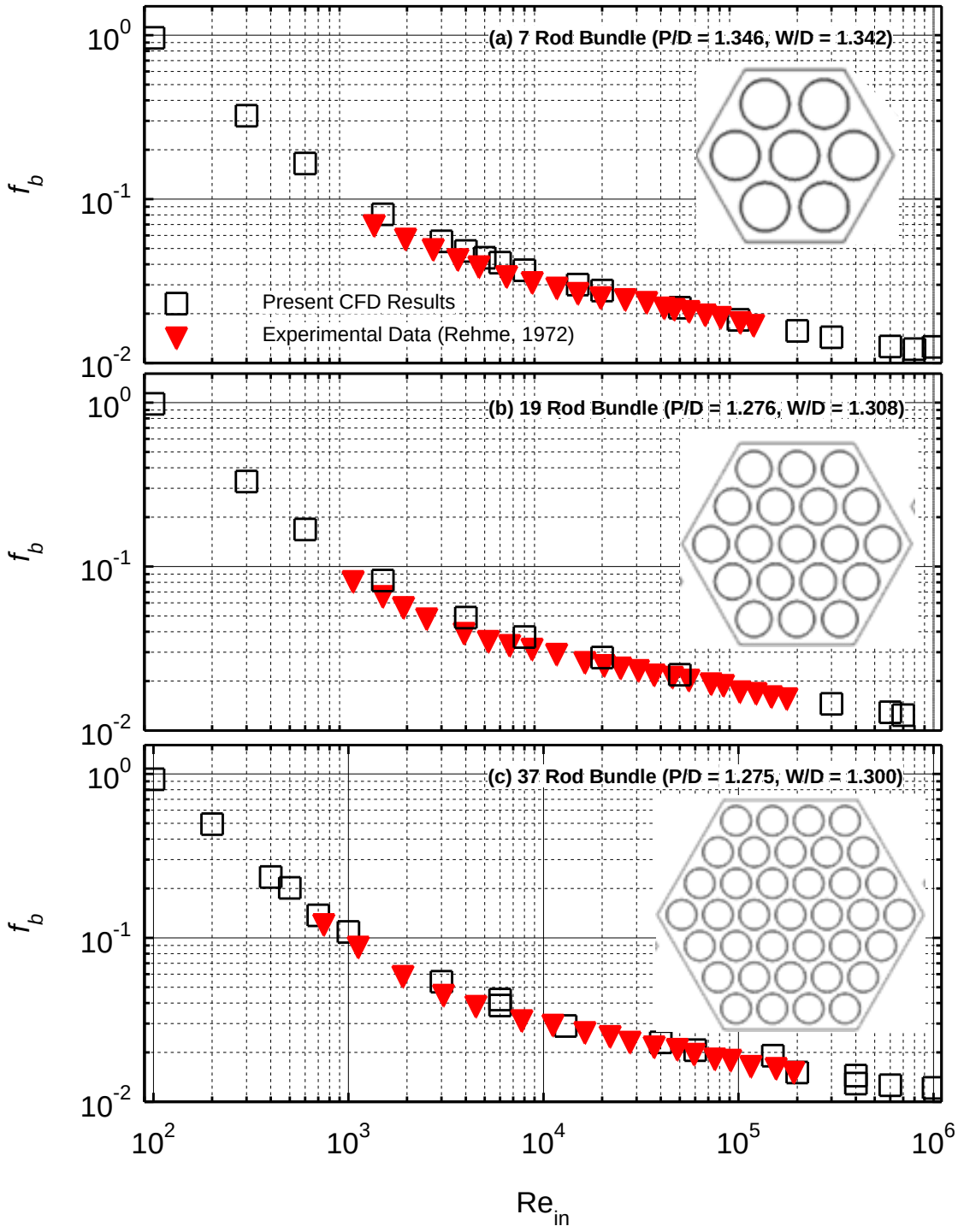

Fig. 6.8. Comparison of the CFD results of the friction factor using the finer mesh grid to the reported experimental data.

6.6. Developed Correlation for Friction Factor for Hexagonal Bundle

The regression for the friction factor data in the laminar flow region ($Re_{in} \leq 10^3$) includes a total of 183 data points. These include 46 reported experimental data points (Rehme, 1972) and as many as 137 presents CFD analyses data points. The data points of the friction factor in the turbulence flow region ($Re_{in} > 10^4$) totals 788, which includes 158 CFD data points and the 630 experimental data points. The friction factor data in the transition flow regime ($10^3 < Re_{in} < 10^4$) totals 453 data points, which include 373 experimental points and 80 CFD analyses points. The developed friction factor correlation in the present work is continuous among the three flow regions of laminar ($Re_{in} < 10^3$), transition ($10^3 < Re_{in} < 10^4$), and turbulent ($Re_{in} > 10^4$).

The experimental data and the present numerical results presented in Figs. 6.8, also show that the bundle frictions factor, f_b, decreases smoothly with increased Re_{in}. Thus, it is desirable to develop a continuous correlation, based on the best fit of the compiled numerical and experimental database in the laminar, transition, and turbulent flow regions. This correlation would have the following form:

$$f_b = [f_l^m + f_t^m]^{1/m}. \tag{6.4}$$

In this expression, the laminar flow friction factor, f_l, and the turbulent flow friction factor, f_t, are given as:

$$f_l = A/Re_{in}, \tag{6.5a}$$

$$f_t = B \,/\, Re_{in}^n \,. \tag{6.5b}$$

In these expressions, the coefficients "A" and "B" are functions of the P/D ratio and the number of the bare rods or tubes, N, in the hexagonal bundles with flat walls. These coefficients as well as the exponents "m" in Eq. (6.4) and "n" in Eq. (6.5b) are determined from the best fit of the compiled database of the present numerical results and the reported experimental data by Rehme (1972) in Table 6.1.

6.6.1. Friction Factor Correlation for Laminar Flow

As shown in Fig. 6.9a, the coefficient, A, of the friction factor for laminar flow ($Re_{in} < 10^3$), in hexagonal bundles with flat walls (Eq. 6.5a), increases almost exponentially

with increased P/D. It also increases as the number, N, of the bare tubes or rods in the hexagonal bundles increases. It is lowest for the bundle of 7 rods or tubes and highest for the bundle with 331 rods or tubes. The dashed curve of the laminar friction factor for the central subchannel in the bundles (Fig. 6.1a) is the upper limit for very large bundles. This is because the equivalent hydraulic diameter, De, for large bundles approaches that of the central subchannel, and the effect of the walls on the friction pressure losses practically diminishes (Fig. 6.2 and Eqs. 6.1a, 6.1b).

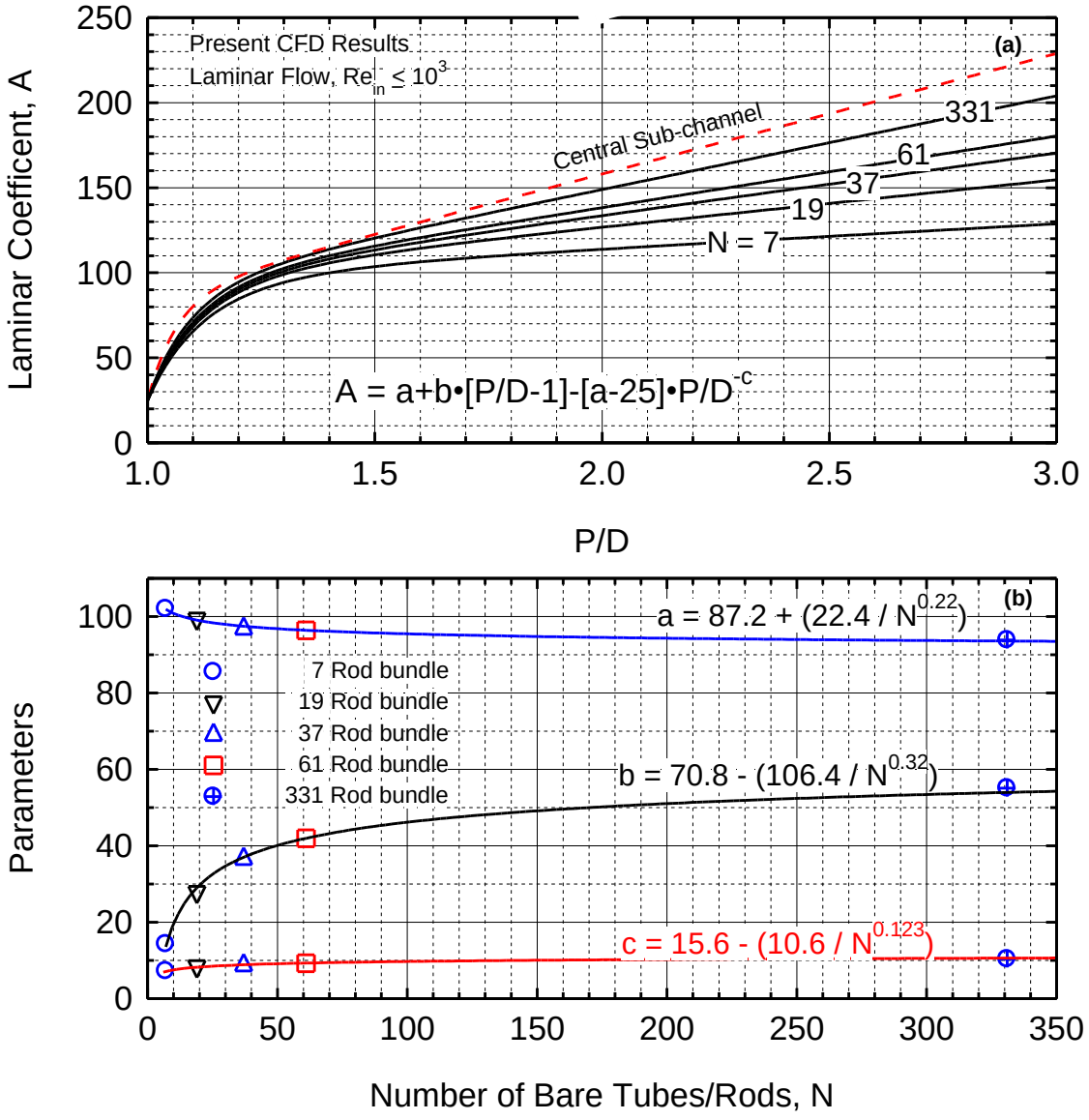

Fig. 6.9. Coefficient and parameters of the friction factor for laminar flow in hexagonal bundles with flat walls (Eqs. 6.5a and 6.6).

The values for the parameter "A", in Fig. 6.9a are correlated in terms of P/D in the bundle, as:

$$A = a + b\left(\frac{P}{D} - 1\right) - \left[(a - 25)/\left(\frac{P}{D}\right)^{c}\right] \quad (6.6a)$$

In this expression, the parameters "a", "b", and "c", expressed in terms of the number of rods or tubes in the bundle, N, are based on the best fit of the present CFD numerical results (Fig. 6.8b), as:

$$a = 87.2 + (22.4\ /N^{0.22}), \quad (6.6b)$$

$$b = 70.8 - (106.4\ /N^{0.32}), \quad (6.6c)$$

$$c = 15.6 - (10.6\ /N^{0.123}). \quad (6.6d)$$

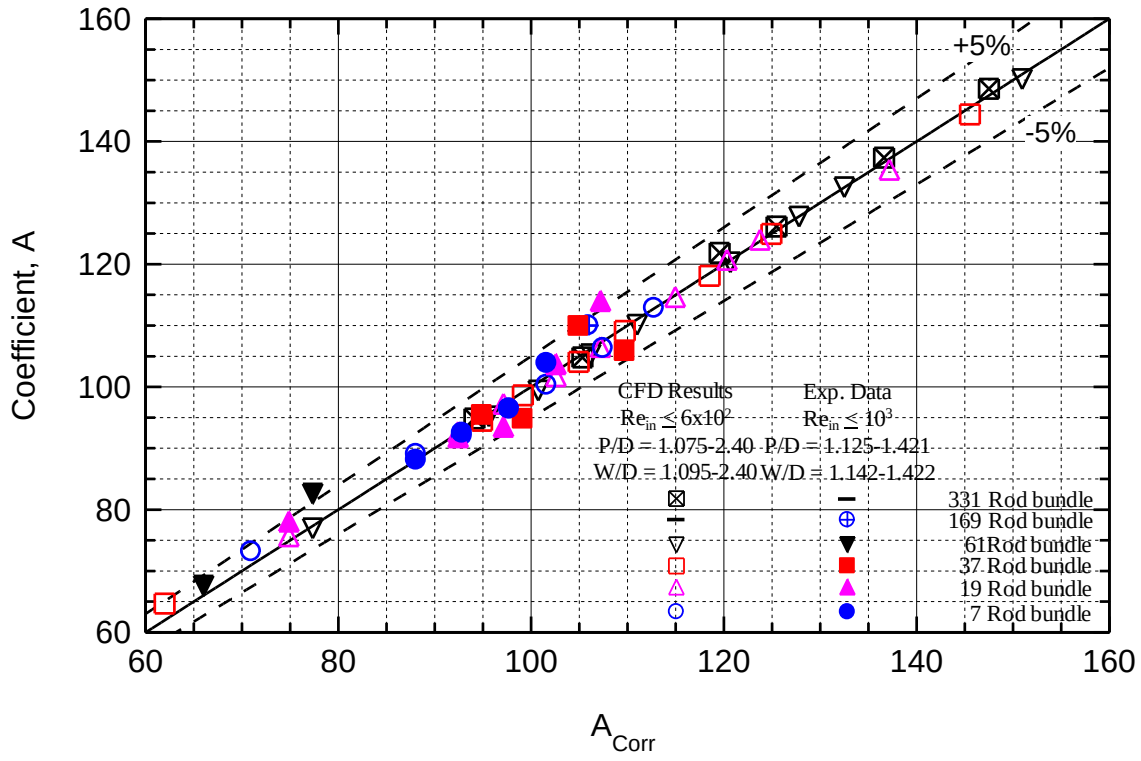

Fig. 6.10. Comparison of developed correlation for the coefficient "A" (Eq. 6.6a), with the compiled database of present CFD and reported experimental data for laminar flow in rod bundles.

These expressions (Eqs. 6.6b –6. 6d), are in excellent agreement with the reported experimental data (Rehme, 1972) and the present CFD analyses results for a wide range of bundle sizes (Fig. 6.9). When these parameters are substituted into Eq.(6.6a), the coefficient "A", expressed in terms of P/D and N in the bundles, is used in Eq. (6.5a) to calculate the friction factor for laminar flow, f_l, in terms of Re_{in}, P/D, and N. Fig. 6.10 shows that the present expression for the parameter "A" (Eq. 6.6), is in excellent agreement, to within $\pm$ 5%, of the compiled database of CFD analyses results and reported experimental data by Rehme (1972), in Table 6.1, for wide ranges of bundle sizes, P/D. W/D, and Re_{in}.

6.6.2. Friction Factor Correlation for Turbulent Flow

Figure 6.11 shows that the coefficient "B" (Eq. 6.5b) ($Re_{in} > 10^4$) in the turbulent flow friction factor, f_t, depends on P/D, but is practically independent of the number of the bare tubes or rods, N, in the hexagonal bundles. The coefficient "B" increases rapidly with increased P/D, from 1.0 to 1.4, but slowly with increased P/D >1.4. The values of this coefficient in the compiled database, of the present CFD numerical results and the reported experimental data (Rehme, 1972) for different size bundles and P/D values are correlated, as:

$$B = 0.186 + 0.00047\,[(P/D) - 1] - [0.06\,/(P/D)^{18.2}]. \qquad (6.7)$$

This correlation is in excellent agreement with the results of the present CFD analyses results (to within $\pm$2%) and the reported experimental data (to within $\pm$9%) for turbulent flow in hexagonal bundles with flat walls (Table 6.1, Fig. 6.11). This data is for P/D = 1.025 – 2.4 and bundle sizes of 7 – 331 rods or tubes. The coefficient "B" equals 0.126 for P/D = 1.0, increases rapidly to 0.1812 at P/D = 1.2 and levels off at 0.186 for P/D > 1.8 (Figs. 6.11 and 6.12b).

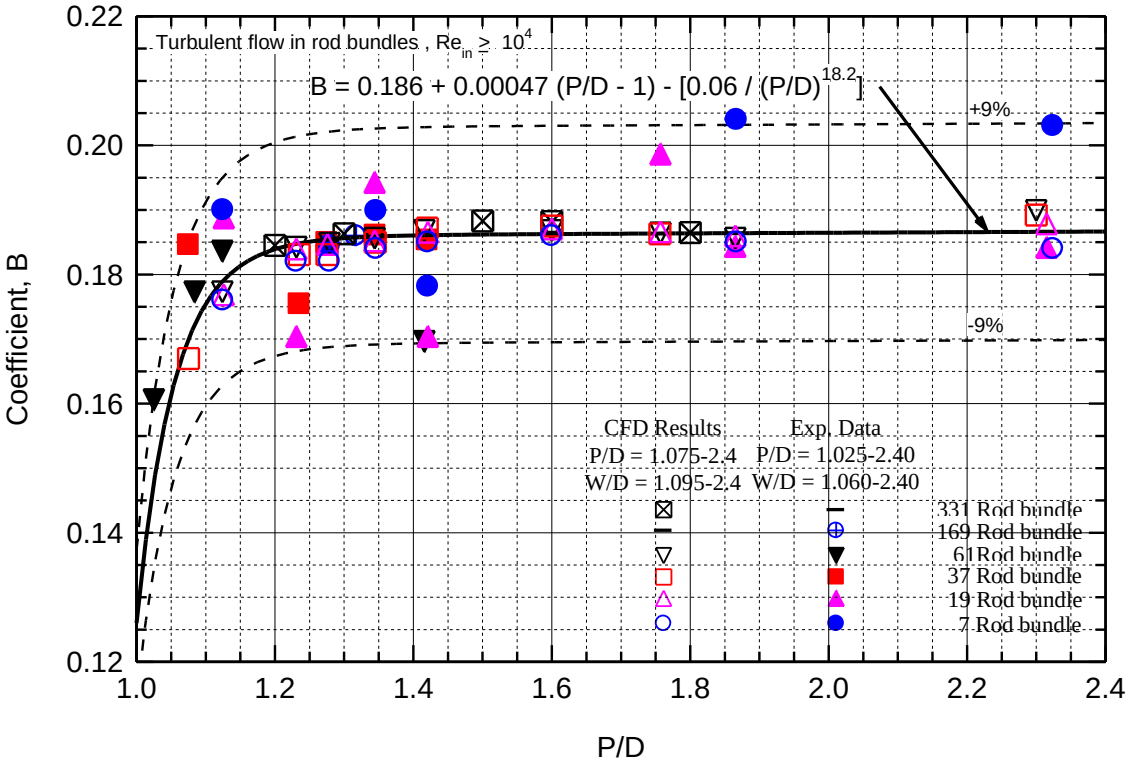

Fig. 6.11. Comparison of the developed correlation for the parameter "B" (Eq. 6.7) of the friction factor, with compiled CFD results and experimental data for turbulent flow in rod bundle.

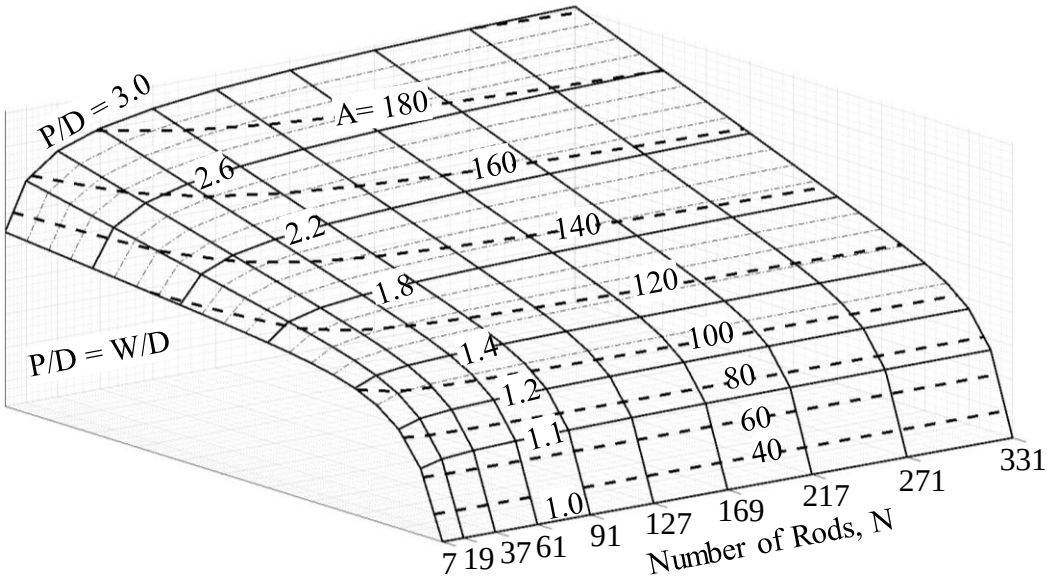

(a) Friction factor parameter "A" for laminar flow in hexagonal bundle (Eq. 6.6a).

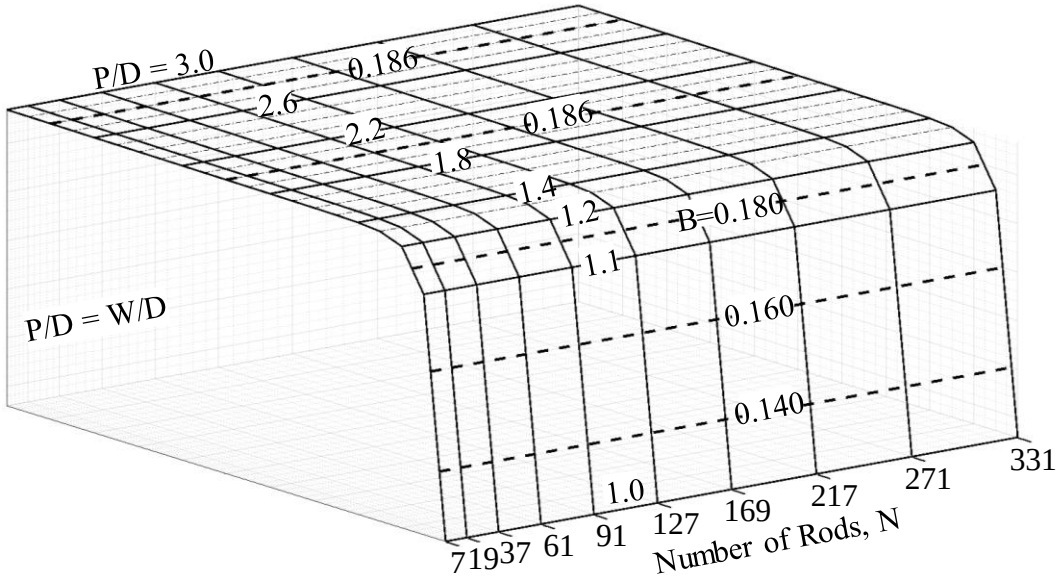

(b) Friction factor parameter "B" for turbulent flow in hexagonal bundle (Eq. 6.7).

Fig. 6.12. Calculated surfaces of the friction factor parameters for laminar (a) and turbulent (b) flows in hexagonal bundles with flat walls.

Figures 6.12a and 6.12b present surfaces of the friction factor coefficients "A' and "B" (Eqs. 6.6a and 6.7) for laminar and turbulent flows, respectively. These surfaces give the values of these coefficients and display their dependence on P/D and the number of bare tubes or rods, N, in the bundles. While the coefficient "A" of the friction factor for

laminar flow, f_l (Eq. 6.5a and Fig. 6.12a), increases with increased N, the coefficient "B" of friction factor for turbulent flow, f_t, (Eq. 6.5b) is practically independent of N (Fig. 6.12b). The values of these coefficients are quite different, but both increase with increased P/D. For large size bundles (N > 169), the coefficient "A" for the laminar flow friction factor increases very little with increasing N (Fig. 6.12a). The Re_{in} exponent "n" in equation (6.5b), of the friction factor for turbulent flow, f_t, is determined from the best fit of the results of the present CFD analyses and the reported experimental data by Rehme (1972) for flat walls hexagonal bundles of 7, 19, 37, and 61 bare tubes or rods, and wide ranges of P/D and W/D values (Figs. 6.1a and 6.13).

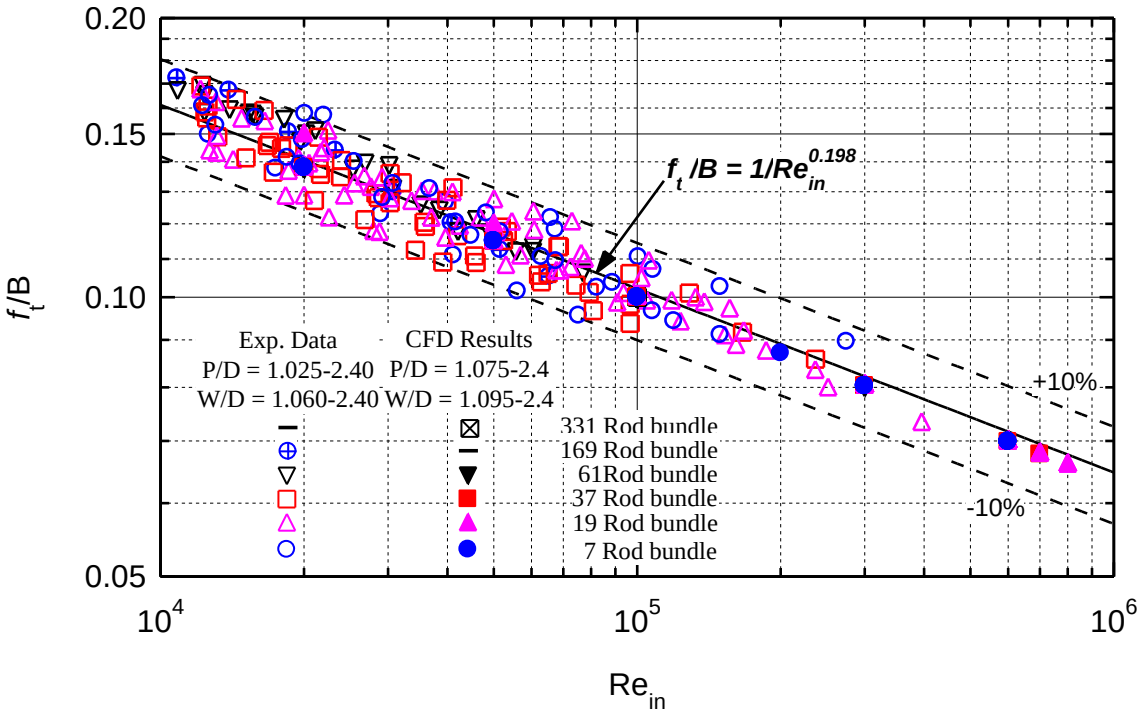

Fig. 6.13. Re_{in} exponent for the friction factor for turbulent flow in flat walls hexagonal bundles of bare tubes (Eq. 6.8).

The values of the parameter "B" and the exponent "n" of the friction factor for turbulent flow in Equation (6.5b) are determined simultaneously. The obtained values are consistent with both the experimental and CFD data of the friction factor for different size bundle (7, 19, 37, 169, and 331 rods) with different P/D (1.025 to 2.40) values (Fig. 6.13). The determined values (Fig. 6.13), is n = 0.198 $\pm$ 0.022. The obtained values of the parameter "B" are given by Equation (6.7), as function of P/D and the number of tubes

rods, N in the hexagonal bundles. Therefore, the correlation of the friction factor for turbulent flow, f_t (Eq. 6.5b), can be written, as:

$$f_t = B \,/\, Re_{in}^{0.198}. \tag{6.8}$$

6.6.3. Continuous Friction Correlation

A continuous correlation of the friction factor in hexagonal bundles of bare tubes or rods is obtained, by substituting the expressions in equations (6.5a), (6.6), (6.7), and (6.8), as well as the value of the exponent "m", determined for best fit of the compiled numerical and experimental database in the transition flow region, into Eq. (6.4). this gives the following continuous correlation of the friction factor, as:

$$f_b = \left[\left(\frac{A}{Re_{in}} \right)^2 + \left(\frac{B}{Re_{in}^{0.198}} \right)^2 \right]^{0.5} \tag{6.9}$$

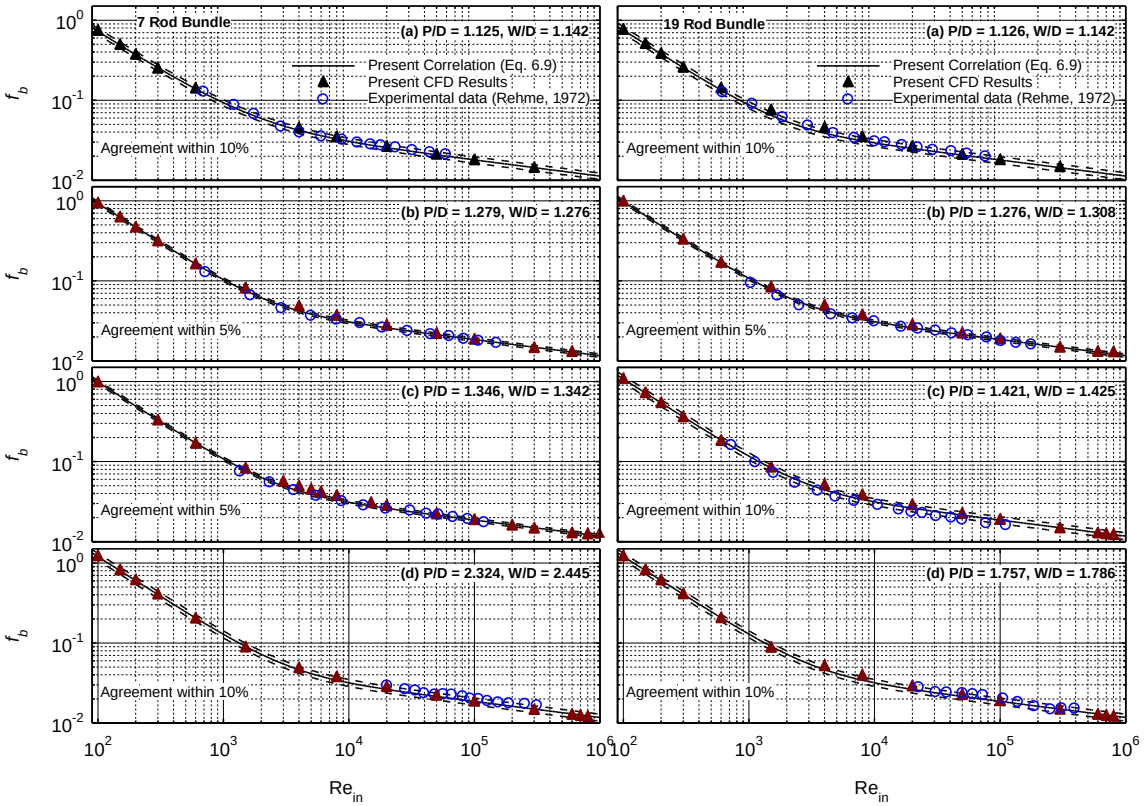

Fig. 6.14. Comparison of the present friction factor correlation (Eq. 6.9) with compiled database for 7 and 19 rods or tubes bundles with flat walls (Fig. 6.1a).

This correlation is in good agreement, to within ± 10%, with the compiled database of the present numerical results and the experimental data (Rehme, 1972) of the friction factor in the laminar, transition and turbulent flow in hexagonal bundles with flat walls, and P/W =1.0. (Figs. 6.14, 6.15).

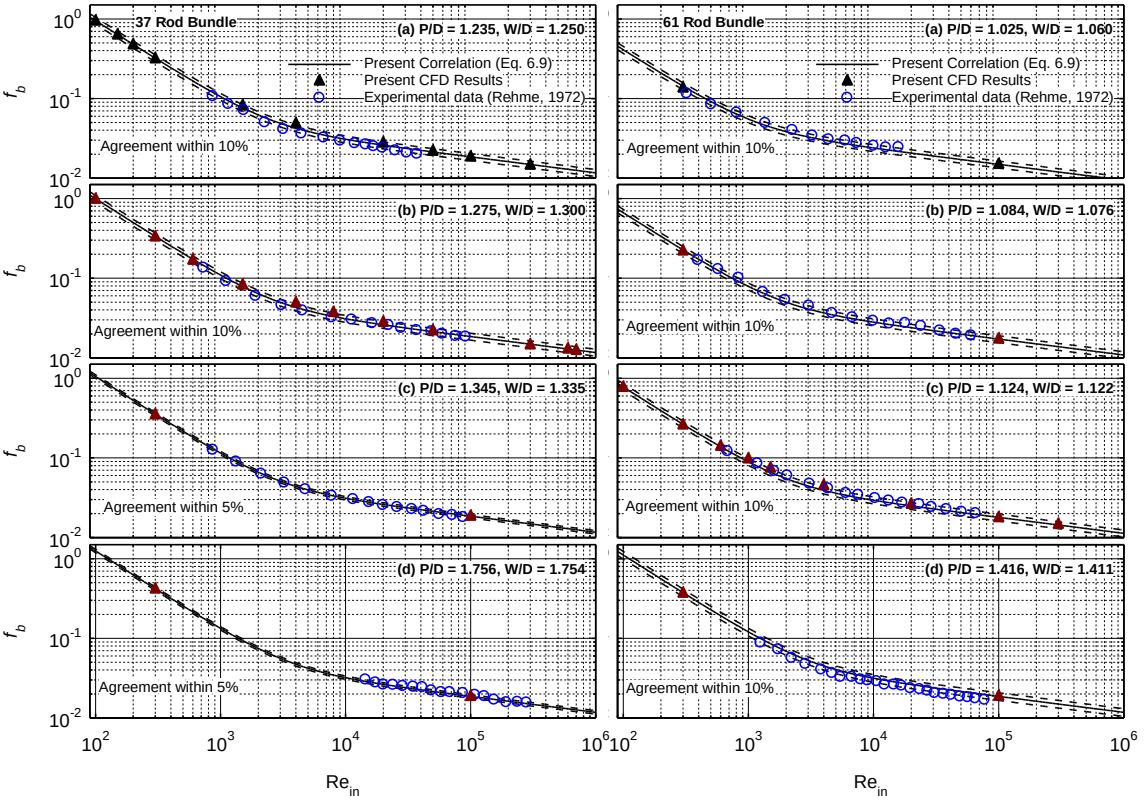

Fig. 6.15. Comparison of present friction factor correlation with compiled database for 37- and 61 rod bundles with flat walls.

Figure 6.14 compares the present friction factor correlation (Eq. 6.9), for select values of P/D, to the compiled database for bundles of 7 and 19 bare tubes or rod bundles. Fig. 6.15 provides similar comparisons of the friction factor for 37 and 61 rod bundles. The results in these figures confirm the good agreement between the present correlation (Eq.6.9) and the compiled database, to within ±5% and ±10%, respectively. These good comparisons confirm the effectiveness of the developed continuous friction factor correlation (Eq. 6.9). It spans a wide range of Re_{in} and is applicable to laminar ($Re_{in} < 10^3$), transition ($10^3 < Re_{in} < 10^4$), and turbulent ($Re_{in} > 10^4$) flows.

Figures 6.14 and 6.15 also show that the present CFD results effectively augment the reported experimental data by Rehme (1972), and fill the voids in the experimental data in the laminar flow region. In summary, the developed continuous correlation of the friction factor for flat walls hexagonal bundles of bare tubes or rods is based on a thorough and systematic approach and credible CFD and experimental database. This correlation is a valuable tool for the design of liquid metals cooled small modular nuclear reactors, employing hexagon bundles of bare tubes or rods, and of compact heat exchanges.

The present CFD results of the friction factor in hexagonal bundles with flat walls are calculated using the RANS SST k-ω turbulence model. They are in good agreement with the reported experimental data by Rehme (1972). Depending on the flow region, the bundle size, and the P/D values, the present CFD results are within 5% of the reported experimental results in the laminar flow region and within 10% of the experimental data in the transition and the turbulence flow regions (Figs. 6.14 and 6.15). The obtained CFD results of the friction factor using the RANS model in the laminar, transition and turbulent flow regimes are compared in Fig. 6.16 to the reported experimental values by Rehme (1972), for a wide range of bundle sizes and P/D values.

The insert in Fig. 6.16, compares the CFD results obtained using both the RANS turbulence model and the Detached Eddy Simulation (DES) model with gamma transition versus the reported experimental results for 7 and 19 rod bundles. The results in the insert in Figure 6.16 confirm that using the RANS or the DES turbulence model in the present CFD analyses gives very close and consistent values of the friction factor. These values are in good agreement with the reported experiment data (Rehme, 1972). The simulations with the DES model used a time step of 10^{-4} sec and the same numerical meshing used in the simulation using the SST k- ω turbulence model. The results of the two turbulence models in the laminar and the transition region are almost identical and within $\pm$10% of the experimental values.

The comparison of the CFD results and the reported experimental data of the friction factor in hexagonal bundle with flat walls (Rehme, 1972) Fig. 6.16 shows that the entire CFD results are within $\pm$10% of the reported experimental data. Considering the large number of the experimental data points and the different bundle sizes and P/D values, as

well as the measurements uncertainties in the experiments, this is an excellent comparison and verification of the present CFD results. The results in the insert in Fig. 6.16 also confirms the applicability of the RANS turbulence model in the present CFD analyses, in conjunction of the implemented numerical grid, for accurately calculating the pressure losses and the friction factor in all flow regimes in the hexagonal rod bundles with flat walls.

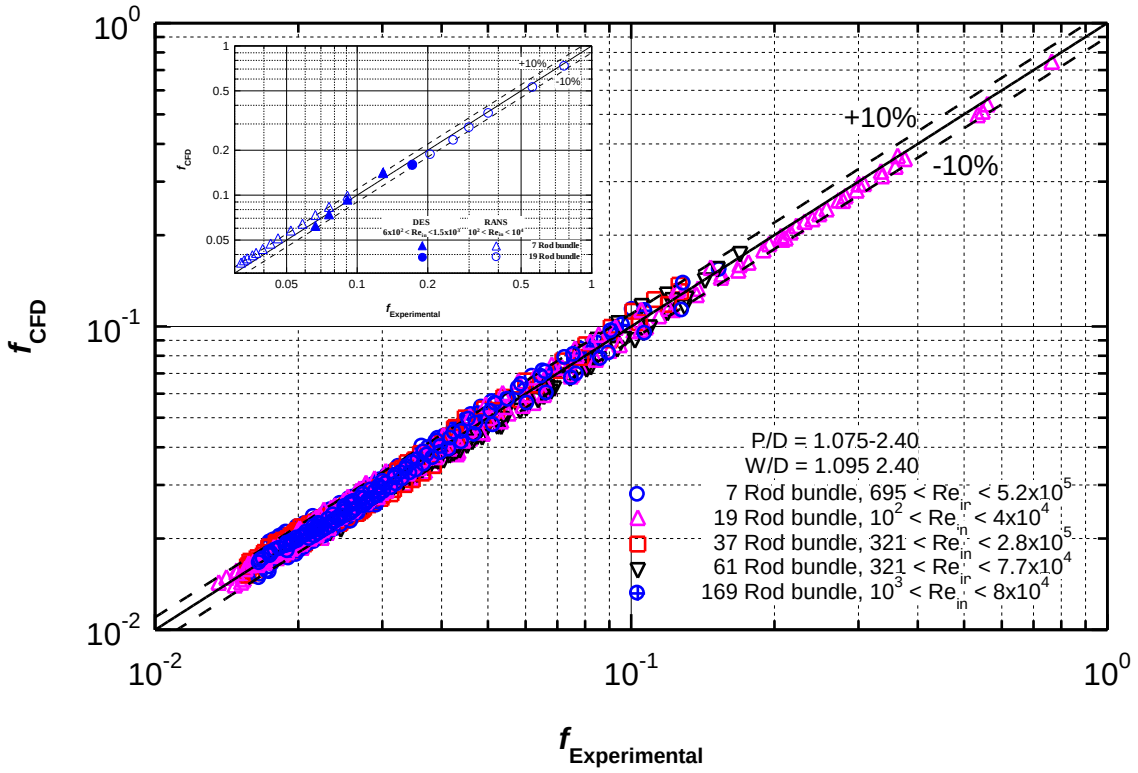

Fig. 6.16. Verification of present CFD analyses results with RANS and DES models using experimental data (Rehme 1972) of the friction factor in hexagonal rod bundles with flat walls.

6.7. CFD Analyses Results for Bundle with Scalloped Walls

This section compares the results of the performed CFD analyses of the friction factor for hexagonal bundles of 19 and 37 bare tubes and with scalloped walls (Fig. 6.1b) to the developed friction correlation (Eq. 6.9) for flat wall bundles (Fig. 6.1a). The 23.7 mm diameter bare tubes or rods in the scalloped wall bundles are arranged in a triangular lattice with P/D =1.2. The setup in the analyses is similar to that used for the flat wall

bundles (Fig. 6.6), except that the test section is longer (L_b = 1.10 m). The 250 mm long entrance and exit lengths ensure that the flow in the test section would be hydrodynamically fully developed, and the inlet and exit flow mixing are negligible to affect the pressure losses in the test section.

The CFD analyses of the pressure losses in the scalloped wall bundles (Fig. 6.1b) with 19 and 37 bare rods are performed for isothermal sodium flow at 500 and 800 K, as well as for water and air flows 295 K. The analyses results cover a wide range of Re_{in} (10^2 – 10^6) that spans all flow regions (laminar, transition, and turbulent). The liquid sodium temperatures used in the present CFD analyses are higher than its melting point at atmospheric pressure of ~ 371 K (Bomelburg et al., 1972; Thermal Fluids Central, 2016). The present CFD analyses of the pressure losses in the hexagonal bundles with scalloped walls used a finer mesh grid (Fig. 6.16), similar to that used in the analyses of the flat wall bundles (Figs. 6.1a and 6.7). This grid has been shown to be best for the convergence and the accuracy of the results (Table 6.2 and Fig. 6.8).

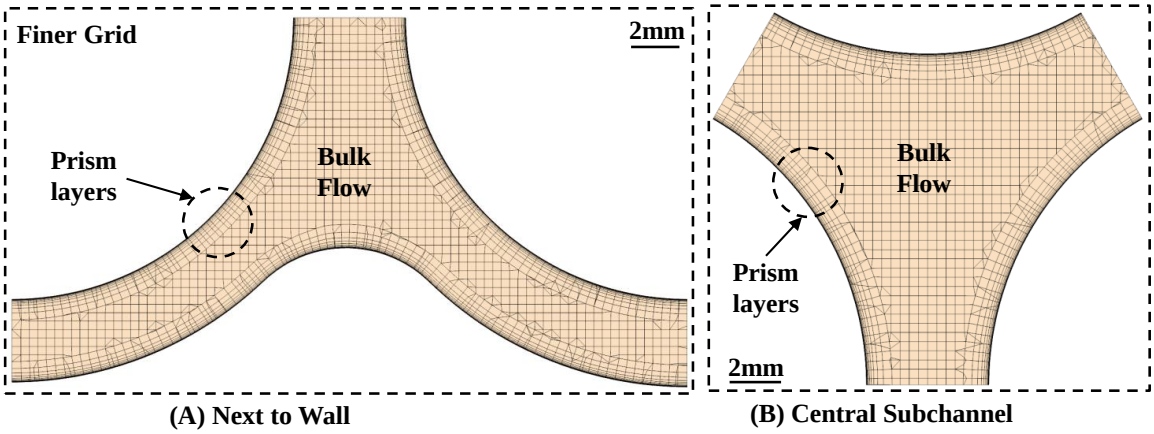

Fig. 6.17. The finer numerical mesh grid used in the present CFD analyses of pressure losses in 19 and 37 rod hexagonal bundles with scalloped walls.

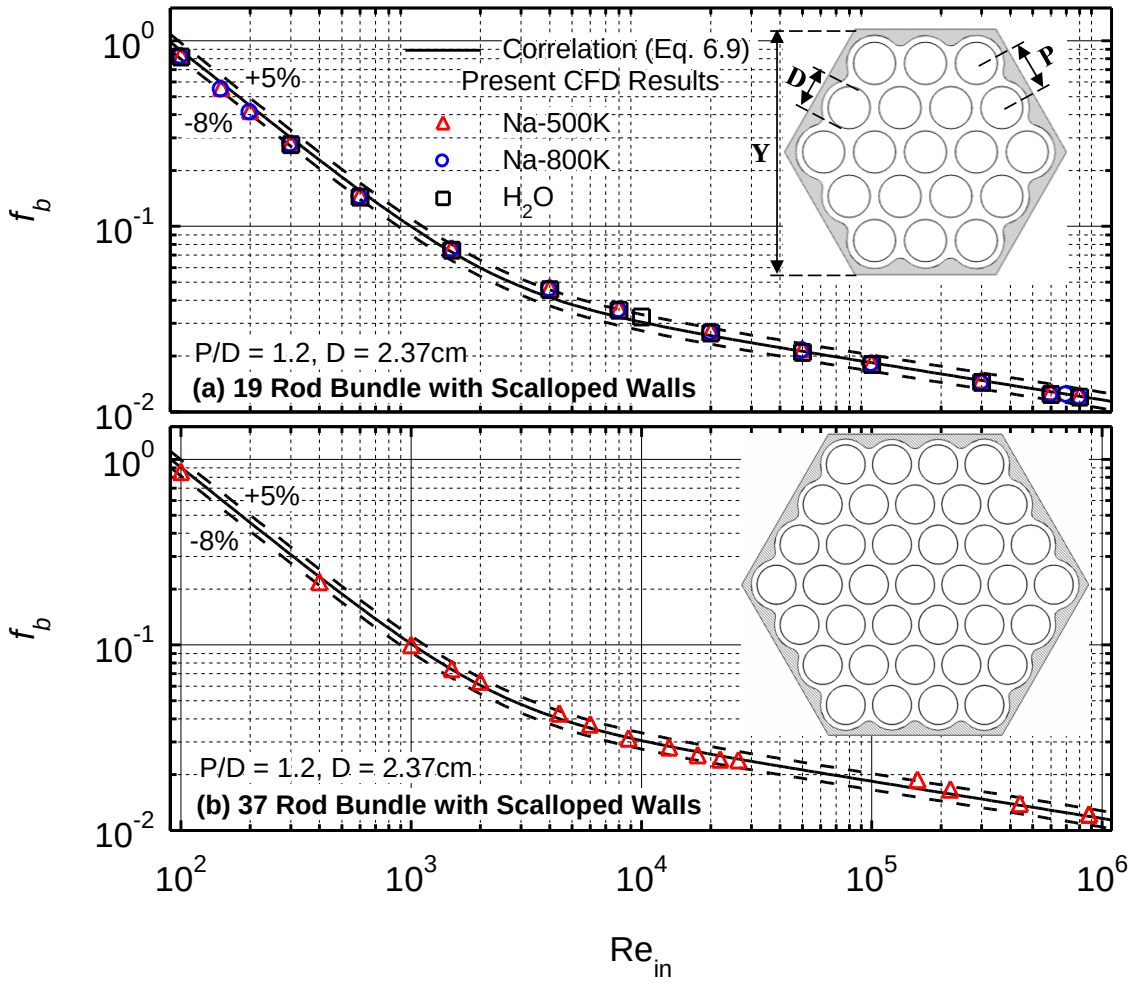

Fig. 6.18. Comparisons of the present CFD analyses results of the friction factor, for different liquids, in scalloped wall bundles to the developed correlation for flat wall bundles (Eq. 6.9).

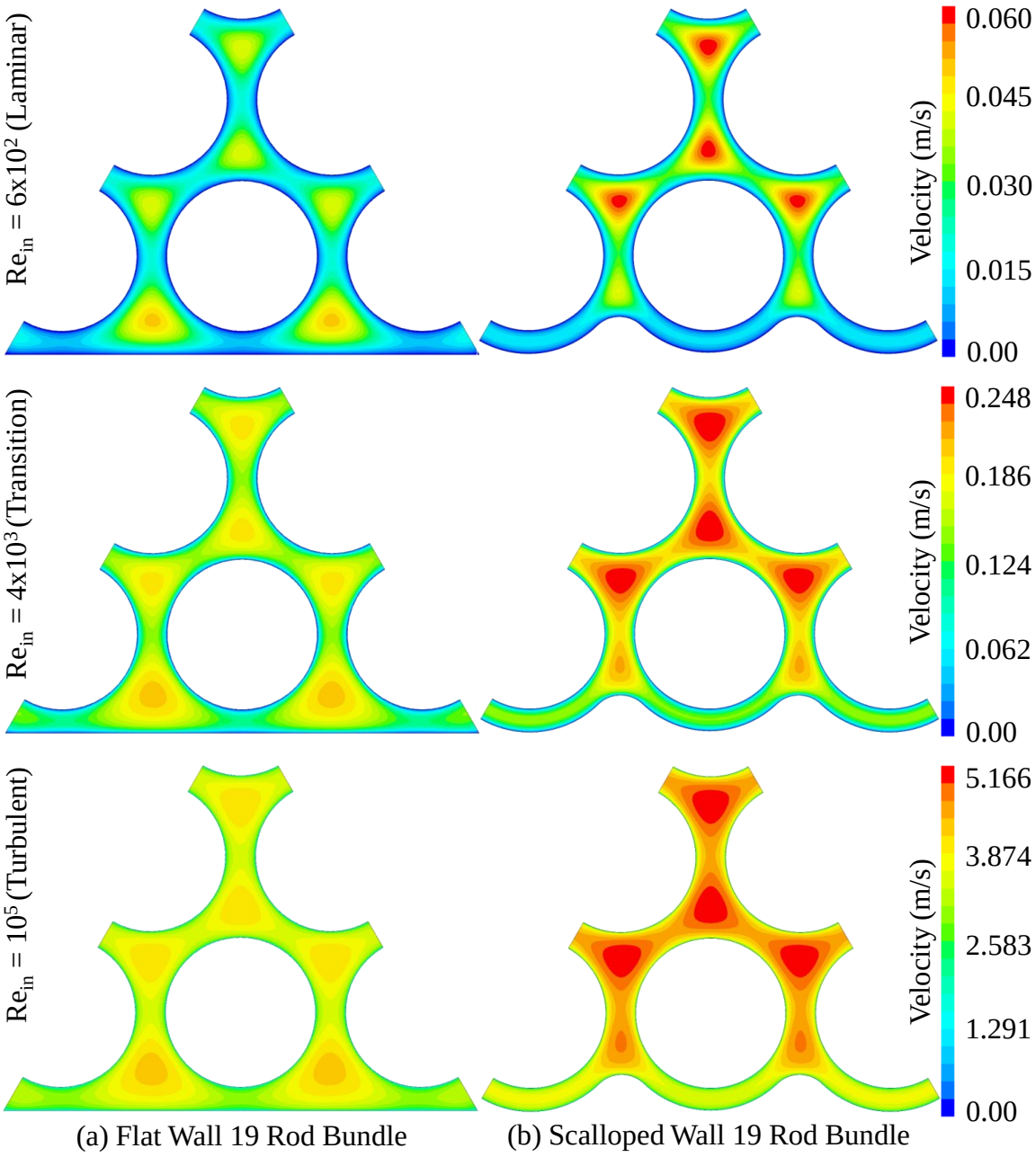

Fig. 6.19. Comparisons of the flow fields in 19 and 37 rod bundles with flat and scalloped walls at the same values of Re_{in} and axial location of 0.5 L_b.

The obtained results of the friction factor in the 19 and 37 rod bundles with scalloped walls are compared in Figs. 6.18a,b to the developed friction factor correlation for flat wall bundles (Eq. 6.9). The results confirm that this continuous correlation can also be

used to accurately predict the friction factor for isothermal flows of liquid metals, water and air flows in the hexagonal bundles with scalloped walls (Fig.6.1b). The correlation in Eq. (6.9) is in good agreement with the present CFD results of the friction factor for the scalloped walls hexagonal bundles. They are within +5% to - 8% of the correlation (Eq. 6.9) in the laminar ($Re_{in} < 10^3$), transition ($10^3 < Re_{in} < 10^4$) and turbulent ($Re_{in} > 10^4$) flow regions (Fig. 6.18).

The flat and the scalloped walls of the hexagonal bundles (Figs. 6.1a, b), affect the flow distribution near the walls and in the central subchannels. Fig. 6.19a compares the calculated velocity fields for laminar flow at $Re_{in} = 6x10^2$ in a 19 rod bundles with flat and with scalloped walls, at the axial plane that is 500 mm from the entrance of the test section (Fig. 6.6). The images of the velocity field in this figure confirm that in the bundle with scalloped wall, the bypass flow next the wall decreases, while that in the subchannels the interior of the bundle increases. This is a desirable spatial velocity distribution for enhancing the thermal-hydraulics in the core of the VSLLIM nuclear reactor.

The scalloped walls direct more of the inlet flow to the interior subchannels, at the expense of decreasing the flow in the subcahannels next to the wall. This effect increases with increased Re_{in}, in the transition and the turbulent flow regions (Fig, 6.19a). It would enhance the heat removal from the nuclear fuel rods and decrease the maximum temperature of the UN pellets in the rods during nominal reactor operation and after shutdown (El-Genk at al., 2017; Shriener and El-Genk, 2018).

Conversely, in the bundle with flat walls, there is relatively large bypass flow in the subchannels next to the walls, at the expenses of reducing the flow in the interior subchannels. Such non-uniform lateral flow distribution, which increase, with increased W/P (Figs. 6.1a), would affect the bundle friction factor thermal hydraulics (Fig. 6.19b).

6.8. Summary

Computational Fluid Dynamics (CFD) analyses investigated the effect of various geometrical (P/D and N) and operation (Re_{in}) parameters on the friction factor for laminar, transition and turbulent flows in flat wall hexagonal bundles of bare tubes or rods and P/W =1.0 and in bundles with scalloped walls. The obtained results for fully developed flows of water and liquid sodium are in good agreement with the reported

experimental data by Rehme (1972) for bundles with flat walls. The compiled database of the present numerical results and the reported experimental data is used to develop a continuous correlation of the friction factor that spans the laminar, transition and turbulent flow regions ($10^2 < Re_{in} < 4x10^5$). The developed correlations is applicable for bundles with P/D up to 3.0 and a wide range of the number of bare tubes or rods, N = 7 – 331.

The developed continuous correlation of the friction factor for flat wall bundles is in excellent agreement with the compiled database, to within +5% to - 10% and is valid for laminar ($Re_{in} < 10^3$), transition ($10^3 < Re_{in} < 10^4$), and turbulent ($Re_{in} > 10^4$) flows. This correlation is a useful tool for engineering design and calculation of pressure losses in hexagonal bundles of bare tubes and with either flat or scalloped walls.

The continuous friction factor correlation developed for flat wall a bundle is within +5% to - 8% of the CFD data generated for the scalloped walls bundles with 19 and 37 rods or tubes in all flow regions. The CFD analyses results show that the scalloped walled reduces the bypass flow next to the wall, while increasing the flow in the interior subchannels of the bundle. Higher flow in the inner subchannels enhances the thermal-hydraulics in the core of the VSLLIM reactor by removing more heat from the UN fuel rods, while reducing the fuel temperatures for the same Re_{in}. However, for bundles with flat walls the bypass flow next to the walls increases with increased W/P and would affect the bundle friction factor.

7. SUMMARY AND CONCLUSIONS

The performed research in this dissertation includes neutronics and CFD-thermal hydraulics analyses of the **V**ery-**S**mall, **L**ong-**LI**fe, and **M**odular (VSLLIM) nuclear reactor. It can provide 1.0 – 10 MW_{th} for electricity generation and process heat for industrial uses and/or district heating, for extended periods of time without refueling. The compact VSLLIM reactor can be fabricated, assembled, and sealed at the factory. The fully assembled reactor, together with a power conversion module, can be deployed on a portable platform for niche applications such as electricity generation for remote and isolated communities, island nations, and advanced military bases and outposts. Alternatively, the reactor power module could be transported by rail, barge or truck to a permanent site, where it would be installed below ground and mounted on seismic isolation bearings. At the end of life (EOL), the post-operation VSLLIM reactor is safely showdown and left onsite for a period of time until the external radiological dose rate decreases to a safe level for handling and transportation to the factory or a reprocessing facility. The removed VSLLIM reactor unit would then be replaced with a new unit loaded with fresh fuel for continued plant operation.

Neutronics analyses results show that the VSLLIM reactor with UN fuel enrichment of 13.76% is capable of achieving full-power operation life of ~92 FPY and 5.8 FPY at 1.0 and 10 MW_{th}, respectively. Results also show that the RC and ESS are each capable of shutting down the reactor with sufficient cold-clean reactivity shutdown margin. In addition, the negative temperature reactivity feedback in the VSLLIM core is also capable of shutting down the reactor with modest increases in the temperatures of the UN fuel and the in-vessel liquid sodium. The calculated neutron energy spectrum in the VSLLIM reactor core is hard, which helps for reduce the inventory of minor actinides in UN fuel during reactor operation. The UN fuel in the VSLLIM core experiences practically no swelling and fission gas release, because of its low operating temperatures, $\leq$ 812 K at 10 MW_{th} and the low average power density in the core ($\leq$ 23.47 MW_{th}/m^3).

After reactor shutdown, natural circulation of the in-vessel liquid sodium is maintained for removing the decay heat generated in the reactor core using the in-vessel Na-Na HEX. In case of a malfunction of the Na-Na HEX, decay power is removed by the LMHPs embedded in the primary vessel wall and by natural circulation of ambient air

along the outer surface of the reactor guard vessel wall. Results of the 3D-CFD and thermal-hydraulics analyses demonstrate that following an unlikely malfunction of the in-vessel Na-Na HEX, the decay heat generation in the reactor core can be safely removed by natural circulation of ambient air along the outer surface of the reactor guard vessel, with and without metal fins. The metal fins increase the rate of decay heat removal by ambient air by ~ 13.5% (from 244 kW_{th} to 277 kW_{th} immediately after shutdown). This decreases the time after shutdown from when the rate of decay heat generation in the reactor core drops below that removed by natural circulation of ambient air from 0.34 to 0.2 hr. Results show that reducing the width of the cold air intake duct by 50%, and without metal fins along the guard vessel wall, the rate of decay heat removal by natural circulation of ambient air decreases by 35% (from 244 kW_{th} to 155 kW_{th} immediately after shutdown). This extends the time for the average temperature of the in-vessel liquid sodium to cool down to 400 K from ~100 hr. (or > 4 days) to 346 hrs. (or > 2 weeks).

The calculated total pressure losses for natural circulation of the in-vessel liquid sodium in the VSLLIM reactor increase with increasing its thermal power. The pressure losses in the reactor core represent a large fraction of the total pressure losses for the natural circulation of in-vessel liquid sodium. To accurately estimate the pressure losses across the hexagonal bundles in reactor core, CFD analyses are performed to numerically determine the friction factor for laminar, transition and turbulent flows in bare tubes hexagonal bundles with flat and scalloped walls. Results of the 3D-CFD analyses for calculating the friction factor is validated using a large compiled experimental database. The comparison involving bundles with flat walls covers a wide range of geometrical parameters, namely the number of rods or tubes, diameter, P/D and flow Re_{in} ($10^2 < Re_{in} < 10^6$).

Results of the friction factor correlation for fully developed water and liquid sodium flows are in good agreement, to within +5% to -10%, with the reported experimental data by Rehme (1972) for bundles with flat walls. The correlation is valid for laminar ($Re_{in} < 10^3$), transition ($10^3 < Re_{in} < 10^4$), and turbulent ($Re_{in} > 10^4$) flows. The compiled database of 1049 experimental and 375 data points of the present CFD results are used to develop a continuous correlation of the friction factor that spans the laminar, transition and turbulent flow regions ($10^2 < Re_{in} < 4x10^5$). The developed correlations is applicable

to P/D up to 3.0 and for a wide range of the number of bare tubes or rods in the bundles, N = 7 – 331. This correlation of the friction factor is also within 5% - 8% to the CFD data generated for the scalloped walls bundles with 19 and 37 rods or tubes along all flow regions.

The developed friction factor correlation for hexagonal rod bundles with either flat or scalloped walls, is a useful tool for engineering design and calculation of pressure losses in hexagonal bundles of bare tubes with either flat or scalloped walls. In addition, CFD analyses are perform to examine the flow distribution in flat and scalloped walled hexagonal rod bundles. The analyses show the scalloped wall reduces bypass flow next to the wall, while increasing the flow in the interior subchannels of the bundle. Higher flow in the inner subchannels enhances thermal-hydraulics by removing more heat from the UN fuel rods, while reducing its maximum temperature.

8. REFERENCES

Acktar Advanced Coatings, 2019. https://www.acktar.com/products-services/high-emissivity-materials/ (Accessed March 2019).

Anantatmula, R.P., Berhm, W.F., 1985. Sodium Compatibility of HT-9 and Fe-9Cr-1Mo Steels, Technical Report # HEDL-SA-2801FP. Westinghouse Hanford Company, Hanford, Washington, USA.

Angelo JR, J., Buden, D., 1987. Space Nuclear Power. Orbit Book Company Inc., Malabar, FL, USA.

Arie, K., 2009. Development for Fast Reactor and Related Fuel Cycle in Toshiba. Proceedings International Congress on Advances in Nuclear Power Plants (ICAPP'09), Tokyo, Japan. May 10-14.

Babcock & Wilcox Nuclear Energy, Inc., 2011. Generation mPowerTM B&W. Charlotte, NC, USA, http://www.babcock.com/products/modular_nuclear/generation_mpower.html.

Barret, K., Bragg-Sitton, S., Galicki, D., 2012. Advanced LWR Nuclear Fuel Cladding System Development Trade-off Study. Technical Report # INL/EXT-12-27090, Idaho National Laboratory, Idaho Falls, ID, USA.

Bomelburg, H.J., Smith, C., Royden, H.N., Swanson, V.A., Thiele, A.W., Tuttle, R.J., 1972. Physical Properties Sodium-NaK Engineering Handbook, In: Foust, O.J. (Ed.), Gordon and Breach, Science Publishers, INC, New York, USA, vol. 1, pp. 1–167.

Brown, F.B., 2006. The MAKXSF Code with Doppler Broadening, Technical Report # LA-UR-06-7002. Los Alamos National, Los Alamos, NM, USA.

Brown, F.B., Kiedrowski, J.B., 2008. MCNP – A General Monte Carlo N-Particle Transport Code – Version 5, Technical Report # LA-UR-03e1987, vol. I. Los Alamos National Laboratory, Los Alamos, New Mexico, USA.

Brown, N. R., Betzler, B. R., Carbajo, J. J., Wysocki, A. J., Greenwood, M. S., Gentry, C., Qualls, A. L., 2017. Preconceptual Design of a Fluoride High Temperature Salt-Cooled Engineering Demonstration Reactor: Core Design and Safety Analysis. Annals of Nuclear Energy 103, 49-59.

Brown, N.R., Todosow, M., 2014. Reactor Performance Screening of Accident Tolerant Fuel and Cladding Candidate Systems, Technical Report # BNL-107219- 2014-cp. Brookhaven National Laboratory, Long Island, NY, USA.

Carelli, M.D., Garrone, P., Locatelli, G., Mancini, M., Mycoff, C., Trucco, P., Ricotti, M. E., 2010. Economic Features of Integral, Modular, and Small-to-Medium Size Reactors. Progress in Nuclear Energy 52, 403–414.

Caro. M., 2012. Irradiation Embritlement in Alloy HT-9, Technical Report LA-UR-12-24334. Los Alamos National Laboratory, Los Alamos, NM, USA.

CD-ADAPCO, STAR-CCM+ Release 12.02, 2017.

Chadwick, M.B. et al., 2006. ENDF/B-VII.0: Next Generation Evaluated Nuclear Data Library for Nuclear Science and Technology. Nuclear Data Sheets 107, 2931– 3059.

Cheng, S.K., Todreas, N.E., 1986. Hydrodynamic Models and Correlation for Bare, and Wire Wrapped Hexagonal Rod Bundles – Bundle Friction Factor, Subchannel Friction Factors and Mixing Parameters. Nuclear Engineering and Design 92, 227–251.

Choi, S., Cho, J.H., Bae, M.H., Lim, J., Puspitarini, D., Jeun, J.H., Joo, H.-G., Hwang, I.S., 2011. PASCAR: Long Burning Small Modular Reactor Based on Natural Circulation. Nuclear Engineering Design 241, 1486-1499.

Chun, J.H., Lee, K.H., Chung, Y.J., 2013. Assessment and SMART Application of System Analysis Design Code, TASS/SMR-S for SBLOCA. Nuclear Engineering Design 254, 291–299.

Department of Defense, 2016. Task Force on Energy Systems for Forward/Remote Operating Bases. Technical Report AD1022571, Washington, D.C., USA.

Ding, M., Kloosterman, J.L., Kooijman, T., Linssen, R., 2011. Design of a U-Battery, Delft Technical University, Delft, Technical Report # PNR-131-2011-014, https://www.u-battery.com/_/uploads/AExecSummary.pdf

El-Genk M.S., 2008. Space reactor Power Systems With no Simple Point Failures. Nuclear Engineering Design 238, 2245-2255

El-Genk, M.S. and Schriener, T.M., 2018. Post-operation radiological source term and dose rate estimates for the Scalable LIquid Metal-cooled small Modular Reactor. Annals of Nuclear Energy 115, 442-458.

El-Genk, M.S. and Seo, J.T., 1988. Load Following and Reliability Studies of an Integrated SP-100 System. Journal Propulsion and Power 4, 152-156.

El-Genk, M.S. and Tournier, J.M., 2005. Review of Refractory Metal Alloy and Mechanically Alloyed Oxide Dispersion Strengthened Steels for Space Nuclear Power systems. Journal Nuclear Materials 340, 93-112

El-Genk, M.S., 1994. A Critical Review of Space and Nuclear Power and Propulsion 1984–1993. American Institute of Physics, New York, NY, USA.

El-Genk, M.S., and Tournier, J.M., 2009. Performance Analyses of VHTR Plants with Direct and Iindirect Closed Brayton Cycles. Journal of Progress in Nuclear Energy 51, 526-542.

El-Genk, M.S., L.M. Palomino, 2019, A Walk-Away Safe, Very Small, Long-LIfe, Modular (VSLLIM) Reactor for Portable and Stationary Power. Annals of Nuclear Energy 129, 181-198.

El-Genk, M.S., Palomino, L.M., 2014. SLIMM-Neutronic Analyses and Lifetime Estimates, Proceedings ICAPP'14, Paper 14232. American Nuclear Society, Charlotte, NC, USA.

El-Genk, M.S., Palomino, L.M., 2014. SLIMM-Scalable Liquid Metal Cooled Small Modular Reactor, Proceedings of ICAPP`14, Paper 14076. American Nuclear Society, Charlotte, NC, USA.

El-Genk, M.S., Palomino, L.M., 2015. SLIMM-scalable Liquid Metal Cooled Small Modular Reactor: Preliminary Design. Progress in Nuclear Energy 85, 56–70.

El-Genk, M.S., Palomino, L.M., Schriener, T.M., 2017. Low-enrichment and Long-life Scalable LIquid Metal cooled small Modular (SLIMM-1.2) Reactor. Nuclear Engineering and Design 315, 163–185.

El-Genk, M.S., Saber, H.H., 2003. High Efficiency Segmented Thermoelectric for Operation between 973 K and 300 K. Energy Conversion Management 44, 1069–1088.

El-Genk, M.S., Saber, H.H., Caillat, T., Sakamoto, J., 2006. Test Results and Performance Comparisons of Coated and Un-coated Skutterudite-based Segmented Unicouples. Energy Conversion Management 47, 174–200.

El-Genk, M.S., Tournier, J.M., 2003. Analysis of Small Nuclear Power Plants with Static Energy Conversion. Progress in Nuclear Energy 42, 283–310.

El-Genk, M.S., Tournier, J.-M., 2011. Uses of Liquid-Metal and Water Heat Pipes in Space Reactor Power Systems. Journal Frontier in Heat Pipes 2, 3002.

Engel, F., Markley, R., Bishop, A., 1979. Laminar, Transition, and Turbulent Parallel Flow Pressure Drop Across Wire-Wrap-Spaced Rod Bundles. Nuclear Science and Engineering 69, 290-296.

Fakory, M., Todreas, N.E., 1979. Experimental Investigation of Flow Resistance and Wall Shear Stress in the Snterior Subchannel of a Triangular Array of Parallel Rods, Transactions of the ASME. Journal of Fluids Engineering 101, 429–435.

Filippone, C. and Jordan, K.A., 2017. The Holos Reactor: A Distribution Generation with Transportable Subcritical Power Modules. Holos Generators, https://engrxiv.org/jzac9/.

Foust, O.J., 1972, Sodium-NaK Handbook, Vol. I, Gordon and Breach, New York, USA.

Gajapathy, R., Velusamy, K., Selvaraj, P., Chellapandi, P., Chetal, S., 2009. A Comparative CFD Investigation of Helical Wire-Wrapped 7, 19 and 37 Fuel Pin Bundles and Its Extendibility to 217 Pin Bundle. Nuclear Engineering and Design 239, 2279-2292.

General Atomics and Affiliated Companies, 2010. EM2TM Energy Multiplier Module, General Atomics, San Diego, CA, USA, http://www.ga.com/energy/em2/.

Goorley, T., 2014. MCNP6.1.1-Beta Release Notes, Technical Report # LA-UR-14-24680. Los Alamos National Laboratory, Los Alamos, New Mexico, USA.

Greene, S.R., Flanagan, G.F., Borole, A.P., 2008. Integration of Biorefineries and Nuclear Cogeneration Power Plants – A Preliminary Analysis, ORNL/TM-2008/102.

Guo, Z., Zhao, Y., Zhu, Y., Niu, F., Lu, D., 2018. Optimal Design of Supercritical CO_2 Power Cycle for Next Generation Nuclear Power Conversion Systems. Progress in Nuclear Energy 2018, 111-121.

Haskins, D.A., El-Genk, M.S., 2016. CFD Analyses and Correlation of Pressure Losses on the Shell-side of Concentric, Helically-Coiled Tubes Heat Exchanger. Journal of Nuclear Engineering Design 305, 531–546.

Haskins, D.A., El-Genk, M.S., 2017. Natural Circulation Thermal-Hydraulics Model and Analyses of ‘‘SLIMM” – A Small Modular Reactor. Annals of Nuclear Energy 101, 516-527.

Hayes, S.L., Thomas, J.K., Peddicord, K.L., 1990. Material Property Correlation for Uranium Mononitride IV. Thermodynamic properties, Journal of Nuclear Material 171, 300– 318.

He, Y., Li, Y., Wang, L., Sun, Y., Ahang, S., 2009. High Emissivity Coatings for High Temperature Application: Progress and Prospect. Journal Thin Solid Films 517, 5120–5129.

Hickman, B.S., Pryor, A.W., 1964. The Effect of Neutron Irradiation on Beryllium Oxide. Journal of Nuclear Materials 14, 96–110.

Hidayatullah, H., Susyadi, S., Subki, M.H., 2015. Design and Technology Development for Small Modular Reactor Safety Expectations, Prospect and Impediments of their Deployment. Progress in Nuclear Energy 79, 127-135.

Horie, H., Miyagi, K., Nakahara, K., Matsumiya, H., 2008. Safety Performance of the 4S Reactor on the ATWS Events – Statistical Estimation of Uncertainty. Progress in Nuclear Energy 50, 179–184.

Idaho National Laboratory, 2006, EBR-I Fact Sheet, 60-GA50269. Idaho, USA.

Ingersoll, D.T., 2009. Deliberately Small Reactor and the Second Nuclear Era. Progress in Nuclear Energy 51, 589-603.

Ingersoll, D.T., Houghton, Z.J., Bromm, R., Desportes, C., 2014. NuScale Small Modular Reactor for Co-generation of Electricity and Water. Desalination 340, 84–93.

International Atomic Energy Agency, 2007. Status of Small Reactor Designs Without On-site Refuelling, IAEA-TECDOC-1536, IAEA, Vienna, Austria.

International Atomic Energy Agency, 2008. Thermophysical Properties of Materials for Nuclear Engineering: A Tutorial and Collection of Data. IAEA Technical Report # IAEA-THPH, Vienna, Austria, http://www.pub.iaea.org/MTCD/publications/PDF/IAEA-THPH_web. pdf.

International Atomic Energy Agency, 2011. In: Workshop on SMR Technology Assessment for Near Term Deployment. IAEA Annual Report 2011, Vienna, Austria.

International Atomic Energy Agency, 2012. Status of Small Medium Sized Reactor Designs - A Supplement to the IAEA Advanced Reactors Information System (ARIS). International Atomic Energy Agency, Vienna, Austria, http://aris.iaea.org.

International Atomic Energy Agency, 2014. Status of Small Medium Sized Reactor Designs - A Supplement to the IAEA Advanced Reactors Information System (ARIS). International Atomic Energy Agency, Vienna, Austria. http://aris.iaea.org.

International Atomic Energy Agency, 2016. Advance in Small Modular Reactor Technology Developments - A Supplement to the IAEA Advanced Reactors Information System (ARIS). International Atomic Energy Agency, Vienna, Austria, http://aris.iaea.org.

International Atomic Energy Agency, 2018. Advances in Small Modular Reactor Technology Developments - A Supplement to the IAEA Advanced Reactors Information System (ARIS). International Atomic Energy Agency, Vienna, Austria. http://aris.iaea.org.

John, J., 2018. Distribute Energy Poised for Explosive Growth on the US Grid, GTM Research, 21 June, https://www.greentechmedia.com/articles/read/distributed-energy-poised-for-explosive-growth-on-the-us-grid.

Kemeny, J., 1979. Report of the President's Commission on the Accident at Three Mile Island. D.C.U.S. Government Printing Office, Washington, USA.

Klueh, R.L., Nelson, A.T., 2007. Ferritic/Martensitic Steels for Next Generation Reactors. Journal of Nuclear Materials, 371, 37-52.

Kuznetsov, V., 2008. Options for Small and Medium Sized Reactors (SMRs) to Overcome Loss of Economies of Scale and Incorporate Increased Proliferation Resistance and Energy Security. Progress in Nuclear Energy 50, 242–250.

Kyoko, I., Hisato, M., Norihiko, H., 2011. Activities for 4S USNRC Licensing. Progress in Nuclear Energy 53, 831–834.

Liu, Z., Fan, J., 2014. Technology Readness Assessment of Small Modular Reactor (SMR) Designs. Progress in Nuclear Energy 70, 20–28.

Locatelli, G, Bingham, C, Mancini, M. 2014. Small Modular Reactors: A Comprehensive Overview of their Economics and Strategic Aspects. Progress in Nuclear Energy 73, 75-83.

Lokhov, A., Sozoniuk, V., Rothwell, G., Cometto, M., Paillere, H., Crozat, M., Genoa, P., Joon Kim, T., McGough, M., Ingersoll, D., Rickman, R., Stout, D., Halnon, G., Chenais, J., Briffod, F., Perrier, S., Shahrokhi, F., Kaufer, B., Wasylyk, A., Shropshire, D., Danrong, So., Swinburn, R., 2016. Small Modular Reactors: Nuclear Energy Market Potential for Near-Term Deployment, Nuclear Energy Agency of the Organization for Economic Co-Operation and Development. Technical Report NEA-7213. Boulogne-Billancourt, France.

Lommers, L., Shahrokhi, F., Southworth, F., Mayer, J. III., 2014. AREVA Modular Steam Cycle – High Temperature Gas-Cooled Reactor Development Progress. Proceedings of the HTR-2014, Weihai, China, October 27-31, paper HTR2014-71346.

Makenas, B.J., Paxto, D.M., Vaidyanathan, S., Hoth, C.W., 1994. SP-100 Fuel Pin Performance: Results from Irradiation Testing. In: Proceedings 11th Symposium on Space Nuclear Power Systems (Editors: M.S. El-Genk, and M.D. Hoover), AIP Conference Proceedings 301, 403-412.

Maloy, S.A., Toloczko, M.B., Cole, J., and Byun, T.S., 2011. Core Materials Development for the Fuel Cycle R&D Program. Journal of Nuclear Materials 415, 302-305.

Martel, L., Minnick, L., Levey, S., 1985. Summary of Discussions with Utilities and Report to Congress: Review of Manned Aircraft Nuclear Propulsion Program. Comptroller General of the United States. 1963.

Mason, R.E., and El-Genk, M.S., 1994. Experimental Investigation of the Ruthenium-Uranium and Rhenium-Uranium Binary Systems. Journal of Nuclear Materials 217, 304-321

Matthews, R.B., Chidester, K.M., Hoth, C.W., Mason, R.E., Petty, R.L., 1988. Fabrication and Testing of Uranium Nitride Fuel for Space Reactors. Journal of Nuclear Materials 151, 345.

Menter, F.R., 1994. Two-equation Eddy-Viscosity Turbulence Modeling for Engineering Application. AIAA Journal 32, 1598-1605.

Moore., M., 2016. The Economics of Very Small Modular Reactors in the North, Proceedings 4th International Technical Meeting on Small Reactors (ITMSR-4), Ottawa, Ontario, Canada.

Mosteller, R.D., 2008. ENDF/B-VII.0, ENDF/B-VI, JEFF-3.1, and JENDL-3.3 Results for the MCNP Criticality Validation Suite and Other Criticality Benchmarks. Proceedings of International Conference on Reactor Physics, Nuclear Power, Interlaken, Switzerland.

Mosteller, R.D., Macfarlane, R.E., Little, R.C., White, M.C., 2003. Analysis of Hot and Cold Kritz Criticals with MCNP5 and Temperature-Specific Nuclear Data Libraries. Proceedings Advances in Nuclear Fuel Management III (ANFM), American Nuclear Society, USA. ID: 700296/ISBN:0-89448-670-5.

Odmaa, S., and Obara, T., 2012. Conceptual design for a small modular district heating reactor for Mongolia. Annals of Nuclear Energy 47, 210-215.

Palomino, L., El-Genk, M.S., 2016. CFD and Thermal-hydraulics Analyses of ‘‘SLIMM” Reactor Passive Decay Heat Removal by Natural Circulation of Ambient Air. Journal in Nuclear Technology 195, 1–14.

Palomino, L., El-Genk, M.S., 2016. CFD and thermal-hydraulics analyses of ‘‘SLIMM” reactor passive decay heat removal by natural circulation of ambient air. Journal in Nuclear Technology 195, 1–14.

Peakman, A., Hodgson, Z., Merk, B., 2018. Advance Micro-reactor Concepts. Progress in Nuclear Energy 107, 61-70.

Pelowitz, D.B., 2011. MCNPX, Version 2.7.0., Technical Report LA-CP-11e00438. Los Alamos National Laboratory, Los Alamos, New Mexico, USA.

Rehme, K., 1971. Laminarstromung in Stabbundeln. Chemical Engineering and Technology 43, 962–966.

Rehme, K., 1972. Pressure drop performance of rod bundles in hexagonal arrangements. International of Journal Heat and Mass Transfer 15, 2499–2517.

Rehme, K., 1973. Simple method of predicting friction factors of turbulent flow in a non-circular channel. International of Journal Heat and Mass Transfer 16, 933–950.

Roache, P.J., 1994. Perspective: A Method for Uniform Reporting of Grid Refinement Studies. Journal of Fluids Engineering 116, 405-413.

Rodriguez, S., 2017. Current Capabilities at SNL for the Integration of Small Modular Reactors Onto Smart Microgrids Using Sandia's Smart Microgrid Technology High Performance Computing and Advanced Manufacturing. Sandia National Laboratory, Technical Report SAND-2017-5537R. Albuquerque, New Mexico, USA

Rodriguez, S.B., Gauntt, R.O., Cole, R., Mcfadden, K., Gelbard, F., Drennen, T., Malczynski, L., Martin, B., Louie, D.L.Y., Archuleta, L., El-Genk, M.S., Tournier, J.-M., Espinoza, F., Vierow, K., Hagan, K., Revankar, S.T., Oh, S., 2007. Development of Design and Simulation Model and Safety Study of Large-Scale Hydrogen Production Using Nuclear Power, Technical Report SAND2007-6218, Sandia National Laboratories, Albuquerque, NM, USA.

Rodriguez, S.B., Louie, D., Gelbard, F., El-Genk, M.S., Gauntt, R.O., Tournier, J.-M., Cole, R., Gelbrad, F., McFadden, K., Revankar, S.T., Vierow, K., Drennen, T., Martin, B., Espinoza, F., Archuleta, L., 2009. Transient Analysis of Sulfur-Iodine Cycle Experiments and Very High Temperature Reactor Simulations Using MELCOR-H2. Journal of Nuclear Technology 166, 76–85.

Ross, S.B., El-Genk, M.S., 1988. Thermal Conductivity Correlation for Uranium Nitride Fuel between 10 and 1923 K. Journal of Nuclear Materials 151, 313–317.

Ross, S.B., El-Genk, M.S., 1990. Uranium Nitride Fuel Swelling Correlation. Journal of Nuclear Materials 170, 169–177.

Salemo, L.N., Berglund, R.C., Gyorey, G.L., Tipets, F.E., Tschamper, P.M., 1988. PRISM Concept, Modular LMR Reactor. Nuclear Engineering and Design 109, 79–86.

Salim, S.M., Cheah, S.C., 2009. Wall y+ Strategy for Dealing with Wall-Bounded Turbulent Flows. In: Proceedings International Multiconference of Engineers and Computer Scientists, IMECS 2009, vol. III, Hong Kong.

Schriener, T.M., and M.S. El-Genk, M.S., 2015, Convection Heat Transfer of NaK-78 Liquid Metal in a Circular Tube and a Tri-lobe Channel. International Journal of Heat and Mass Transfer, 86, 234 – 243.

Shriener, T.M. and El-Genk, M.S., 2018. Transient and Safety Analyses of "SLIMM" – a Walkaway Safe Small Modular Reactor. Journal of Nuclear Science and Power Generation 7, 442.458.

Singh, K., 2013. SMR-160: The Gravity-Driven and Gravity-Protected Small Modular Reactor, HOLETC International Presentation, http://www.platts.com/IM.Platts.Content/ProductsServices/ConferenceandEvents/2013/pc330/presentations/Kris_Singh.pdf.

Smith, C., Halsey, W., Brown, N., Sienicki, J., Moisseytsev, A., Wade, D., 2008. SSTAR: The US Lead-Cooled Fast Reactor (LFR). Journal of Nuclear Mater 376, 255-259.

Smith, M.C., Wright, R.F., 2012. Westinghouse Small Modular Reactor Passive Safety System Response to Postulated Events, Proceedings ICAPP'12, Paper 12157, American Nuclear Society.

Sterbentz, J.W., Werner, J.E., McKellar, M.G., Hummel, A.J., Kennedy, J.C., Wright, R.N., Biersdorf, J.M., 2017. Special Purpose Nuclear Reactor (5MW) for Reliable Power at Remote Sites Assessment Report – Using Phenomena Identification and Ranking Tables (PIRTs). Technical Report INL/EXT-16-40741, Idaho National Laboratory, Idaho Falls, Idaho, USA

Su, K., Freire, A.P.S., 2002. Analytical Prediction of Friction Factors and Nusselt Numbers of Turbulent Forced Convection in Rod Bundles with Smooth and Rough Surfaces. Nuclear Engineering and Design 217, 111–127.

Suid, L.H., 1990. The Army's Nuclear Power Program: the Evolution of a Support Agency. Greenwood Press.

Sun, Y., 2013. HTR Development Status in China, Presentation at IAEA YWG-GCR Meeting VIC, Vienna, Austria, https://www.iaea.org/NuclearPower/Downloadable/Meetings/2013/2013-03-05-03-07-TWG-NPTD/Day_1/3.Sun.pdf.

The U.S. Deparment of Energy's Office of Nuclear Energy, 2011, Small Modular Reactors. USA.

Thermal Fluids Central, 2016. Thermophysical properties: Sodium. Global Digital Central, Columbia, MO, USA, http://www.thermalfluidscentral.org/.

Triplett, B.S., Loewen, E.P., Dooies, B.J., 2012. PRISM: a Competitive Small Modular Sodium-Cooled Reactor. Nuclear Technology 178, 186-200.

Trupp, A.C., Azad, R.S., 1975. The Structure of Turbulent Flow in Triangular Array Rod Bundles. Nuclear Engineering Design 32, 47–84.

Ueda, N., Kinoshita, I., Minato, A., Kasai, S., Yokoyama, T., Maruyama, S., 2005. Sodium Cooled Small Fast Long-Life Reactor 4S. Progress in Nuclear. Energy 47, 222–230.

Vijayan, P.K., Pikhwal, D.S., Saha, D., Venkat R.V., 1999. Experimental Study on the Pressure Drop Across the Various Components of a PHWR Fuel Channel. Experimental Thermal Fluid Science 20, 34–44.

Vujic, J., Bergmann, R.M., Skoda, R., Miletic, M., 2012. Small Modular Reactors: Simpler, Safer, Cheaper. Energy 45, 288–295.

Wang, M., Lian, C., Li, Y., Wang, D., Jiang, J., Wu, Y., 2015. Preliminary Conceptual Design of Lead-Bismuth Cooled Small Reactor (CLEAR-SR). International Journal of Hydrogen Energy 40, 15132-15136.

Welty, J.K, Wicks, C.E., Wilson, R.E., Rorrer, G.L., 2007. Fundamentals of Momentum, Heat, and Mass Transfer, 5, 169-182, John Wiley an Sons, Inc. NJ, USA.

Westinghouse Global Technology Office, 2017. Westinghouse eVinci Micro Reactor, http://www.westinghousenuclear.com.

Westinghouse Nuclear, 2016. Small Modular Reactor by Westinghouse, http://www.westinghousenuclear.com/New-Plants/Small-Modular-Reactor.

Wilcox, D.C., 1998. Turbulence Modeling for CDF. 2nd Edition, DCW Industries, Inc.

World Nuclear Association, 2016. Small Nuclear Power Reactors, Retrieved on 2016 July 19. http://www.world-nuclear.org/information-library/nuclear-fuel-cycle/nuclearpowerreactors/small-nuclear-power-reactors.aspx.

World Nuclear Association, 2016. Small Nuclear Power Reactors, Retrieved on 2016 July 19. http://www.world-nuclear.org/information-library/nuclear-fuel-cycle/nuclearpowerreactors/small-nuclear-power-reactors.aspx.

Wright, S.A., Radel, R.F., Vermon, M.E., Rochau, G.E., Pickard, P.S., 2011. Operation and Analysis of a Supercritical CO_2 Brayton Cycle. Technical Report # SAND2010-0171, Sandia National Laboratories, Albuquerque, NM, USA.

Yu, H., Hartanto, D., Moon, J., Kim, Y., 2015. A Conceptual Study of a Supercritical CO_2-Cooled Micro Modular Reactor. Energy 8, 13938-13952.

Zhang, X., Lu, D., 2013. A Conceptual Design of a Small Modular Natural-Circulation Liquid Metal Fast Reactor with AMTEC Units. Proceedings of the 2013 21st International Conference on Nuclear Engineering, Paper 15235, American Society of Mechanical Engineers, Chengdu, China.